A Multiscale Study of Atomic Interactions in the Electrochemical Double Layer Applied to Electrocatalysis

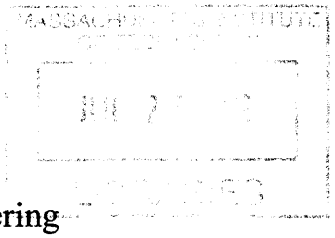

by

Nicéphore Bonnet

Diplôme de l'École Polytechnique
École Polytechnique (2005)

M.Sc., Department of Nuclear Science and Engineering
Massachusetts Institute of Technology (2007)

Submitted to the Department of Nuclear Science and Engineering
in partial fulfillment of the requirements for the degree of

DOCTOR OF PHILOSOPHY

at the

MASSACHUSETTS INSTITUTE OF TECHNOLOGY

[September 2011]

August 2011

Author .....
Department of Nuclear Science and Engineering
August 1st, 2011

Certified by .....
Nicola Marzari
Associate Professor
Thesis Supervisor

Certified by .....
Bilge Yildiz
Assistant Professor
Thesis Reader

Accepted by .....
Mujid S. Kazimi
TEPCO Professor of Nuclear Engineering
Chair, Department Committee on Graduate Students

A Multiscale Study of Atomic Interactions in the Electrochemical Double Layer Applied to Electrocatalysis

by

Nicéphore Bonnet

Submitted to the Department of Nuclear Science and Engineering
on August 1st, 2011, in partial fulfillment of the
requirements for the degree of
DOCTOR OF PHILOSOPHY

Abstract

This work is an integrated study of chemical and electrostatic interactions in the electrochemical double layer, and their significance for accurate prediction of reaction kinetics in electrocatalysis.

First, a kinetic model of the oxygen reduction reaction (ORR) on platinum, in connexion with first-principles techniques, is developed to illustrate that a self-consistent description of kinetics and reactant coverages on the surface can help to propose new mechanisms when energy prediction and experimental uncertainties still prevail. ORR kinetic limitation is often rationalized in terms of surface poisoning by parallel reactions, namely water oxidation, and/or as a result of the demanding requirements of Sabatier's principle. The sensitivity analysis presented here suggests that additional mechanisms may have to be considered, in particular self-poisoning by transient O_2 dissociation in certain regimes.

A common assumption of kinetic studies is that the only effect of electrode bias is to modify the electron chemical potential. To refine our understanding of bias effects in the double layer, a correction code applied to plane-wave DFT techniques is used to realistically simulate an electrochemical setup under potential control as an electrode with variable explicit charge screened by ions in solution.

The scheme is first used to shed light on the nature of the stretching frequency shift of CO on Pt(111) as a function of electrode potential. It is concluded that the Stark effect interpretation is correct, and more generally, that electrochemistry on metal surfaces may often be correctly described in terms of perturbation theory.

Then, hydrogen under-potential deposition on platinum is computed as a function of pH. It is shown that modification of the surface dipole by hydrogen electrosorption couples with the surface charge to make the adsorbant chemical potential pH-dependent. This observation is related to the concept of electrosorption valency. The octahedric-to-cubic nanoparticle shape transition resulting from hydrogen adsorption upon cathodic sweep is then predicted to be more pronounced in alkaline media. Inclusion of surface dipole effects is therefore relevant for surface stability and shape-dependent electroactivity.

Third, the correction scheme is applied to develop a model of water dielectric saturation in the strong fields of the double layer. The water molecule dipole is computed in real space and Monte-Carlo simulation techniques are performed for the statistics of proton arrangement.

DFT is seen to overestimate the permittivity of ice, confirming the difficulty of water simulation at the first-principles level. However, saturation effects are believed to be qualitatively captured and their influence on reaction kinetics in the double layer from the Frumkin effect is assessed. The impact is rather moderate with at most a factor of 3 in exchange current predictions.

Finally, DFT occasional errors in chemisorption energies remain an important drawback for heterogeneous catalysis studies. Here, the vdW-DF functional for inclusion of long-range, dispersion interactions is tested on the prediction of CO adsorption on transition metals. Observed improvement on binding energies and adsorption site ordering comes at the expense of the correct description of metal energetics, suggesting the need for alternative schemes in this case.

In conclusion, the purpose of this work is to help the design of electrocatalysts by providing a framework to assess chemical and electrostatic contributions to the kinetics, informed by the complexity and uncertainties attached to the surface and double layer structure.

Thesis Supervisor: Nicola Marzari
Title: Associate Professor
Thesis Supervisor

À mes parents, Anne-Marie et Manuel.

Acknowledgments

I am first extremely grateful to my advisor, Professor Nicola Marzari, thanks to whom I learned a lot, and who was very supportive of my research directions. I thank Professor Bilge Yildiz, for her help and interest in my project, as well as Professor Michael Demkowicz.

I greatly thank Professor Yang Shao-Horn for the support of my research and for exciting work and discussions in the EEL group with her and her students, in particular with Jin Suntivich.

I thank Ismaïla Dabo, with whom we had very nice work sessions on part of the project at ENPC in Paris.

I thank members of the Quasiamore group, especially Davide Ceresoli and Nicola Bonini for sharing their post-doctoral knowledge, and Nicolas Poilvert for his Python, etc., proselytism.

And to my family and friends, for all the good moments in Boston and elsewhere.

Contents

List of Figures

List of Tables

Chapter 1

Energy and Electrochemistry

1.1 Sustainability - facts and figures

1.1.1 Current situation

In 2010, the **world energy consumption** was 12 Gtoe (gigatons of oil equivalent), in which oil actually accounts for 40%[1]. The largest known resources in hydrocarbons are those of coal, estimated at 1600 Gt. Different ways to report the price of energy are here exemplified:

- Oil: 100 $/barrel
- Natural gas: 5 $/mmbtu (mmbtu $\simeq$ 0.15 barrel, energy-wise)
- Coal: became competitive when oil reached 40 $/barrel
- Electricity: 5 cents/kWh

CO_2 emissions can be roughly estimated by multiplying by 3 the mass of hydrocarbons burned. Since the beginning of industrial revolution, CO_2 concentrations in the atmosphere have risen from 280 to 400 ppm. Limiting the global temperature increase to 2°C will most likely require a 80% reduction in emissions by 2050 [2].

An average **European** consumes twice as much as the global average, with a consumption of 120 kWh/d, i.e. roughly 12 L of oil per day. This represents 50 times the human metabolism (100 W, like a light bulb):

- Heating and cooling: 40 kWh/d
- Transport: 40 kWh/d
- Electricity: 2 $\times$ 20 kWh/d (assuming 50% energy conversion efficiency)

[1]Most figures in this section are adapted from [1]. Typical numbers as of 2010 are given. The goal here is not so much accuracy as giving orders of magnitude which are easy to remember.

Table 1.1: Embedded energy and price for selected materials.

Material	Embedded energy (kWh/kg)	Price ($/t)
Cement	1.6	100
Steel	14	600
Aluminum	47	2500

Other contributions may quickly add in:

- One transatlantic round-trip flight per year $\Rightarrow$ 30 kWh/d
- Energy to produce "stuff" $\simeq$ 40 kWh/d (mostly consumed in emerging countries)

Heavy emitters related to construction or agriculture are:

- Cement and steel productions: each accounts for 5-10% of total world emissions (Table 1.1). Cement is the most produced material, 10 times more than steel. In its case, 50% of emissions are directly produced by calcination and 50% come from the energy consumed for the reaction.
- Haber-Bosch process: sometimes called the most important technological advance of the 20th century, the Haber-Bosch process now produces 100 million tons of nitrogen fertilizer per year and is responsible for sustaining 40% or earth population[2]. It consumes 1% of world's annual energy.

1.1.2 Energy solutions

Estimates for **renewable powers per surface area** are given in Table 1.2. Let us assume that a 10% efficient solar panel delivers 10 W/m^2. For an average European consuming 5000 W, 500 m^2 of solar panels are necessary[3]. For a country like France, with 60 million inhabitants, it implies 30,000 km^2 of solar panels, approximately 1/20 of the country area.

Important savings in **domestic heating** can be achieved with better insulation and more efficient heat supply. Heat pumps can have a coefficient of performance equal to 4.

[2]Haber and Bosch were awarded Nobel prizes in 1918 and 1931 respectively, for their work in overcoming the chemical and engineering problems posed by the use of large-scale, continuous-flow, high-pressure technology. During World War I, the process was used to produce explosives, particularly through the conversion of ammonia into a synthetic form of Chile saltpeter, which could then be changed into other substances for the production of gunpowder and high explosives. The Allies had access to large amounts of saltpeter from natural nitrate deposits in Chile that belonged almost totally to British industries. Therefore, Germany had to produce its own. It has been said that without this process, Germany would have had to surrender years earlier.

[3]Here, we compare oil chemical energy and electric energy, which is unfair, but it is just to get an order of magnitude. On the other hand, solar panels are only operational during daytime, and this is not accounted for either.

Table 1.2: Power per surface area for different renewable energies.

Renewable energy source	Power per surface area (W/m^2)
Wind	2 (for an average wind speed of 6 m/s)
Tidal pools	3
Tidal stream	6
PV panels	5-20
Plants	0.5
Hydroelectric facility	11
Geothermal	0.017

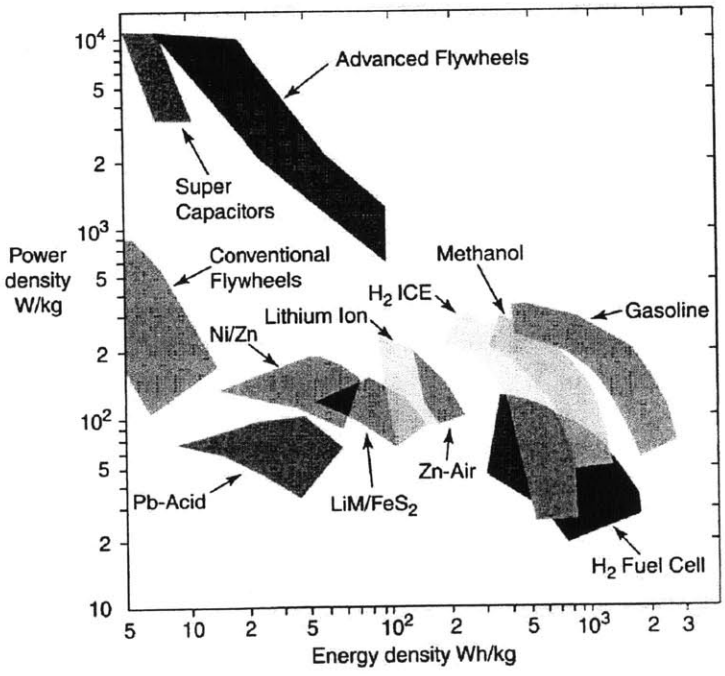

Figure 1-1: Power and energy density for different technologies.

The next field for improvement is **transportation**. An average car with a mileage of 12 km/L consumes 80 kWh per 100 km. This is comparable to air and sea transportation. By contrast, train consumes commonly 10 times less. Car performance, efficiency and environmental friendliness are improved in several ways:

- Regenerative breaking: supercapacitors and fly wheels can achieve high power densities (Fig. 1-1). For instance, a flywheel system weighing just 25 kg can store 0.1 kWh of energy, enough to accelerate an ordinary car up to 60 miles per hour, and it can accept or deliver 60 kW of power. Using regenerative breaking can save 20-30% fuel.

- Complete electrification: performance on the order of 15 kWh per 100 km has been observed on both the GWiz and the Tesla roadster. In the GWiz, the lead-acid battery stores 10 kWh and has a maximum power of 15 kW. Lead-acid technology, like compressed air, has a specific energy 5 times smaller than lithium-ion. In the Tesla roadster, the lithium-ion battery pack stores 50 kWh, has a maximum power of 200 kW, and weighs 500 kg. Its laptop battery technology costs 200 \$/kWh, 4 times cheaper than dedicated packs used in other cars. In general, comparison should be made with conventional petrol engines, which cost 30 \$/kW (note this is power instead of capacity).

Hydrogen has also been proposed as an energy vector. Production techniques include steam methane reforming, thermochemical water splitting, water electrolysis in a reverse SOFC device, possibly in connexion with high-temperature nuclear reactors ($\geq$ 800°C). Also, photoelectric water splitting can be achieved with a catalyst [3].

Electricity production is likely to rely in particular on:

- Clean coal power plants. Turbine technology solutions include the supercritical CO_2 power conversion cycle.

- PV solar energy. Capital cost has to be lowered (Table 1.3). Given high absorption coefficients in silicon ($\sim 10^3$ cm^{-1}), thin films can be used. A dramatic growth in CdTe, CdS, ZnO thin films has been observed. Organic-based solutions include the dye-sensitized and polymer solar cells. In the second case, electronic mobility is much smaller than in crystalline or amorphous semiconductors, on the order of a few cm^2s^{-1}/V vs. 1400 cm^2s^{-1}/V for silicon at room temperature. However, electrolyte is easily printed on paper, and absorption properties can be tuned chemically. Dielectric functions of polymers can be studied by ellipsometry.

Increasing the electricity production must be combined with **electric energy storage**, another prominent role for electrochemical systems. Possibilities include hydrogen production com-

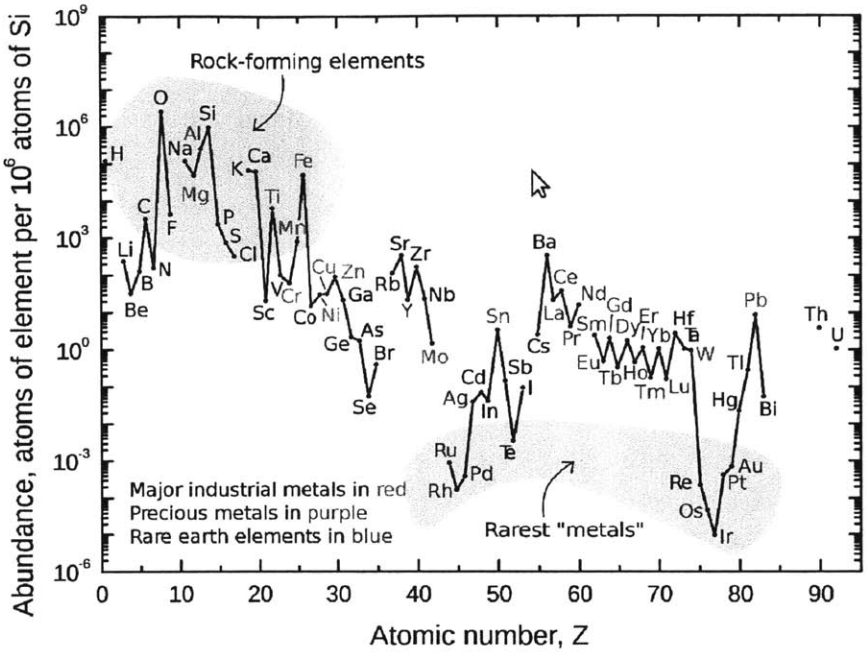

Figure 1-2: Abundance of elements.

Table 1.3: Comparison of power plant capital costs.

Technology	Capital cost ($/kW)
Advanced open cycle gas turbine	0.4
Coal-fired plant with scrubber	1.3
Advanced nuclear	2
Photovoltaic	5

bined with solid oxide fuel cells (SOFCs), Sadoway's Mg-Sb liquid metal battery [4], zinc-bromine flow battery, etc.

Resources may be a limiting factor. Natural abundance in the Earth upper crust (Fig. 1-2) and price in general (Table 1.4) must be considered.

1.2 Electrochemical systems

Luigi Galvani marked the birth of electrochemistry by observing the relation between chemical reactions and electricity in his 1791 essay "De viribus electricitatis in motu musculari com-

Table 1.4: Example of resources and price for some strategic materials.

Material	Production/Abundance	Price
Lithium	Annual production: 20,000 t. Known resources enough for 1 billion car batteries containing 3% Li.	100 $/kg
Uranium	1 million tons in Australia	100 $/kg
Silver	20,000 t/y	40 $/oz
Gold	2,000 t/y	1500 $/oz (50 $/g)
Platinum	200 t/y	50 $/g

mentarius". He believed that animal electricity was the manifestation of a specific vital force. His interpretation was rejected by Alessandro Volta, who replied that frog's legs responded to compositional differences of the metal probes. Galvani, in turn, refuted this idea by obtaining muscular activation between two electrodes of the same material. In 1800, Volta invented the **voltaic pile**, an early electric battery based on copper (or silver) and zinc (Fig. 1-3).

Work by Sir Humphry Davy in the early 1800s with electrolysis led to **isolation of sodium and potassium** from their compounds and of alkaline earth metals.

In 1832, Michael Faraday conducted experiments and stated his two laws of electrochemistry. Soon after, John **Daniell** invented a primary cell eliminating the problem of hydrogen production found in the voltaic pile (Fig. 1-4). Later, he obtained better voltage by using amalgamated zinc.

William Grove produced the first **fuel cell** in 1839.

In 1859, Gaston Planté invented the **lead-acid cell**, the first rechargeable battery. In 1899, Belgian race car driver Camille Jenatzy was the first man to break the land speed barrier of 100 km/h, at the wheel of his electric car "La jamais contente" ("Never satisfied") powered by a 50 kW_{max} lead-acid battery pack (Fig. 1-5).

In 1868, Georges Leclanché patented a new cell, a forunner of the world's first widely used battery, the **zinc-carbon cell**.

In 1886, Paul Héroult and Charles M. Hall found a method to produce aluminum by electrolysis of molten alumina.

In 1888, Walther Hermann Nernst developed the theory of the electromotive force in voltaic

Figure 1-3: Alessandro Volta (1745-1827) showing his battery to French emperor Napoléon Bonaparte.

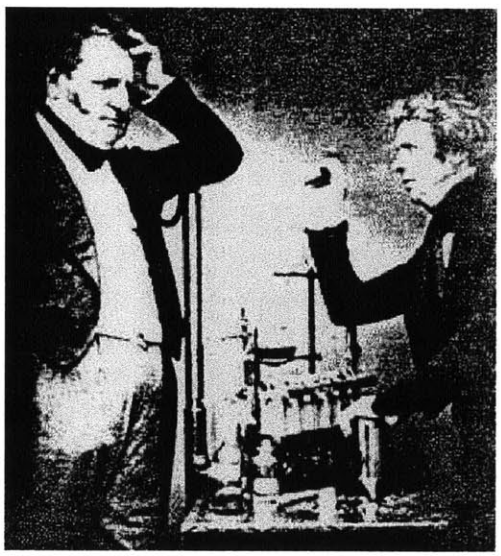

Figure 1-4: John Daniell (1790-1845) (left) and Michael Faraday (1791-1867) (right).

Figure 1-5: Camille Jenatzy (1868-1913) and his wife riding the *Jamais Contente* vehicle.

cells, and constructed **Nernst equation** to relate the cell voltage to its properties (Fig. 1-6).

In 1902, the Electrochemical Society (ECS) was founded.

The use of highly electropositive metals in batteries had been in mind since the 19th century. In "Vingt mille lieues sous les mers" ("Twenty thousand leagues under the seas") by novelist Jules Verne, Captain Nemo powers his submarine *Nautilus* with a sodium battery. The first lithium battery, proposed by M.S. Whittingham in the 1970s, used metallic lithium at the anode. In 1979, John Goodenough proposed a rechargeable cell with high cell voltage around 4 V with lithium cobalt oxide ($LiCoO_2$) as the positive electrode and lithium metal as the negative electrode. This innovation provided the positive electrode material which made the **lithium-ion battery** possible. Today's most powerful electric motorcycle in the world, the KillaCycle, is powered by a 260 kW lithium iron phosphate[4] battery pack (A123 technology), and is able to reach 60 mph within 0.97 s (Fig. 1-7).

[4] $LiFePO_4$ cathode is more stable with respect to electrolyte oxidation.

Figure 1-6: Walther Nernst (1864-1941) in the 1910s.

Figure 1-7: The KillaCycle in action.

Chapter 2

Electronic Structure Theory

2.1 The many-body problem

2.1.1 Schrödinger's equation

Physical properties of condensed matter and chemical properties in general are determined by the arrangement of nuclei and electrons, at a scale where the laws of quantum mechanics apply. In general, a system must be described by a many-body wave function, including all degrees of freedom. However, due to the large mass of the proton or neutron compared to the mass of the electron ($\frac{m_p}{m_e} \simeq 2000$), the dynamics of the latter are usually much faster, thus reaching equilibrium almost instantaneously from the nuclei perspective. This is translated into the so-called Born-Oppenheimer (BO) approximation, which is two-fold: (i) the nuclear and electronic degrees of freedom are separated, leading to factorization of the wave-function into nuclear and electronic components; (ii) for any fixed value of nuclear coordinates $\vec{R}$, the equilibrium electronic wave-function is computed. This is the assumption of adiabaticity. Repeating the calculation for many different values of $\vec{R}$ gives access to the potential energy surface (PES) of the nuclei.

Furthermore, the motion of nuclei in the PES is also often assumed to follow classical Newton mechanics. However, a quantum mechanical treatment may be required for the lightest elements such as hydrogen[1]. Likewise, the second assumption of BO approximation is not true for non-adiabatic processes, where electron dynamics can affect motion of the nuclei. Every electron has four degrees of freedom, three for its position in space and one for the spin. Let

[1] At room temperature, the wave-length of hydrogen is:

$$\lambda = \frac{h}{\sqrt{2mE}} \simeq \frac{h}{\sqrt{mkT}} \simeq 2.6 \text{ Å}$$

us denote $\mathbf{x_i} = (\mathbf{r_i}, s_i)$ the extended coordinate. For a system of N electrons, the wave-function has N^4 degrees of freedom:

$$\Psi_{\text{el}}(\mathbf{x_1}, \mathbf{x_2}, ..., \mathbf{x_N})$$

Equilibrium properties of the system are obtained by solving the non-relativistic[2] time-independent Schrödinger equation:

$$H\Psi_{\text{el}} = E\Psi_{\text{el}} \tag{2.1}$$

where the electronic Hamiltonian includes kinetic and electrostatic energies:

$$H = -\sum_{i=1}^{N} \frac{\hbar^2}{2m_e}\nabla_i^2 + v_{\text{ext}} + \sum_{i\neq j}^{N} \frac{q_e^2}{4\pi\varepsilon_0 r_{ij}} \tag{2.2}$$

v_{ext} denotes the electrostatic potential created by the nuclei or any other external source and acting on the electrons. The last term is the electron-electron interaction. Making this equation dimensionless leads to the definition of atomic units for distance and energy, namely the bohr a_0, and the Hartree energy E_a, satisfying:

$$\frac{\hbar^2}{m_e a_0^2} = \frac{e^2}{a_0} = E_a$$

Therefore, $a_0 = \frac{\hbar^2}{m_e e^2} = 0.529$ Å, and $E_a = 27.2$ eV. Incidentally, one also has $E_a = m_e c^2 \alpha^2$, with $\alpha = \frac{e^2}{\hbar c} \sim \frac{1}{137}$ (see App. A for units).

2.1.2 Electron correlation

Finding the energy of the system is equivalent to finding the two-body density matrix $\rho_2(\mathbf{r}, \mathbf{r}')$, which can be expressed in terms of the one-body charge density and the correlation function $g(\mathbf{r}, \mathbf{r}')$ [5]:

$$\rho_2(\mathbf{r}, \mathbf{r}') = \frac{1}{2}\rho(\mathbf{r})\rho(\mathbf{r}')g(\mathbf{r}, \mathbf{r}')$$

In general, electrons are correlated, and the exchange-correlation hole is defined as:

$$\rho_{XC}(\mathbf{r}, \mathbf{r}') = \rho(\mathbf{r}')\left[g(\mathbf{r}, \mathbf{r}') - 1\right]$$

[2]For heavy atoms, relativistic effects appear for core electrons. They can be included in the construction of the pseudopotential.

Assumptions on the form of the electronic wave-function translate into different statements on $g(\mathbf{r},\mathbf{r}')$:

- For independent electrons, the wave-function can be simply written as a product of individual spin orbitals $\Psi_{\text{el}} = \Psi_1(\mathbf{x_1})...\Psi_N(\mathbf{x_N})$, and $g(\mathbf{r},\mathbf{r}') = 1$.
- However, from the fact that electrons are identical fermions, Pauli exclusion principle stipulates that their collective wave-function must be anti-symmetric under electron exchange. The simplest way to satisfy this condition starting from the previous form is to anti-symmetrize the wave-function by means of a Slater determinant, $\Psi_{\text{el}} = |\Psi_1(\mathbf{x_1})...\Psi_N(\mathbf{x_N})|$. Then, $g(\mathbf{r},\mathbf{r}') \leq 1$ and tends to 1/2 when $|\mathbf{r}-\mathbf{r}'| \to 0$, expressing that electrons of the same spin do not like to be at the same place. By their very quantum mechanical nature, electrons (of the same spin) are correlated even when they do not interact. This kind of correlation is called exchange correlation.
- When the Coulomb interaction is switched on, electrons start interacting with one another, adding more correlation and reducing further the value of $g(\mathbf{r},\mathbf{r}')$. Therefore, in general, electrons are correlated as a combined effect of their quantum mechanical nature and of their interaction. The overall correlation is then rather called exchange-correlation. At this point, this has to be taken as a global expression, since the complicated form of the wave-function does not allow to define an exchange term on its own.

The electron-electron interaction energy $E_{\text{el-el}}$ can be rewritten, in dimensionless fashion:

$$E_{\text{el-el}} = \frac{1}{2}\int \frac{\rho(\mathbf{r})\rho(\mathbf{r}')}{|\mathbf{r}-\mathbf{r}'|} d\mathbf{r}d\mathbf{r}' + \frac{1}{2}\int \frac{\rho(\mathbf{r})\rho_{XC}(\mathbf{r},\mathbf{r}')}{|\mathbf{r}-\mathbf{r}'|} d\mathbf{r}d\mathbf{r}'$$

The first term is the classical expression for the charge distribution energy and is called Hartree energy. The second term is the exchange-correlation energy.

2.2 Hartree-Fock model

The Hartree-Fock theory is a hybrid approach in which the electronic wave-function is taken in the form of a single Slater determinant, while the Coulombic interaction does exist in the Hamiltonian. $E_{\text{el-el}}$ contains the classical Hartree term and an exchange term:

$$E_{\text{el-el}} = \frac{1}{2}\int \frac{\rho(\mathbf{r})\rho(\mathbf{r}')}{|\mathbf{r}-\mathbf{r}'|} d\mathbf{r}d\mathbf{r}' + \frac{1}{2}\sum_{i,j}^{N}\int \Psi_i^*(\mathbf{x})\Psi_j(\mathbf{x})\frac{1}{|\mathbf{r}-\mathbf{r}'|}\Psi_j^*(\mathbf{x}')\Psi_i(\mathbf{x}')d\mathbf{x}d\mathbf{x}'$$

Note that in the second part, terms in which $i = j$ are also included, exactly canceling self-interaction of the Hartree term. Minimization of the energy leads to a system of coupled eigenvalue equations in which each wave-function depends self-consistently on the others. This model only retains exchange-type correlation, but can be used as a starting point for further many-body (including perturbation) theories determining leading terms of the remaining correlation (e.g. MP2, CCSD, scaling in $O(N^5 - N^7)$). The main computational cost of the Hartree-Fock method is the calculation of exchange integrals, which can be expressed in terms of four-center integrals if wave-functions are projected on a basis. With no simplification, the cost is in $O(N^4)$.

2.3 Density functional theory

2.3.1 Hohenberg and Kohn theorem

The Hartree-Fock method is expensive because the primary information is stored in electron wave-functions, which in total have N^3 spatial degrees of freedom. A question to ask is whether this approach is redundant. In other words, is there a more compact way to characterize the system uniquely? The answer is yes, and is specifically the object of 1964 Hohenberg and Kohn theorem [6]:

***Theorem**: The external potential is univocally determined by the electronic density, except for a trivial additive constant.*

Since the ground-state electronic wave-function is itself a function of the external potential, an immediate corollary of that theorem is that Ψ_{el} and the total energy are functions of the density ρ:

$$E = E[\rho]$$

The primary information is now much cheaper to store, since it has only 3 degrees of freedom. The total energy is written:

$$E[\rho] = T[\Psi_{\text{el}}[\rho]] + \frac{1}{2}\int \frac{\rho(\mathbf{r})\rho(\mathbf{r}')}{|\mathbf{r}-\mathbf{r}'|} d\mathbf{r}d\mathbf{r}' + E_{\text{XC}}[\rho]$$

where T is the kinetic operator acting on the real electronic wave-function. Of course, the exact expression for $E_{\text{XC}}[\rho]$ is not known, and approximations are needed, as discussed shortly after. The kinetic energy is also, naturally, a function of the density. However, approximate

expressions of T based on the density, like in the original Thomas-Fermi model, have proven to be insufficient. One reason is that the kinetic energy should not be a smooth function of the density as orbitals are filled. This preoccupation happens to couple perfectly with a method to "code" the charge density, referred to as the Kohn-Sham approach.

2.3.2 Kohn-Sham approach

Inspired by wave-function-based methods, the idea is to consider a Slater-determinant wave-function $|\Psi_1(\mathbf{x_1})...\Psi_N(\mathbf{x_N})|$ which happens to have the same one-body density matrix as the real wave-function [7]:

$$\rho(\mathbf{r}) = \sum_{i=1}^{N} |\Psi_i(\mathbf{r})|^2$$

In other words, a "fictitious" system of non-interacting electrons is used to represent the density. That any charge density can be written this way is known as the N-representability problem, and has been proven possible. The salient feature is to use this fictitious wave-function for evaluating the kinetic energy. The kinetic energy thus obtained is of course erroneous, but the missing part can be exactly recovered by taking a certain average over a transformation in which the density is kept constant - which is always possible by tuning the external potential accordingly - and the Coulomb interaction is progressively turned on by means of a scaling parameter λ going from 0 to 1. The kinetic energy of the fictitious system is the kinetic energy of the real system - of identical density - at the beginning of the transformation, when electrons are non-interacting. The average of the correlation function in this adiabatic connexion is:

$$\tilde{g}(\mathbf{r},\mathbf{r}') = \int_0^1 g_\lambda(\mathbf{r},\mathbf{r}')d\lambda$$

and the exchange-correlation energy including correlation effects on the kinetic energy becomes:

$$\tilde{E}_{\mathrm{XC}} = \frac{1}{2}\int \frac{\rho(\mathbf{r})\rho(\mathbf{r}')}{|\mathbf{r}-\mathbf{r}'|}[\tilde{g}(\mathbf{r},\mathbf{r}')-1]d\mathbf{r}d\mathbf{r}'$$

The total energy is therefore evaluated as:

$$E = \sum_{i=1}^{N} T[\Psi_i] + \frac{1}{2}\int \frac{\rho(\mathbf{r})\rho(\mathbf{r}')}{|\mathbf{r}-\mathbf{r}'|}d\mathbf{r}d\mathbf{r}' + \tilde{E}_{\mathrm{XC}}$$

Minimization of the energy functional with respect to the charge density under constraint on the number of electrons leads to the self-consistent Kohn-Sham equations:

$$\left[-\frac{\nabla^2}{2}+v_{\text{eff}}(\mathbf{r})\right]\Psi_i=\varepsilon_i\Psi_i$$

The effective potential is given by:

$$v_{\text{eff}}(\mathbf{r})=v_{\text{ext}}(\mathbf{r})+\int\frac{\rho(\mathbf{r}')}{|\mathbf{r}-\mathbf{r}'|}d\mathbf{r}'+v_{\text{XC}}(\mathbf{r})$$

where v_{XC} is the functional derivative of the exchange-correlation energy $\delta E_{\text{XC}}[\rho]/\delta\rho$.

2.3.3 Exchange-correlation energy functionals

2.3.3.1 Local density approximation (LDA)

The system is considered homogeneous locally and a local energy density $\varepsilon_{\text{XC}}(\mathbf{r})$ is defined, equal to the corresponding energy in the homogeneous electron gas. The exchange energy density has the form adopted by Dirac:

$$\varepsilon_{\text{X}}[\rho]=-\frac{3}{4}\left(\frac{3}{\pi}\right)^{1/3}\rho^{1/3}$$

which is the exact analytical result for the homogeneous gas. In addition, exact numerical results for the correlation energy in the homogeneous gas have been obtained from Monte-Carlo simulations by Ceperley and Alder [8], and parametrized by Perdew and Zunger [9]. The exchange-correlation energy is then (now the ˜ is implicit):

$$E_{\text{XC}}^{\text{LDA}}[\rho]=\int\rho(\mathbf{r})\varepsilon_{\text{XC}}(\mathbf{r})d\mathbf{r}$$

2.3.3.2 Local spin density approximation (LSDA)

Again, from Hohenberg and Kohn theorem, it is true in general that the exchange-correlation energy is a function of the charge density. However, a simple analytical representation cannot capture possibly arising spin effects. In this case, original Kohn-Sham equations do not distinguish between spin up and spin down, leading to a set of spatial orbitals which are occupied by 2 electrons in the ground state. LSDA is a refined fit in which the exchange-correlation energy is expressed as a function of the two components, spin-up $\rho_\uparrow(\mathbf{r})$ and spin-down $\rho_\downarrow(\mathbf{r})$, of the charge density. Kohn-Sham equations remain the same, except that now there are two effec-

tive potentials $v_{\text{eff}}^{\uparrow}(\mathbf{r})$ and $v_{\text{eff}}^{\downarrow}(\mathbf{r})$ for spin-up and spin-down orbitals respectively. The LSDA functional is obtained from interpolation between the non-polarized and the totally polarized cases.

2.3.3.3 Generalized gradient approximation (GGA)

To capture the effect of inhomogeneity, the next improvement is to express the exchange-correlation energy in terms of the derivative of the charge density as well, leading to the GGA approximation, which is described as a semi-local approximation. Two commonly used functionals are the one of Perdew and Wang (PW91) [10] and the one of Perdew, Burke and Ernzerhof (PBE) [11].

2.3.3.4 Problem with analytical formulas

One consequence of analytical approaches for the electron-electron energy - similar to what was mentioned about the kinetic energy - is that $\delta E_{XC}/\delta\rho$ is a continuous function of the density, which is wrong in reality. The energy should be a series of straight lines which connect when an orbital is completely filled.

A sub-problem of the analytical treatment is the presence of self-interaction in the Hartree term (see last section).

2.4 Non-local correlation in DFT

Local and semi-local approximations often provide a good description of cohesion, bonds, structures and other properties for single molecules and dense solid-state systems. However, for sparse systems, including soft matter and biomolecules, non-local, long-ranged interactions, such as van der Waals (vdW) forces (possible interactions at distance on the order of several tens of meV), are important. The original work of Langreth and Lundqvist embarked on developing a scheme capable of marrying in a seamless fashion the DFT formalism with the description of non-local correlation effects [12]. This leads to the derivation of a so-called kernel function allowing to compute the non-local correlation energy from the sole electronic charge density:

$$E_c^{nl} = \frac{1}{2}\int \rho(\mathbf{r})\Phi(\mathbf{r},\mathbf{r}')\rho(\mathbf{r}')d\mathbf{r}d\mathbf{r}'$$

A very brief overview of physical principles behind their derivation is given here.

2.4.1 Relation between correlation and linear response

A very general result in statistical mechanics is that, for a system close to equilibrium, internal correlations (e.g. given in reciprocal space by the structure factor $S(\mathbf{q})$ for electron correlation) are related to a corresponding linear response function [13]. When an external potential v_{ext} is applied on the system, it couples linearly with the charge density in the new hamiltonian, and the charge density responds linearly through the linear response $\chi_{nn}(\mathbf{r},\mathbf{r}',t)$ (here, not the susceptibility). Specifically, the fluctuation-dissipation theorem gives:

$$\boxed{S(\mathbf{q}) \; \alpha \int_{\omega} \text{Im}\chi_{nn}(\mathbf{q},\omega)} \tag{2.3}$$

Correlations between $\mathbf{r}'$ and $\mathbf{r}$ cause a delay in the response function, corresponding to an energy transfer from the external perturbation to the system (phase shift in the complex number formalism). Interestingly, for an infinite system, such a dissipation occurs even when no coupling with an external damping system is included. Correlation ensures the transfer, and "loss", of energy into an infinite number of states in the system, which therefore is its own bath (infinite thermal capacity). For convergence considerations, the formalism often resorts to a damping parameter η appearing somewhere and then converged to 0.

2.4.2 Random phase approximation

Non-local correlations ought to be captured by a response function exhibiting long-range effects. The random-phase approximation (RPA)[3] is a mean-field approach allowing to calculate the linear response in two-steps: (i) the density response function χ° with respect to the effective potential v_{eff} acting on the electrons is determined ($v_{\text{eff}} = v_{\text{ext}} + v_{\text{int}}$, where $v_{\text{int}}[\rho]$ is the mean-field potential from electron-electron interactions, i.e. Hartree + exchange-correlation). This is possible, for example, by applying the Lehmann formula directly on the eigenstates of the self-consistent Hamiltonian. (ii) Then, to get the linear response χ with respect to the external field, one needs to know how v_{eff} changes with v_{ext} [15]:

$$\chi = \frac{\delta\rho}{\delta v_{\text{eff}}}\frac{\delta v_{\text{eff}}}{\delta v_{\text{ext}}} = \chi^{\circ}\left[1 + \frac{\delta v_{\text{int}}}{\delta\rho}\frac{\delta\rho}{\delta v_{\text{ext}}}\right] = \chi^{\circ}[1 + K\chi]$$

[3]This mean-field approach ignores dynamic effects, or assumes that those effects cancel each other. The name "random-phase approximation" comes precisely from another theory in which those effects are considered to have a random phase, which explains their cancellation.

Where the kernel K is defined:

$$\begin{aligned} K(\mathbf{r},\sigma;\mathbf{r}',\sigma') &= \frac{\delta^2 E_{Hxc}[\rho]}{\delta\rho(\mathbf{r},\sigma)\delta\rho(\mathbf{r}',\sigma')} \\ &= \frac{\delta_{\sigma,\sigma'}}{|\mathbf{r}-\mathbf{r}'|} + \frac{\delta^2 E_{xc}[\rho]}{\delta\rho(\mathbf{r},\sigma)\delta\rho(\mathbf{r}',\sigma')} \\ &= \frac{\delta_{\sigma,\sigma'}}{|\mathbf{r}-\mathbf{r}'|} + f_{xc} \end{aligned}$$

Solving for χ gives:

$$\chi = \frac{\chi^\circ}{1-\chi^\circ K}$$

The random phase approximation is to say $f_{xc} = 0$.

2.4.3 Plasmons

RPA is applied to calculate the linear response of the homogeneous electron gas. In this case, the density response function χ° is also the response of the free electron gas to an external field, and is called the Linhard function, exactly computable from free electron states. When $q = |\mathbf{q}|$ is small, χ° becomes real and is approximated by:

$$\chi^\circ(q,\omega) \simeq \frac{nq^2}{m_e\omega^2}\left[1+\frac{3}{5}\frac{q^2 v_F^2}{\omega^2}\right] + i\eta$$

where v_F is the Fermi velocity. Then, the real part of the denominator of χ goes to zero for well-chosen values of ω and q:

$$\omega_p^2(q) = \frac{4\pi n e^2}{m_e} + \frac{3}{5}q^2 v_F^2 \tag{2.4}$$

Infinite χ implies that eigenmodes of the system have been found. They are called plasmons, and are the quanta of long-ranged, collective oscillations of the electron gas (plasma). For typical electron densities n in metals, plasmons have frequencies in the THz range. The first term in Eq. (2.4) can be derived from a simple classical model. At those modes, the imaginary part of χ is a Dirac function (in reality, the response cannot diverge, energy must be dissipated). Using Eq. (2.3), the structure factor at small q is inferred:

$$S^{\mathrm{RPA}}(q) \simeq \frac{\hbar q^2}{2m_e\omega_p(q)}$$

It can be shown that $S^{\mathrm{RPA}}(q)$ exhausts a sum-rule at small q, which means that plasmons dominate excitations at long wavelengths and RPA is a good approximation in this regime.

2.4.4 vdW-DF functional

Dion et al. take the structure factor $S(q)$ from the plasmonic response that was just derived. Then, transformation into real space yields the $(\mathbf{r}, \mathbf{r}') = |\mathbf{r}' - \mathbf{r}|$ dependence of the kernel function. Dependence on the charge density results from the fact that, in Eq. (2.4), the plasmon frequency is a function of electronic density.

Romaán-Pérez and Soler developed an efficient implementation of vdW-DF [16], and implementation into the Quantum-ESPRESSO package was done by Kolb and Thonhauser [17]. A review article that shows many of the applications of vdW-DF so far can be found at [18]. Other functionals have been developed using the same physical principles (adiabatic connexion theorem, fluctuation-dissipation, RPA) [19, 20, 21].

2.5 Self-interaction

Hohenberg-Kohn theorem guarantees the existence of an exact energy functional of the charge density. However, in practice, approximate analytical expressions are used. For every electron, the Hartree term contains an energy contribution of the electron interacting with itself, a mechanism referred to as self-interaction, which is only incompletely canceled by the approximate expression of the exchange-correlation energy.

A consequence of self-interaction in DFT is a tendency to over-delocalize orbitals. This is a problem in particular for strongly correlated systems. For instance, magnetic properties in 3d metals or metal oxides are intimately related to electron localization.

Recently, Dabo et al. have developed a very promising self-interaction correction scheme in DFT, based on the idea that a self-interaction-free functional should result in orbital energies that are linear in their occupations [22].

Chapter 3

A Kinetic Model of the Oxygen Reduction Reaction (ORR) on Platinum

3.1 The development of nanocatalysts

3.1.1 Fuel cells

In the search for non-CO_2-emitting automotive technologies, proton-exchange-membrane fuel cells (PEMFCs) are considered promising because of their efficiency and power density, and their relatively low operating temperature [23]. Electricity is produced by oxidation of the hydrogen fuel:

$$H_2 + \frac{1}{2}O_2 \rightarrow H_2O \tag{3.1}$$

during which 2 electrons are exchanged through the external circuit. At the cathode of the fuel cell, oxygen is reduced:

$$\frac{1}{2}O_2 + 2H^+ + 2e^- \rightarrow H_2O \tag{3.2}$$

The development of fuel cell technology is dependent on many aspects, including the question of the hydrogen economy and hydrogen storage. Although fundamental, they are out of the scope of this study. Assuming those aspects are not the limiting factors, efforts must be invested in operating performance and economic competitiveness of the fuel cell. A continuous concern has been the highly activated nature of reaction (3.2) leading to sluggish kinetics [1]. To avoid

[1] Slow kinetics of a reaction are sometimes advantageous. In the other direction, the slow kinetics of oxygen evolution make chloride electrooxidation possible:

$$2Cl^- \rightarrow Cl_2 + 2e^-$$

losing efficiency[2] and power density by applying large overpotentials, the use of a catalyst to increase the turnover frequency of ORR is necessary.

3.1.2 Sabatier's principle and pure metal volcano plots

Conceptually, the first step in the search for a good catalyst is to span the table of pure elements, especially transition metals. In that case, catalytic activity trends can be extracted experimentally. It is found that by moving towards the right of the periodic table, a tendency to lower oxygen binding energy is accompanied by higher activity, before a maximum is reached around late transition metals and activity drops for noble metals Ag and Au. The resulting "volcano plot" is an illustration of Sabatier's principle expressing that a good catalyst should have intermediate affinity to stabilize reaction intermediates while avoiding surface saturation. The best known single metal catalyst for oxygen reduction is platinum (Fig. 3-1)[3]. Its catalytic properties for hydrogen oxidation were recognized in the early 1800s by German scientist Johann Wolfgang Döbereiner (Fig. 3-2)[4].

---

whose equilibrium potential is 1.36 V/SHE.

[2]How does one define the efficiency of a fuel cell? There is not a unique answer. If it is defined as the ratio of output electrical energy over the reaction free energy, then the maximum efficiency is in principle 1. However, this definition is not necessarily useful for the purpose of comparing fuel cell performance to other technologies. In combustion engines, the useful input energy is the fuel combustion heat given by the opposite of the enthalpy of reaction, $-\Delta H_r$. For all devices, the second principle of thermodynamics stipulates that at best (in case of reversibility) the entropy of universe remains constant. Heat flow in one direction must be counter-balanced (in a ratio given by the temperatures of exchange) by another heat flow in the other direction. In a combustion engine, where all reactant enthalpy is first transformed into heat, Carnot's law expresses the maximum efficiency in terms of the heat source combustion temperature T_{hot} and the heat sink temperature T_{cold}:

$$\eta_{\text{engine}}^{\max} = \frac{W_{\text{mech.}}}{-\Delta H_r} \leq \frac{T_{\text{hot}} - T_{\text{cold}}}{T_{\text{hot}}}$$

In the case of a fuel cell, heat flow with the exterior is likewise given by the entropic change, leading to the *thermal efficiency*:

$$\eta_{\text{fuel cell}}^{\max} = \frac{W_{\text{el.}}}{-\Delta H_r} = \frac{-\Delta H_r + T\Delta S_r}{-\Delta H_r}$$

thereby expressing that a system losing entropy ($\Delta S_r \leq 0$) releases heat which will be taken away from the output electrical work. Since the oxygen reduction reaction (3.1) produces one molecule out of two (furthermore, below 100°C, the product is in liquid state, as opposed to gaseous reactants), the reaction entropy is negative, and even more so with increasing temperatures. The thermal efficiency limit is therefore less than 1 and decreases linearly with temperature (neglecting the discontinuity introduced by the water phase transition at 100°C). Thus, at 25°C, $\eta^{\max}$ = 83% (maximum electromotive force of 1.23 V/RHE), and around 700°C, $\eta^{\max}$ = 68% ($\text{EMF}_{\max}$ = 1.01 V/RHE), a temperature at which, interestingly, the Carnot cycle starts to be more efficient (assuming a 50°C exhaust temperature).

[3]Interestingly, the best catalyst for the reverse reaction, i.e. oxygen evolution from water oxidation, is an oxide: RuO.

[4]The term catalysis was coined by Swedish chemist Jöns J. Berzelius (1779-1848), who, together with Robert Boyle (1627-1691), Antoine Lavoisier (1743-1794) and John Dalton (1766-1844), is considered a father of modern chemistry. On the physical side, Friedrich Ostwald (1853-1932) (winner of the 1909 Nobel prize in chemistry for his work on catalysis, chemical equilibria and reaction velocities), Jacobus van't Hoff (1852-1911) and Svante

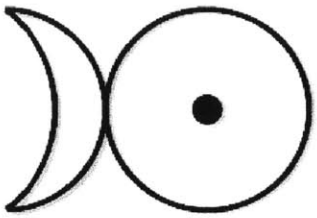

Figure 3-1: Alchemical symbol of platinum, combining those of silver and gold.

Figure 3-2: Johann Wolfgang Döbereiner (1780-1849). His work on chemical elements, leading to the discovery of patterns known as Döbereiner's triads, foreshadowed the periodic law of chemical elements. German writer Goethe was his friend, attended his lectures and used his theories of chemical affinities as a basis for his 1809 novella *Elective affinities* [25].

3.1.3 Geometric tuning

The high cost of platinum has driven the effort to maximize the mass activity of the catalyst, that is the product of its surface activity by its dispersion (surface/volume ratio). One of the first milestones in that regard was the development of carbon-supported Pt catalysts in order to get higher and more stable dispersion of the precious metal on the electronically conducting support [26]. Later came the introduction of those Pt/C catalysts in PEM fuel cell technology using recast Nafion as a proton conducting and bonding agent [27, 28], and further optimization of the catalyst layer composition and thickness was achieved for maximum catalyst utilization in operation on air and on impure hydrogen feed streams [29, 30].

In a benchmark study for Pt-based electrocatalysts, Gasteiger et al. report the typical characteristics and performance of nanoparticles in the state of the art [31]. Their size is in the 2-4 nm range[5] . At 0.8 V, 80°C, 1 atm, the measured turnover frequency (TOF) for ORR is 21 Hz (21 electrons exchanged per second per site), implying a current density of 4.83 mA/cm^2 (specific activity)[6] . Given the nanoparticle topology, a dispersion of 60 m^2/g_{Pt} is achieved, to be

Arrhenius (1859-1927) are usually credited with being the modern founders of the field of physical chemistry. Heterogeneous catalysis alone has been estimated to be a prerequisite for more than 20% of all production in the industrial world [24].

[5]There exist different methods to synthesize nanoparticles: wet chemistry (precipitation from solution followed by calcination), which generally offers less control over size distribution; nanolithography, which cannot go below 15 nm; methods involving STM, where formation is induced by the tip; evaporation and self-assembly, offering more control over size distribution (e.g. increasing heat treatment leads to larger particles); atom by atom deposition; etc.

[6]Here are some useful orders of magnitude. The **turnover frequency** is converted into surface current knowing the surface atomic density α_S. For Pt(111), $\alpha_S = 1.44 \times 10^{15}$ cm^{-2} and results in the equivalence:

$$1 \text{ Hz} \leftrightarrow 0.23 \text{ mA/cm}^2$$

A natural frequency of the transition state is $\frac{kT}{h} = 6.21 \times 10^{12}$ Hz. In this case, a turnover frequency of 1 Hz is equivalent to an energy penalty of 0.77 eV (at room temperature).

Kinetics are also affected by diffusion currents. A diffusion coefficient is essentially obtained from a relation of the type $D = \frac{kT}{h} a^2 e^{\frac{-\Delta G}{kT}}$. With a rotating disk electrode (RDE), the **mass diffusion limiting current** is related to the disk rotation speed by the Levich equation. First, a diffusion layer thickness δ can be defined, from which the current is inferred:

$$\delta = 1.61 \frac{D^{1/3} \nu^{1/6}}{\omega^{1/2}}$$

$$i_d = nF \frac{D}{\delta} C^*$$

Numerical values (for oxygen when applicable) at room temperature are:

D_O = diffusion coefficient = 1.93×10^{-5} cm^2/s
D_H = 2.13×10^{-5} cm^2/s (Grotthuss mechanism) [32]
ν = water kinematic viscosity = 10^{-2} cm^2/s
$C^*_{O_2}$ = bulk concentration = 1.26×10^{-3} mol/L

compared with a theoretical maximum of 214 m^2/g_{Pt} assuming all Pt atoms are on the surface. The resulting catalyst mass activity is then 2.90 A/mg_{Pt}. Furthermore, if Pt loading is 0.4 mg_{Pt} per square centimeter of the cathode, it yields a current at the cathode of 1.16 $A/cm^2_{cath.}$. Assuming a cathode thickness around 1 cm, the power density is 1 W/cm3, and we have 1 kW per 0.4 g_{Pt}. If the price of Pt is 50 \$/g, the catalyst part of the PEM technology cost is 20 \$/kW. This is already a substantial cost, compared to a conventional combustion engine of average total cost 30 \$/kW. Further catalyst mass reductions are therefore necessary.

However, increase of the mass activity by further reduction of the catalyst size has reached its limits for various reasons:

- **Geometric limitations** - With a dispersion already of the order of 1/3 and a catalyst utilization as high as 80%, the potential to drive more current by greater dispersion becomes fairly modest and runs into other limitations having to do with mass transport properties. Part of the challenge is relocated to the design of a sufficiently porous carbon support and an ionomer membrane recasting around it in a way that satisfies both gas and proton demands.

- **Particle size effect** - Reducing the particle size deteriorates ORR specific activity and even mass activity under a certain size. See next section for more information.

- **Chemical instability** - Finally, lower coordination of Pt atoms on the surface of small particles exacerbates the problem of chemical instability leading to Pt dissolution into the acidic electrolyte. The loss of activity with time can be attributed to nanoparticle sintering due to the dissolution/precipitation mechanism. As a variation, metal ions in solution can migrate to the ionomer and get reduced by hydrogen permeating through the proton-conducting membrane [33, 34]. To limit chemical instability, the nanoparticle original size appears to be critical. The specific surface area of a nanoparticle of original size 2.3 nm is 80 m^2/g_{Pt}, and drops to 30 m^2/g_{Pt} after 1000 cycles. The loss is reduced to 10 m^2/g_{Pt} if the particle original size is 3.7 nm. On the theoretical side, Tang et al. applied ab initio cluster expansion techniques to compute Pourbaix diagrams of Pt nanoparticles of a couple of nm diameter in acidic environment, and were able to quantify the vulnerability to dissolution as a function of geometry [35]. Generally speaking, novel solutions are then required to extend catalyst durability in acidic medium beyond

For instance, at 2500 rpm, it implies:

$$\delta_O = 1.24 \times 10^{-3} \text{ cm}$$

$$i_d = 7.56 \text{ mA/cm}^2$$

the typical 2000 hours achieved today towards the 5500 hours required for automotive applications.

3.1.4 Facet sensitivity and particle size effect

Half-way between geometric and chemical tuning, it was established that ORR activity is sensitive to facet orientation [36, 37, 38]. For instance, on platinum surfaces immersed in KOH electrolyte, where no competitive anion adsorption is occurring, the order of facet orientations for increasing ORR activity is (100) < (110) < (111).

ORR specific activity decreases as catalyst nanoparticles become smaller. Surface activity of typical, state-of-the-art Pt/C particles is 10 times smaller than for the regular Pt(111) surface. The maximum mass activity is achieved for nanoparticles in the 2-3 nm range. In line with experiments on facet sensitivity, the particle size effect has been attributed to a larger fraction of Pt atoms located in edge or corner sites in small particles. Those sites bind OH intermediates more strongly, resulting in a poisoning effect [39]. DFT studies have been supporting this interpretation. Greeley et al. have predicted decreasing ORR specific activity with decreasing particle size on Pt, but the opposite trend on Au [40]. In addition, Han et al. observed that low-coordinated site chemistry is more sensitive to particle size and surface structure than other sites [41]. Finally, corner sites may not be as suited to perform catalytic steps requiring multi-site interactions.

It is important to contrast these trends for ORR activity with other reactions. Shao-Horn et al. have shown that decreasing the particle size has a beneficial effect on methanol oxidation (MOR) and carbon monoxide oxidation (COox) reactions [42, 43]. While ORR occurs preferentially on terrace sites, CO oxidation activity is enhanced by the presence of steps which facilitate OH formation. The specific electronic structure of low-coordinated sites has been described using the Hammer-Nørskov predictor, i.e. the distance between the local d-band center and the Fermi level [44]. Interestingly, in their study on the particle size effect on ORR and COox, Mayrhofer et al. have investigated another electronic observable, namely the potential of zero total charge (pztc) [45] (see also [94]). Using the CO displacement method, they found that PZTC decreases for smaller particles, an effect which can be attributed to the electrostatics of the electron spill-over surface dipole (arguing that the surface dipole increases with surface atomic density). This is another illustration of the link between geometry and electronic structure. However, in this case, we believe that the link between PZTC shift and stronger binding energies is indirect (the effect of surface free charges on adsorption energies is typically small, see Chap. 6), as the main factor is really the adsorption site coordination.

3.1.5 Chemical tailoring

Limitations exposed in the previous section have led to search more active catalysts through chemical modification. Moving from carbon-supported Pt to carbon-supported Pt alloy catalysts, Mukerjee et al. demonstrated a 3 to 4-fold performance enhancement [46, 47]. When alloyed with Co, Ni or Cr, Pt tends to segregate towards the surface and to form a core-and-shell structure[7]. At the same time, a lowered drive of the Pt shell atoms to bond to surface oxygen atoms is observed and is understood as the result of the involvement of d-electrons of Pt atoms in bonding to Co (or Ni, or Cr) atoms in the adjacent atomic layers underneath. Therefore, continuing efforts to tailor core-and-shell alloy particles seek to further lower the mass of precious metal per unit power output and boost the catalytic activity per square centimeter of catalyst area [49].

Very representative of these prospects are the results of Stamenkovic et al. on the performance of a Pt_3Ni surface [50]. A turnover frequency around 2800 Hz is reported - again to be compared with the 250 Hz of regular Pt(111). Grown into a 30-nm-diameter octahedra, it would yield 10 times the mass activity of current Pt/C. Combining ex-situ (LEED for crystallography, LEIS for surface composition, and UPS for electronic structure) and in-situ (SXS for positions and compositions of surface and subsurface layers) spectroscopy, they showed a similar Pt segregation at the surface and a modification of the Pt surface electronic structure with a downshift of the d-band center. Cyclic voltammograms and polarization curves revealed a decrease of close to 50% of O and OH coverage and an upshift of approximately 100 mV of the onset potential for ORR. Therefore, the superior activity of the Pt_3Ni catalyst was interpreted as a consequence of reduced surface poisoning achieved through chemical tailoring of the metal affinity. Later, trends over other Pt-based alloys were exhibited, and confirmed Pt_3Co as an excellent candidate as well [51].

On the other hand, the use of electropositive alloying elements (Co, Fe, Ni) is partly challenged by requirements on operational stability because of the strong tendency of such atoms to leave the metal alloy crystal and form metal ions in solution.

3.1.6 Non-precious metal catalysts

Until recently, non-precious metal catalysts demanded overpotentials susbstantially larger than those applied with Pt/C, an additional loss on the order of 150-200 mV. However, in 2009,

[7] A general study of segregation in transition metal alloys has been completed using ab-initio methods by Nørskov et al. [48]. Concerning impurities in metals, such as C, O or S, they segregate to the surface because they have a lower surface energy.

Lefèvre et al. reported turnover frequencies around 25 Hz at 0.8 V/RHE for a novel design of nitrogen-coordinated iron on a carbon matrix, thereby equaling current Pt-based nanoparticles in performance, at a much cheaper price [52]. The next challenge for these non-precious metal catalysts is to eradicate the rapid activity loss upon utilization, as they reported a two-fold decrease in current density at constant potential over 100 hours.

3.2 ORR mechanism

The previous account reveals that much improvement in catalyst design was already achieved on geometric considerations or in light of a single-parameter version of Sabatier's principle. In that case, a catalyst surface is viewed to have a general chemical affinity for adsorbates, and the best catalyst, lying at the top of the volcano plot, is the one with the right intermediate value for this affinity. This heuristic framework is comforted by the observation that adsorption energies for different molecules are usually correlated to one another in an almost linear fashion (Brønsted-Evans-Polanyi relations), by that nourishing the idea to do optimization using a single predictor. However, those linear relationships are not perfect, and it is clear that a deviation by only a couple of tenths of eV can make a great deal of difference at the nanoscopic scale. This consideration is an encouragement for more thorough investigation into the real mechanism of oxygen reduction reaction, with the view that a more detailed knowledge of the process can help target the right limiting factors.

The difficulty comes from the fact that most of our knowledge in that regard is still relatively indirect. No experimental method allows for direct, in-situ observation of atoms as they react on the surface. The more traditional techniques consist in measuring a macroscopic response (the oxygen reduction current) as a function of an intensive parameter, thus giving only deductive insights into the nanoscopic mechanism. Most commonly they are:

i-V curves: Depending on the potential time profile, they can be polarization curves (leading to Tafel plots), cyclic voltammograms, impedance spectroscopies, etc.

Arrhenius plots: The surface current is measured as a function of temperature and an effective activation energy is inferred, $E^a = kT^2 d\ln(i_{\mathrm{ORR}})/dT$.

i-p curves: Oxygen pressure is modified in order to determine the reaction order.

More recent techniques lead to a closer description of the system at the nanoscale. They include synthesis methods to produce well defined catalyst surfaces, along with surface science techniques (most notably spectroscopic methods) to characterize their geometry and their

chemistry. On the theoretical side, development of ab-initio tools, especially based on density-functional theory, have strengthened the prospect to follow a bottom-up approach in designing improved catalysts. However, difficulties remain which, for the experimental part, come from the yet limited set of in-situ spectroscopic techniques, and for the theoretical part, have to do with the system complexity and errors inherent to ab-initio approximations. It is then important to combine insights from different perspectives to reduce as much as possible uncertainties. In the following, previous experimental and theoretical findings for the ORR mechanism on Pt surfaces are summarized.

3.2.1 Dissociative vs. associative mechanism

The formation of water at the cathode from dioxygen and protons involves essentially two types of reaction: breaking of the O-O bond and the protonation reaction. An important question is to know which one happens first.

Dissociative path - Experimentally, it is known that O_2 dissociates on Pt above 150 K (see section "O_2 dissociation?" at the end). A natural scenario would then be to postulate that O_2 first dissociates on the surface, followed by successive protonations of O, then OH, to produce water. However, DFT calculations show that the barrier for O_2 dissociation increases very rapidly with surface coverage. For a quarter monolayer, different studies find barriers between 0.5 and 0.7 eV [53, 54]. Even more restrictive, the same studies demonstrate that the energy cost for atomic oxygen protonation is on the prohibitive order of 0.9 eV, as a result of the very low diffusivity of the oxygen atom on the surface.

Associative path - Consequently, the associative path, by which protonation of the adsorbed O_2 molecule occurs before splitting of the O-O bond, appears as a reasonable alternative. Evidence for that scenario is provided by the observation of hydrogen peroxide leakage as the reaction proceeds. DFT computations (see same references), some of them including the role of surrounding water, seem to reach the same conclusion, since the maximum barrier that they predict for the associative path is around 0.4 eV. Breaking of the O-O bond in OOH is facilitated by the fact that the bond order is significantly less than 2.

3.2.2 Rate-determining step

Oxygen reduction reaction order was measured to be close to 1 [39][8], advocating for protonation of adsorbed O_2 being the rate limiting step. This conclusion is also supported by computational findings of Liang et al. [53].

3.2.3 Nanoscopic picture of Sabatier's principle

At the same time that more of the nanoscopic mechanism was understood, theoretical approaches aimed to extract guidelines for catalyst design and optimization. After important contributions by Anderson et al. who applied ab-initio techniques on model clusters [57, 58], Nørskov et al. produced impactful studies of ORR in both associative and dissociative paths on slab geometries [59]. They calculated the binding energy of successive intermediates at low coverage, and argued that the energy cost to go from one intermediate to another could be taken as a valuable estimate of the reaction barrier - without actually computing the transition state energy. They concluded that the ideal catalyst would be the one for which all those barriers are equal. They were able to show how the observed activity volcano plot across different chemistries does conform to that principle. They further pointed out the necessity of chemical stability of new alloys under potential cycling and suggested that one can attempt to overcome limitations imposed by the Brønsted-Evans-Polanyi relations by investigating other material types (oxides, complexes, etc.) [60, 61].

Apparently different in spirit, insights by Mukerjee et al. and Stamenkovic et al. put more emphasis on the role of surface coverage [62, 50]. They related the superior activity of the Pt_3Ni surface to a lowered poisoning by products of water oxidation. Wang et al. showed that it is possible to reproduce polarization curves of ORR on platinum using a simple kinetic model taking into account the effect of surface coverage on site availability and energetics [63]. Nonetheless, after some consideration, one can perceive that approaches by Nørskov et al. and Stamenkovic et al. are closely related. By computing intermediate energies at low coverage, Nørskov et al. do not so much pursue realistic description of the surface - on which equalization of chemical potentials would de facto flatten all reaction steps by adjusting species coverages, as they tend to provide a multi-parameter descriptor of species energetics. Aiming for successive steps of equal energy cost is in the end equivalent to stressing the importance of balancing coverages to limit poisoning.

[8] This value has been the object of a debate, after Neyerlin et al. did measures of the reaction order in operating PEMFCs, providing apparent support for an ORR reaction order of 0.5 [55]. Debates also appeared on values of the Tafel slope. In the latter case, Makharia et al. contributed elegantly by means of impedance spectroscopy, finding an intrinsic Tafel slope close to 120 mV/dec. [56].

However simple and appealing those rationales, it should be kept in mind that they pertain to a wider picture in which self-consistently determined coverages and activation energies do a priori affect the kinetics. In fact, it may be along those lines that limitations imposed by Brønsted-Evans-Polanyi relationships will be overcome. In addition, simplified approaches may have to be considered with caution in their relation to macroscopic observables. When estimating reaction rates from adsorbate energies, Nørskov et al. naturally find a Tafel slope of 60 mV/dec for ORR on platinum [59], close to the experimental value, but a more complete treatment reveals the combination of two different effects: the Butler-Volmer relation at the transition state with a symmetry factor of 0.5 yields an "intrinsic" Tafel slope equal to 120 mV/dec, while simultaneously the applied overpotential tends to clear the surface from oxygenated species, thus bringing the effective Tafel slope back to a value close to 60 mV/dec [39]. This counter-effect disappears at lower potentials where an increase of the Tafel slope is observed.

3.3 Our ORR kinetic model

In line with considerations of the previous paragraph, our purpose here is to develop a kinetic model for ORR which encompasses surface coverage effects as well as activated processes. The way reactions are inter-connected is simplified based on previous findings about dominant mechanisms, but the spirit of a fully self-consistent system is maintained.

3.3.1 Set of reactions

The assumptions used to draw the reaction mechanism showed in Fig. 3-3 have been partially explained earlier in the text. They are summarized here:

- Before interacting with the surface, O_2 is dissolved in the electrolyte and is in equilibrium with the gas phase.
- Only the associative path is considered.
- The first reaction on the surface is O_2 protonation to form OOH. This is also the rate-determining step. The single electron transfer is supported by an intrinsic Tafel slope of 120 mV/dec.
- Before reacting, O_2 is assumed to have adsorbed on the surface (Langmuir-Hinshelwood condition). This is to capture the chemical specifity of the metal. In addition, the presence of O_2 adsorbed on the surface is supported by spectroscopic studies by Adzic et al. [64].

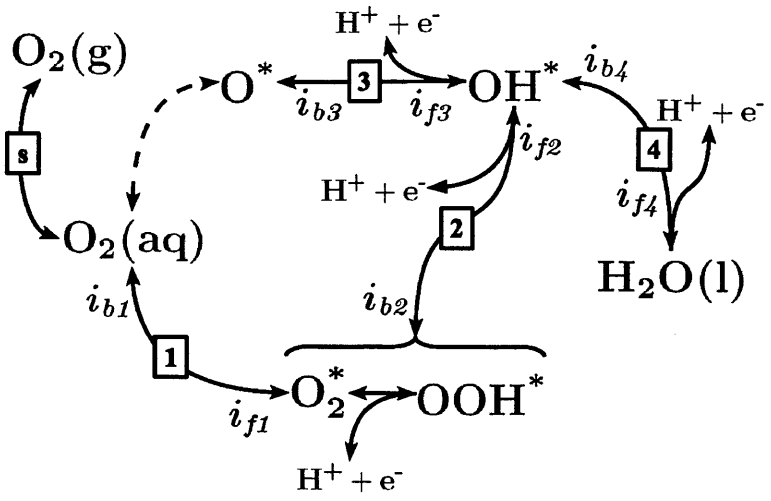

Figure 3-3: Schematic showing reactions considered in our ORR model.

- In turn, OOH is protonated and dissociates into 2OH. This route is proposed based on findings by Jacob et al. that H_2O_2 is rather unstable on the surface and prefers to dissociate immediately. We also assume that OOH does not split before being protonated as it would lead to formation of atomic oxygen, which has been seen to be very costly to protonate.
- Nonetheless, atomic oxygen does exist on the surface owing to water oxidation.
- Protons involved in protonation reactions are assumed to be in solution (as opposed to adsorbed on the surface). This is justified by the observation that under-potential hydrogen deposition on platinum occurs around 0.3 V/RHE. At potentials relevant for oxygen reduction, hydrogen surface coverage should then be very low[9].

3.3.2 Transition state theory

The rate at which each of the above reaction proceeds is quantified by the traditional transition state theory[10]. For any of the possible paths open to the reaction in the energy landscape, the point of highest free energy determines the probability that this path will be effectively selected. In practice then, only the paths with lowest energy for this intermediate state are considered to contribute to the kinetics. Usually, one such path is identified, and its highest point, lying

[9]Arguably, that could be viewed as part of the reaction barrier. Arguments based on the Tafel slope could then be also invoked.

[10]The main reference for this part is [65].

at a col of the energy landscape, is called the *transition state* (TST)[11]. Provided a free site is available, any molecule reaching the transition state is expected to fall over the other side of the ridge and relax into the reaction product, at a rate given by the vibration frequency of the TST bond that is being formed or broken during the reaction[12]. Thus, in a reaction where a reactant R is transformed into a product P, the production rate is given by:

$$r = \frac{dN_P}{dt} = \nu N^* \Pi_{\text{free}} \tag{3.3}$$

where ν is the vibration frequency driving the reaction (TS bond), N^* is the number of molecules in the transition state, and Π_{free} is the probability to find a free site. Evaluation of N^* is most easily achieved by different methods depending on the type of reaction.

3.3.2.1 Molecular and atomic adsorption

In the gas phase, molecules are far from each other, and on the surface, the number of molecules in the transition state is small. The corresponding partition functions Q_g and Q^* can therefore be approximated by the expressions:

$$Q_g = \frac{q_g'^{N_g}}{N_g!}$$

$$Q^* = \frac{q'^{*N^*}}{N^*!}$$

where q_g' and q'^* are the partition functions for an individual molecule and N_g and N^* are their respective numbers in each phase (for partition functions in the gas phase, see Table 3.1). Since the two phases are in equilibrium, their chemical potentials, $\mu = -kT\frac{\partial \ln Q}{\partial N}$, are equal, which implies:

$$\frac{N^*}{N_g} = \frac{q'^*}{q_g'} \tag{3.4}$$

The partition function of a vibrational mode of frequency $\tilde{\nu}$ is:

$$q_{\tilde{\nu}} = \frac{e^{-\frac{h\tilde{\nu}}{2kT}}}{1 - e^{-\frac{h\tilde{\nu}}{kT}}}$$

[11] "Early transition state" and "late transition state" are expressions used to describe a TST that resembles more the reactant or the product state, respectively.

[12] Nuclear tunneling effects are in addition included in the quantum TS theory also known as Kramers theory.

Table 3.1: Partition functions for a molecule in the gas phase.

	q	⟨Energy⟩	Entropy
Translational[1]	$\frac{\Omega}{\lambda_T^3}$	$\frac{3}{2}kT$	$k\ln\frac{\Omega}{\lambda_T^3}+\frac{5}{2}k$
Rotational[2]	$\frac{kT}{2\varepsilon_{rot}}$	kT	$k+k\ln\frac{kT}{2\varepsilon_{rot}}$
Vibrational[3]	$\frac{e^{-\beta h\nu/2}}{1-e^{-\beta h\nu}}$	ZPE[4]	$\frac{h\nu/T}{e^{\beta h\nu}-1}-k\ln\left(1-e^{-\beta h\nu}\right)$
Electronic	–	E_{el}	–

[1] Including all 3 degrees of freedom. $\lambda_T=\frac{h}{\sqrt{2\pi mkT}}$.

[2] Including all corresponding degrees of freedom of diatomic molecule. The factor 2 in denominator is for homodiatomic molecules because of indistinguishability of the atoms, and is therefore applicable for O_2. For O_2, $\varepsilon_{rot}=0.179$ meV.

[3] Including the zero-point energy, and only for one vibration mode.

[4] If $h\nu \gg kT$.

If the bond is weak, i.e. $kT \gg h\tilde{\nu}$, $q_{\tilde{\nu}}$ simplifies into $\frac{kT}{h\tilde{\nu}}$, whereas if the bond is strong, it simplifies into $e^{-\frac{h\tilde{\nu}}{2kT}}$ (whereby the entropy is reduced to zero). Therefore, taking electronic and vibrational contributions out of the partition functions gives:

$$\frac{q'^*}{q'_g}=\frac{kT}{h\nu}\frac{q^*}{q_g}e^{-\frac{\Delta E}{kT}} \tag{3.5}$$

where q_g and q^* are the partition functions including only translational and rotational degrees of freedom, and ΔE is the change in electronic and zero-point energy from non-TS bonds at the transition state. If the molecule does not dissociate upon adsorption, the probability to find a free site for the product on the surface is simply $1-\theta$, where θ is the total surface coverage. By combining with Eqs. (3.3), (3.4) and (3.5), it follows:

$$r=\frac{kT}{h}N_g\frac{q^*}{q_g}e^{-\frac{\Delta E}{kT}}(1-\theta) \tag{3.6}$$

The expression for q^* is different depending on the assumption of *indirect* or *direct* adsorption.

Indirect adsorption - The molecule in the transition state is free to move along the surface. Using analytical expressions for translational partition functions in 2D and 3D, neglecting the rotational contribution, and assuming the gas to be perfect, the production per surface site becomes:

$$\frac{d\theta_P}{dt}=\frac{r}{M}=\frac{kT}{Mh}\frac{pV}{kT}\frac{A(2\pi mkT)/h^2}{V(2\pi mkT)^{\frac{3}{2}}/h^3}(1-\theta)$$

where M is the number of sites on the surface of area A, and V is the volume of the gas phase. Introducing the surface atomic density N_0, it simplifies into:

$$\frac{d\theta_P}{dt} = \frac{p}{N_0\sqrt{2\pi mkT}}(1-\theta)$$

Direct adsorption - The bond of the transition state to the surface is already strong enough to prevent free motion along the surface. The transition state is attached to a site, but can vibrate in all directions. The configurational entropy of the transition state per surface site is:

$$s_{\text{conf}} = \frac{k\ln Q^*}{M} = -k(\theta^*\ln\theta^* + (1-\theta^*)\ln(1-\theta^*)) \tag{3.7}$$

In the limit where only one molecule is present on the surface, $\theta^* = \frac{1}{M} \ll 1$, implying:

$$\frac{k\ln Q^*}{M} = \frac{k\ln q^*}{M} = -k\theta^*\ln\theta^*\left(1 - \frac{1}{\ln\theta^*}\right) \simeq -k\theta^*\ln\theta^* \simeq -k\frac{\ln\frac{1}{M}}{M}$$

from which it follows[13] that $q^* \simeq M$. Substituting this result and the expressions for the 3D translational partition function in Eq. (3.6) gives:

$$\begin{aligned}
\frac{d\theta_P}{dt} &= \frac{kT}{Mh}\frac{N_g M}{q_g^{\text{trans}} q_g^{\text{rot}}} e^{-\frac{\Delta E}{kT}}(1-\theta) \\
&= \frac{kT}{h}\frac{pV}{kT}\frac{1}{q_g^{\text{rot}}}\frac{h^3}{V(2\pi mkT)^{\frac{3}{2}}} e^{-\frac{\Delta E}{kT}}(1-\theta) \\
&= \frac{p}{N_0\sqrt{2\pi mkT}} S_0(T)(1-\theta)
\end{aligned} \tag{3.8}$$

with $S_0(T) = \frac{N_0 h^2}{2\pi mkT} e^{-\frac{\Delta E}{kT}}$. If vibrations of the TST in planar directions are of intermediate strength, an intermediate simplification of the vibrational partition function must be used. One then rather has:

$$S_0(T) = \frac{q'^*_{\text{2D,direct}}}{q'^*_{\text{2D,indirect}}} = \frac{\left(\frac{kT}{h\nu_{\text{2D}}}\right)^2 h^2}{a^2(2\pi mkT)} e^{-\frac{\Delta E_{\text{el}} + h\nu_{\text{2D}}}{kT}}$$

[13] It is an obvious result if one goes back to the definition of Q^* as a binomial coefficient; for one molecule, it is equal to $\binom{M}{1}$, which is indeed equal to M. However, the general formula in terms of θ^* was first derived because it will be useful further in this dissertation.

where a is the lattice parameter (of a square lattice for simplification). Taking some typical numbers, $a = 2.5$ Å, T = 300 K, $m = m_{Ar} = 40$ amu, $\Delta E_{el} = 0$ eV, $\nu_{2D} = 40$ cm^{-1}, we obtain:

$$S_0(T) = \left(\frac{kT}{h\nu_{2D}}\right)^2 e^{-\frac{h\nu_{2D}}{kT}} \times 4.0 \times 10^{-3} = 0.09$$

3.3.2.2 Link to collision theory

Based only on the Boltzmann distribution of velocities, collision theory finds that the rate of collision per surface site is:

$$\frac{d\theta_P}{dt} = \frac{p}{N_0\sqrt{2\pi mkT}}$$

Then, to get the effective rate of adsorption, an efficiency coefficient is introduced, called the sticking coefficient. If the process is activated, the sticking coefficient includes the exponential factor associated with that.

3.3.2.3 Simplified approach in the case of direct adsorption

In the case of direct adsorption, N^* can be directly obtained from equality of the chemical potentials. Differentiation of Eq. (3.7) with respect to θ^* gives:

$$-\frac{ds_{conf}}{d\theta^*} = -\frac{dS_{conf}}{dN^*} = k\ln\frac{\theta^*}{1-\theta^*}$$

Considering that all entropic free energy $-Ts_g$ from translational and rotational motions is lost upon adsorption at the transition state, and neglecting translational and rotational enthalpies, the free energy change for one molecule reaching the transition state, *factoring out the contribution from the TS bond*, is:

$$\delta G = Ts_g + kT\ln\frac{\theta^*}{1-\theta^*} + \Delta E$$

when equilibrium is established ($\delta G = 0$) and assuming $\theta^* \ll 1$:

$$\theta^* = e^{-\frac{s_g}{k}} e^{-\frac{\Delta E}{kT}}$$

Now, refactoring in the contribution of the loose TS bond to the partition function, we obtain:

$$\frac{d\theta_P}{dt} = \frac{kT}{h}\theta^*(1-\theta) = \frac{kT}{h} e^{-\frac{s_g}{k}} e^{-\frac{\Delta E}{kT}}(1-\theta) \tag{3.9}$$

To check that this equation is similar to the first line of Eq. (3.8), we can reexpress the chemical potential using the partition function:

$$\mu_{\text{trans}} + \mu_{\text{rot}} = -kT\frac{\partial \ln Q}{\partial N_g} = -kT\ln\frac{q_g}{N_g}$$

and assuming that for those degrees of freedom, the term Ts dominates the enthalpy:

$$e^{-\frac{s_g}{k}} \simeq e^{\frac{\mu_{\text{trans}}+\mu_{\text{rot}}}{kT}} = \frac{N_g}{q_g}$$

Moreover, if there is no dissociation, the molecule adsorption should be non-activated ($\Delta E = 0$), simplifying Eq. (3.9) into:

$$\boxed{\frac{d\theta_P}{dt} = \frac{kT}{h}e^{-\frac{s_g}{k}}(1-\theta)} \tag{3.10}$$

To give a sense of s_g, for O_2 in standard conditions, $Ts_g = 0.6$ eV, in which 0.5 eV are translational and 0.1 eV are rotational.

3.3.2.4 Molecules on the surface

The number of molecules in the transition state is proportional to the number of reactant molecules and to the probability to reach the transition state. The reaction rate per surface site is then directly:

$$\boxed{\frac{d\theta_P}{dt} = \theta_R\frac{kT}{h}e^{\frac{\Delta S^*}{k}}e^{-\frac{\Delta E}{kT}}(1-\theta)} \tag{3.11}$$

In the special case of a desorption reaction, there is no significant entropic change from the adsorbate to the transition state, while the enthalpic difference should be close to the desorption energy. Therefore:

$$\boxed{\frac{d\theta}{dt} = -\theta\frac{kT}{h}e^{-\frac{\Delta E_{\text{des}}}{kT}}} \tag{3.12}$$

3.3.3 Reaction barriers

Here, we define the enthalpic and entropic barriers ΔS^* and $-\Delta E^*$ of Eq. (3.11) for the specific reactions of our kinetic model.

Table 3.2: Thermodynamic data for a selected set of molecules [66].

	ΔH_f° (kJ mol^{-1})	ΔG_f° (kJ mol^{-1})	S° (J mol^{-1}K^{-1})	Ts (eV)[1]
H_2O(g)	-241.8	-228.6	188.8	0.58
H_2O(l)	-285.8	-237.1	70.0	0.22
HO_2(g)	10.5	22.6	229.0	0.71
H_2(g)	0	0	130.7	0.40
O_2(g)	0	0	205.2	0.63
O(g)	249.2	231.7	161.1	0.50
OH(g)	39.0	34.22	183.7	0.57

[1] At room temperature (T = 298 K).

Table 3.3: Reaction enthalpies.

$\Delta H[2OH(g) \rightarrow O_2(g) + H_2(g)] = -0.81$ eV
$\Delta H[OH(g) \rightarrow O(g) + \frac{1}{2}H_2(g)] = 2.18$ eV
$\Delta H[H_2O(l) \rightarrow OH(g) + \frac{1}{2}H_2(g)] = 3.37$ eV

Table 3.4: Electronic energies of selected molecules computed by GGA-DFT (with RRKJUS pseudopotentials of Quantum-ESPRESSO distribution) and corrected using reaction enthalpy $\Delta H[H_2O(l) \rightarrow \frac{1}{2}O_2(g) + H_2(g)] = 2.96$ eV. See also Table 3.9.

	RRKJUS	Corrected
H_2O	-466.047	-466.047
H_2	-31.6947	-31.6947
OH	-447.193	-447.144
O_2	-863.718	-863.212
HO_2	–	-879.086
O	–	-428.973

3.3.3.1 Electron transfer

Most reactions considered here involve an electron transfer. In addition to chemical changes, this implies a response from the solvent polarizability, described in Marcus theory [67]. Description of inner-shell electron transfer at the metal surface, possibly coupled with proton exchange, remains complex and has been the topic of several studies [68, 69, 70, 71, 72] (see also book chapter [73]). In particular, one may have to assess a desolvation cost rather than the cost of solvent reorganization. Here, we do not try to explicitly treat solvent effects in electron transfer reactions. They are implicitly included in the reaction barriers that we introduce.

3.3.3.2 Enthalpic barriers

Three enthalpic barriers at the transition state, E^*_{f2}, E^*_{f3} and E^*_{f4}, for reactions 2, 3 and 4 in the forward direction, are introduced. In practice, the fact that reaction 2 is the rate-determining step must impose that E^*_{f2} is the largest[14]. For the definition of these barriers, low coverage on the surface, and an electrode potential of 1.23 V/RHE are assumed. When a non-zero overpotential is applied to the electrode, $U = 1.23 - \eta$ (here, η is counted positive if the reaction is forced towards reduction), the barrier of each of those reactions, that involve an electron in their reactants, is modified as described by the Butler-Volmer relation:

$$E^*_f(\eta, 0) = E^*_f(0,0) - \alpha e \eta$$

where α is a symmetry factor. This implies an intrinsic Tafel slope $\frac{kT\ln 10}{e\alpha}$. When coverage on the surface is non-zero, reaction barriers are related to the change in adsorption energy of reactants and products, in the spirit of Brønsted-Evans-Polanyi relations:

$$E^*_{f2}(\eta, \theta_s) = E_{f2}(\eta, 0) + p_2 \left[2\delta E_{\text{ads}}(\text{OH}) - \delta E_{\text{ads}}(\text{O}_2)\right]$$

$$E^*_{f3}(\eta, \theta_s) = E_{f3}(\eta, 0) + p_3 \left[\delta E_{\text{ads}}(\text{OH}) - \delta E_{\text{ads}}(\text{O})\right]$$

$$E^*_{f4}(\eta, \theta_s) = E_{f4}(\eta, 0) - p_4 \delta E_{\text{ads}}(\text{OH})$$

where δE_{ads} is the change in adsorption energy compared to the low coverage surface.

[14]This statement is not completely rigorous. In general, one should rather speak of the rate-determining transition state. It is the transition state whose coverage on the surface is the lowest, thus imposing its turnover frequency to the whole multi-step reaction. This transition state does not necessarily belong to the most activated step, as it can as well come after a reaction whose product has a very small coverage itself.

Barriers for backward reactions are obtained from a consistency condition on reactant and product energies (Tables 3.2 and 3.3). Thus[15], in eV:

$$\begin{aligned} E^*_{b2}(\eta,\theta_s) &= E^*_{f2}(\eta,\theta_s) + \Delta H[2OH(g) \rightarrow O_2(g) + H_2(g)] - eU - 2E_{ads}(OH) + E_{ads}(O_2) \\ &= E^*_{f2}(\eta,\theta_s) - 0.81 - 1.23 + \eta - 2E_{ads}(OH) + E_{ads}(O_2) \\ &= E^*_{f2}(\eta,\theta_s) + \eta - 2.04 - 2E_{ads}(OH) + E_{ads}(O_2) \end{aligned}$$

$$\begin{aligned} E^*_{b3}(\eta,\theta_s) &= E^*_{f3}(\eta,\theta_s) + \Delta H[OH(g) \rightarrow O(g) + \frac{1}{2}H_2(g)] - eU - E_{ads}(OH) + E_{ads}(O) \\ &= E^*_{f3}(\eta,\theta_s) + 2.18 - 1.23 + \eta - E_{ads}(OH) + E_{ads}(O) \\ &= E^*_{f3}(\eta,\theta_s) + \eta + 0.95 - E_{ads}(OH) + E_{ads}(O) \end{aligned}$$

$$\begin{aligned} E^*_{b4}(\eta,\theta_s) &= E^*_{f4}(\eta,\theta_s) + \Delta H[H_2O(l) \rightarrow OH(g) + \frac{1}{2}H_2(g)] - eU + E_{ads}(OH) \\ &= E^*_{f4}(\eta,\theta_s) + 3.37 - 1.23 + \eta + E_{ads}(OH) \\ &= E^*_{f4}(\eta,\theta_s) + \eta + 2.14 + E_{ads}(OH) \end{aligned}$$

From that, one can see that the dependence on the electrode overpotential is:

$$E^*_b(\eta,\theta_s) = E^*_b(0,\theta_s) + (1-\alpha)e\eta$$

3.3.3.3 Protonation entropic barrier

The same reactions also involve a protonation. In the forward or backward direction, the proton transfer requires reorganization of the solvent with an entropic cost. This cost S^* is here introduced as a variable and enters an additional barrier of entropic nature $e^{-\frac{S^*}{k}}$.

3.3.3.4 Adsorption - desorption

In Eqs. (3.10) and (3.12) for adsorption and desorption, the kinetic barriers are directly given by the entropy of the reactant and the desorption energy.

[15]In deriving these relations, the definition of the reversible hydrogen electrode potential (RHE) was used. By convention, at this potential, the reaction $H^+ + e^- \leftrightarrow \frac{1}{2}H_2$ is at equilibrium, implying equality of chemical potentials on the two sides. To simplify the treatment, we also assume that the entropy of the proton in acidic medium is comparable to the entropy of $\frac{1}{2}H_2$ at atmospheric pressure, which leads to say that the enthalpy of $H^+ + e^-$ at 0 V/RHE and low pH is equal to the one of $\frac{1}{2}H_2$. At 1.23 V/RHE, we need to subtract 1.23 eV. In the case of backward reaction 2, we only count one electron in the calculation of the barrier, because reaction 2 is in fact not an elementary step.

Table 3.5: Vibrational frequencies (cm^{-1}) and corresponding zero-point energies. DFT values are shown when they have been calculated. Experimental values in the gas phase are from [66]. Total ZPE is derived from experimental vibrational frequency when available, from DFT otherwise.

	DFT	Exp.	ZPE (eV)
$H_2O(g)$[1]	-	3657	0.56
	-	1595	
	-	3756	
$HO_2(g)$[2]	-	3436	0.37
	-	1392	
	-	1098	
$H_2(g)$	4280	4401	0.27
$O_2(g)$	-	1580	0.10
OH(g)	-	3738	0.23
H/Pt(111)	1070	900[3]	0.06
H/Pt(100)	1469	-	0.09
O/Pt(111)	496	490[4]	0.03
OH/Pt(111)[5]	-	3476[6]	0.24
	602	435[6]	

[1] Symmetric stretch, bend, antisymmetric stretch, respectively.
[2] H-O stretch, bend, O-O stretch, respectively.
[3] Ref. [74].
[4] Ref. [75].
[5] Intramolecular, adsorbate-surface, respectively.
[6] Ref. [76].

Table 3.6: Preferential adsorption sites for OH and O on Pt.

	(111)	(100)	(110)
OH	atop[1,6] 	bridge[1,6] 	atop[1,6] 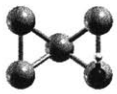
O	fcc[1,3,4,6] 	bridge[1,2] 	short bridge[1,5] 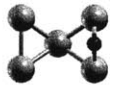

[1] This work
[2] [77]
[3] [78]
[4] [79]
[5] [80]
[6] [81]

3.3.4 Adsorption energies

As shown in the previous section, determination of the kinetic barriers requires knowledge of adsorption energies. Binding energies of atomic and molecular oxygen at specific coverages on Pt facets have been computed in several DFT studies [77, 78, 79, 80, 81] (also see [82] for a more general review). Our own calculations predict preferential adsorption sites in agreement with previous findings (Table 3.6). In general, the adsorption energy is affected by the presence of other molecules on the surface through lateral interactions. A general way to capture such a dependence is the cluster expansion, which allows systematic determination of two-body, three body, etc., interactions with first-nearest neighbors, second-nearest neighbors, etc. Here, a slightly simplified approach is suggested where the total energy on the surface is written as a polynomial of the different species coverages. Considering only species O, OH and O_2 as contributing significantly to the total coverage and numbering them 1, 2, 3 respectively, we write the energy per surface site (electronic energy plus ZPE):

$$E_{\text{surf}} = a_0 + a_1\theta_1 + \frac{a_{11}}{2}\theta_1^2 + a_2\theta_2 + \frac{a_{22}}{2}\theta_2^2 + a_3\theta_3 + \frac{a_{33}}{2}\theta_3^2 + a_{12}\theta_1\theta_2 + a_{23}\theta_2\theta_3 + a_{31}\theta_3\theta_1$$

The differential adsorption energy of each molecule, as required in the kinetic equations, is obtained by differentiating the energy and subtracting the energy in the gas phase:

$$E_{\text{ads}}(\text{O}) = a_1 + a_{11}\theta_1 + a_{12}\theta_2 + a_{31}\theta_3 - E(\text{O(g)})$$

$$E_{\text{ads}}(\text{OH}) = a_2 + a_{22}\theta_2 + a_{12}\theta_1 + a_{23}\theta_3 - E(\text{OH(g)})$$

$$E_{\text{ads}}(\text{O}_2) = a_3 + a_{33}\theta_3 + a_{23}\theta_2 + a_{31}\theta_1 - E(\text{O}_2\text{(g)})$$

3.3.4.1 Determination of a_1, a_2, a_{12}

Computation of coefficients for O and OH is delicate owing to the sensitivity of OH binding energy to surrounding water. Experimentally also, the nature of oxygenated species (O vs. OH) adsorbed upon raising potential has long been regarded as rather elusive. The question dates back to the work of Conway et al. in the 70s who made extensive studies of oxygen and oxide formation on platinum [83]. Later, the same questions were tackled with the advantage that well-defined single-crystal surfaces were available. Existence of a coadsorbed OH+H_2O overlayer as an intermediate in the formation of water has been evidenced experimentally and computationally [84, 85, 86]. Nonetheless, in voltammetry experiments, determination of the chemical nature of adsorbates may be delicate. Significant work by Jerkiewicz et al., studying surface-oxide growth at platinum electrodes in aqueous H_2SO_4 with a combination of cyclic voltammetry, in-situ electrochemical quartz-crystal nanobalance and ex-situ Auger electron spectroscopy, concluded that direct formation of atomic oxygen occurred, with no intermediate OH [87]. However, sulfate ions are strong adsorbants and competitors on the surface, implying that different oxygen patterns can be observed in other electrolytes. Investigating oxygen formation on Pt(111) and polycrystalline Pt in fluoric acid using X-ray photoelectron spectroscopy, Watanabe et al. found coformation of O and OH on the surface at oxidative potentials [88][16]. Later, ab-initio cluster-expansion computations by Viswanathan et al. including the effect of coadsorbed water molecules established the Pourbaix diagram of Pt(111), with results very close to those of Watanabe et al. and consistent with voltammetric currents [89][17]. Therefore, we here propose to build on those studies by adjusting the values of a_1, a_2 and a_{12} so that the subsequent O and OH coverages fit Watanabe's results. We find, in eV, $a_1 = -4.04$, $a_{11} = 1.60$, $a_2 = -2.75$, $a_{22} = 0.50$, $a_{12} = 1.00$ (Fig. 3-4).

3.3.4.2 Determination of a_3, a_{33}, a_{23}, a_{31}

GGA-DFT calculations have been performed to determine O_2 adsorption energy as a function of coverage and with coadsorption of OH and O (Figs. 3-5 and 3-6). Interestingly, O_2 is extremely sensitive to atomic oxygen, but not to OH.

[16]For the spectroscopic measurement, the electrode is transfered to UHV. Evaporation of a droplet remaining on the surface cools the system below 220 K.

[17]Generally speaking, water Pourbaix diagrams on a variety of transition metals have been extensively studied by Nørskov et al. [90, 91].

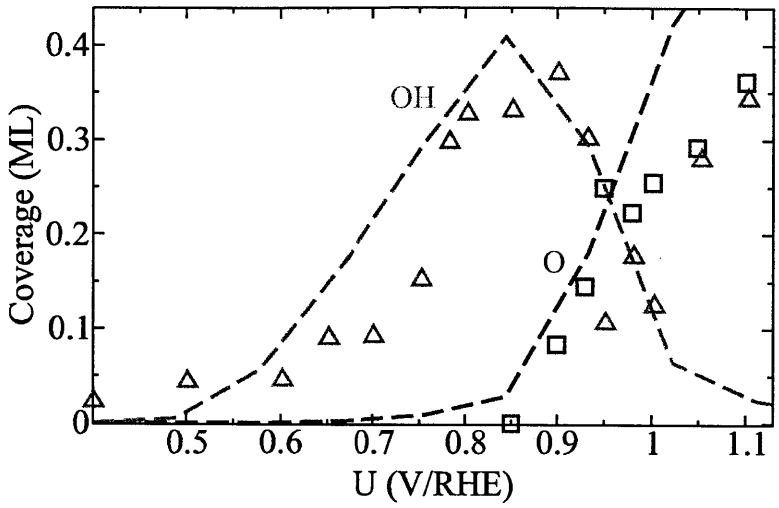

Figure 3-4: OH and O coverage on Pt(111) as a function of potential. Experimental points are from [88]. Dashed lines are fits obtained with parameters in the text.

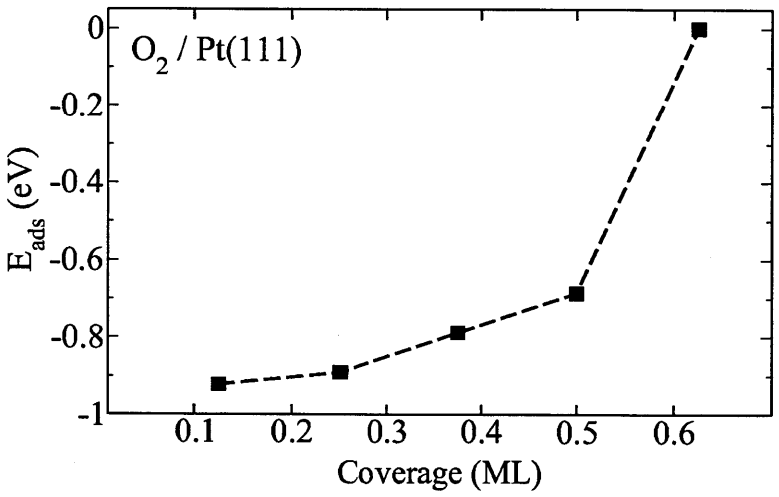

Figure 3-5: O_2 differential adsorption energy on Pt(111) vs. coverage.

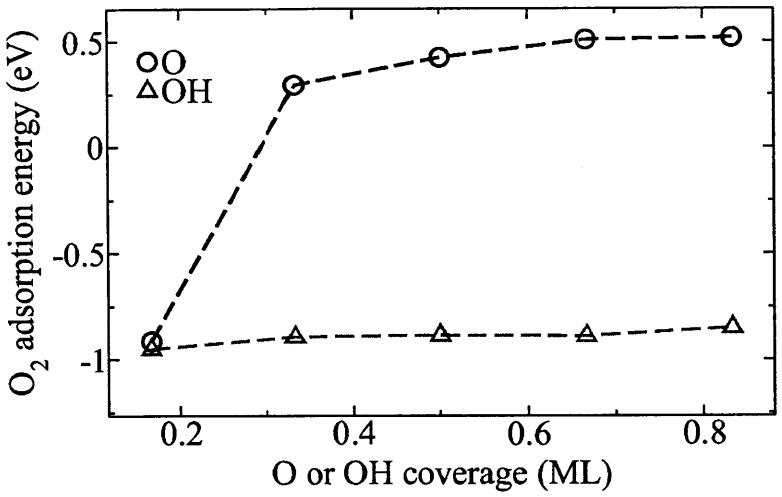

Figure 3-6: O_2 adsorption energy on Pt(111) with coadsorbates O or OH. O, OH and O_2 are on the fcc, atop and bridge sites respectively. O_2 is adsorbed at low coverage.

3.3.4.3 Adsorption from solution

The previous adsorption energies are defined for a molecule in the gas phase. However, in reaction (1), the O_2 molecule is adsorbed from solution, which requires to know how different its enthalpy is compared to the gas phase. This information is not directly available but can be derived from data on the solubility of dioxygen. Let us consider the dissolution reaction:

$$O_2(g) \rightarrow O_2(aq)$$

In general, the law of mass action for equilibrium introduces a reaction constant $K = e^{-\frac{\Delta G}{kT}}$, whose dependence in temperature gives rise to the van't Hoff law[18]:

$$\frac{d\ln K}{dT} = \frac{\Delta H}{kT^2}$$

For dissolution reactions, the law of mass action is known under the name of Henry's law, and the reaction constant k_H relates the concentration c of the solute to its pressure p in the gas phase at a given temperature. Namely, for oxygen, $k_H = \frac{c}{p} = 1.26 \times 10^{-3}$ mol/L·atm at 298 K. The temperature dependence of the solubility can be tabulated (see Table 3.7) in the

[18]Its derivation uses the fact that $\frac{\partial G}{\partial T} = S$.

Table 3.7: O_2 and CO solubility in water as a function of temperature (mole fraction).

T (K)	O_2	CO
288.15	2.756×10^{-5}	2.095×10^{-5}
293.15	2.501×10^{-5}	1.918×10^{-5}
298.15	2.293×10^{-5}	1.774×10^{-5}
303.15	2.122×10^{-5}	1.657×10^{-5}
308.15	1.982×10^{-5}	1.562×10^{-5}

following form:

$$k_H = k_H^\circ \exp\left[C\left(\frac{1}{T}-\frac{1}{T^\circ}\right)\right]$$

and identification with the van't Hoff law yields $\Delta H_{\text{solv}} = -kC$. For dioxygen, $C_{O_2} = 1461.41$ K, giving $\Delta H_{\text{solv}} = -0.13$ eV. As a consequence, Ts for dioxygen goes from 0.64 eV to 0.51 eV upon dissolution in standard conditions.

3.3.5 Kinetic equations

All elements are gathered for a full account of the dynamics on the surface. Based on Eqs. (3.10), (3.11) and (3.12), kinetic equations for the system are written and compiled in Table 3.8, embedding energy parameters introduced or calculated previously.

3.3.6 Steady state solution

At steady state, total time derivatives of species coverages are zero. The resulting system is non-linear in coverages, preventing a straightforward matrix inversion. One physical way to solve the dynamics would be to start away from equilibrium, e.g. with a bare surface, and integrate the equations of time until surface coverages reach convergence and steady state is established. However, this approach is in practice hindered by the very different orders of magnitude of various reaction rates, which would require a complicated treatment with different time steps. Instead then, we have found that a concatenated series of dichotomies on specific coverages chosen in the right order was sufficient to find the equilibrium state[19]:

(a) Choose a value for $\theta_O + \theta_{OH}$.

[19]Other methodologies for solving system kinetics, not necessarily within a given set of reaction paths, include kinetic Monte-Carlo algorithms [92, 93].

Table 3.8: Kinetic equations for our ORR model.

Step	Forward and backward currents	Rate constants[2]
(1)[1]	$i_{f1} = e\alpha_S \frac{d\theta_{O_2}}{dt} = k_{f1}(1-\theta)$	$k_{f1} = i_0 e^{-\frac{sg}{k}}$
	$i_{b1} = -e\alpha_S \frac{d\theta_{O_2}}{dt} = k_{b1}\theta_{O_2}$	$k_{b1} = i_0 e^{-\frac{\Delta E_{\text{des}}}{kT}}$
(2)	$i_{f2} = -e\alpha_S \frac{d\theta_{O_2}}{dt} = \frac{e\alpha_S}{2}\frac{d\theta_{OH}}{dt} = k_{f2}\theta_{O_2}(1-\theta)^2$	$k_{f2} = i_0 e^{-\frac{S^*}{k}} e^{-\frac{E^*_{f2}(U,\theta_s)}{kT}}$
	$i_{b2} = e\alpha_S \frac{d\theta_{O_2}}{dt} = -\frac{e\alpha_S}{2}\frac{d\theta_{OH}}{dt} = k_{b2}\theta^2_{OH}(1-\theta)$	$k_{b2} = i_0 e^{-\frac{S^*}{k}} e^{-\frac{E^*_{b2}(U,\theta_s)}{kT}}$
(3)	$i_{f3} = -e\alpha_S \frac{d\theta_O}{dt} = e\alpha_S \frac{d\theta_{OH}}{dt} = k_{f3}\theta_O(1-\theta)$	$k_{f3} = i_0 e^{-\frac{S^*}{k}} e^{-\frac{E^*_{f3}(U,\theta_s)}{kT}}$
	$i_{b3} = -e\alpha_S \frac{d\theta_{OH}}{dt} = e\alpha_S \frac{d\theta_O}{dt} = k_{b3}\theta_{OH}(1-\theta)$	$k_{b3} = i_0 e^{-\frac{S^*}{k}} e^{-\frac{E^*_{b3}(U,\theta_s)}{kT}}$
(4)	$i_{f4} = -e\alpha_S \frac{d\theta_{OH}}{dt} = k_{f4}\theta_{OH}$	$k_{f4} = i_0 e^{-\frac{S^*}{k}} e^{-\frac{E^*_{f4}(U,\theta_s)}{kT}}$
	$i_{b4} = e\alpha_S \frac{d\theta_{OH}}{dt} = k_{b4}(1-\theta)$	$k_{b4} = i_0 e^{-\frac{S^*}{k}} e^{-\frac{E^*_{b4}(U,\theta_s)}{kT}}$

[1] Beware of notation $\frac{d\theta_{\text{species}}}{dt}$ in these equations. It does not stand for the *total* time derivative of the species coverage, but only for the contribution of the considered current to that quantity. α_S is the surface atomic density.

[2] We define an exchange current:
$i_0 = e\alpha_S \frac{kT}{h} = (1.60 \times 10^{-19}\,\text{C}) \cdot (1.44 \times 10^{19}\,\text{m}^{-2}) \cdot (6.21 \times 10^{12}\,\text{s}^{-1}) = 1.43 \times 10^{12}\,\text{mA/cm}^2$.

(b) Choose a value for θ_{OH}; θ_O is the complement.

(c) Then, it is possible to compute θ_{O_2} by simply exploiting the steady state relation $\frac{d\theta_{O_2}}{dt} = 0$ (also solved by dichotomy).

(d) Knowing all coverages, i_{f3} and i_{b3} can be computed. If the overall reaction 3 is going forward (backward), θ_{OH} needs to be increased (decreased). For that, go back to (b) and adjust search interval accordingly. Keep going through steps (b)-(d) until convergence on θ_{OH} is reached. At this point, there is equilibrium between O and OH.

(e) Knowing all the coverages, it is possible to evaluate the term $\frac{d\theta_{OH}}{dt}$. If it is positive (negative), it means that coverage by OH (and O) has been underestimated (overestimated). Go back to (a) and adjust search interval accordingly. Go through steps (a)-(e) until complete convergence is reached.

3.3.7 Results and discussion

The oxygen reduction surface current is computed as $i_{ORR} = 4i_2 = 4(i_{f2} - i_{b2})$, after checking that reaction 2 is indeed the rate limiting step. The current is a function of input parameters:

$$i_{ORR} = f(a_1, a_{11}, a_2, a_{22}, \mathbf{a_3}, \mathbf{a_{33}}, a_{12}, a_{23}, a_{31}, \mathbf{E_{f2}^*}, \mathbf{S^*}, \mathbf{T}, \mathbf{U})$$

This is a large parameter set to explore, and all dependences do not present the same level of interest. Focusing on O_2 as being the reactant of the rate limiting step, we suggest to fix a_1, a_{11}, a_2, a_{22} and a_{12} at the values consistent with the spectroscopic results of Watanabe. For interactions between O_2 and coadsorbates, we choose representative values $a_{23} = 0.33$ eV and $a_{13} = 1.35$ eV. The remaining parameters subject to investigation are indicated in bold fonts. One method would be to vary the parameters, compute the current, and see how the result compares with experiment. More directly instructive to reveal interdependences is the converse approach that we propose. a_3 and a_{33} are allowed to vary freely within a certain range. For each pair of values, a set of simulations are performed with temperatures ranging from 270 to 330 K, and potentials ranging from 1.23 V to 0.4 V/RHE, from which two curves can be extracted: the polarization curve $i_{ORR}(U)$ and the Arrhenius plot $i_{ORR}(T)$. S^* and E_{f2}^* are adjusted on the fly so that those curves approach the experimental ones as closely as possible. This leads to the fitting relation:

$$(E_{f2}^*, S^*) = f(a_3, a_{33}) \tag{3.13}$$

Experimental results are taken from the study of Wang et al. for polarization curves[20] and from a study by Stamenković et al. for activation energies [95][21]. The plots for Eq. (3.13) are given in Fig. 3-7. Different scenarios emerge depending on the values of a_3 and a_{33} which can be classified in five zones. Physical considerations lead to eliminate certain scenarios as not plausible:

Zone 1 - Strong adsorption of O_2 on the surface combined with weak lateral interactions causes strong poisoning of the surface, requiring a negative value of S^* to reach the experimental current.

Zone 2 - Compared to zone 1, O_2-O_2 lateral interactions are slightly larger, thus reducing effective affinity of the molecule for the surface. Surface poisoning is still very important, but it is also more sensitive to temperature. Heating up the surface causes partial evaporation of the dioxygen layer. Subsequent creation of free sites is sufficient to increase substantially the oxygen reduction current, leading to a large value of the effective activation energy, above the experimental value. To compensate for that, the fitting algorithm has to reach negative values of the enthalpic barrier E^*, which is unphysical.

Zone 4 - Due to reduced binding energy, O_2 coverage on the surface has an intermediate value. Heating up the surface has the effect to reduce even more the coverage, bringing down the oxygen reduction current by lack of reactant. This leads to a negative value of the effective activation energy, which must be compensated by a very large E^*, up to 1.8 eV. This is far from DFT estimates in the range 0.3-0.6 eV.

At this point, only zones 3 and 5 remain as physical candidates. They significantly differ by their coverage in O_2. In zone 3, strong binding energy leads to high coverage, and large value of a_{33} limits poisoning. On the contrary, the weak binding energy in zone 5 leads to small coverages. When heating the surface, thermal activation of the first protonation reaction wins over evaporation, implying reasonable values of the effective activation energy. Figs. 3-8 and 3-9 are examples of the fit in zone 3. Exact values of the parameters are:

[20] Our kinetic model predicts the exchange current, i.e. the rate of electron transfer on the surface. Experimental currents also include possible mass transfer limitations to the electrode. One can either deduce the exchange current from the experimental measure, or include diffusion limitations besides the model exchange current to compute the total current. In case of a strong difference in orders of magnitude, one has to be aware of accuracy issues [94].

[21] They also discuss interesting effects. For instance, they argue that inverse proportionality of the Tafel slope vs. temperature observed in $HClO_4$ may come from oxide adsorption that is temperature dependent (by constrast with strong sulfate adsorption).

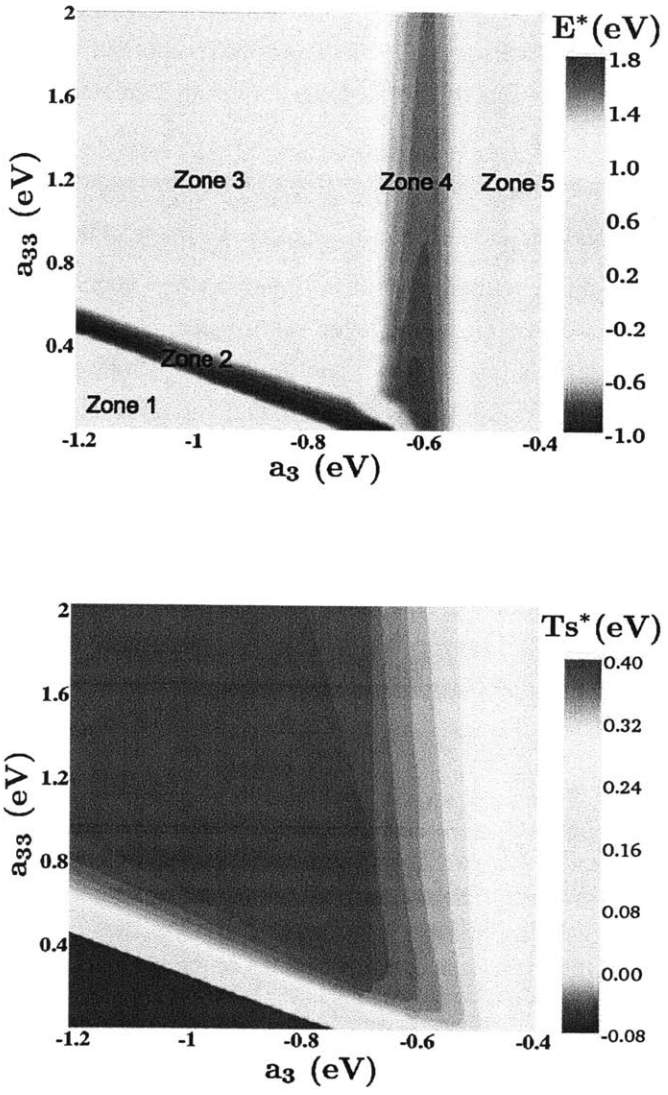

Figure 3-7: Enthalpic (top) and entropic (bottom) reaction barriers as a function of a_3 and a_{33}.

$E^*_{f2} = 0.40$ eV
$Ts^* = 0.43$ eV
$a_3 = -0.90$ eV
$a_{33} = 1.0$ eV

The experimental activation energy is correctly reproduced, as well as the transition of the Tafel slope from 60 to 120 mV/dec when increasing the overpotential. In this case, the Tafel slope change is mainly due to OH depletion, as was already suggested in the literature.

However, one more parameter has not been considered yet: oxygen pressure. An important feature of zone 3 is that O_2 is adsorbed at relatively high coverage, which is not easy to reconcile with a measured reaction order of 1. In the next section, the plausibility of weak adsorption in zone 5 is discussed.

3.3.8 O_2 dissociation?

Our sensitivity analysis tends to bring evidence for weak adsorption of O_2 on the surface (binding energy less than 0.4 eV). This should be on top of coadsorption effects which have already been included. Furthermore, DFT results indicate that O_2 binding energy is weakly dependent on OH, which is the main coadsorbate below the onset of ORR at 0.9 V/RHE.

The adsorption of O_2 on platinum surfaces has been the object of several experimental studies by Avery [96], Gland [97], Gland et al. [75], Steininger et al. [98]. Techniques included thermal desorption for binding energies, EELS for vibrational spectra, LEED for adsorption patterns, Auger electron spectroscopy, X-ray photemission spectroscopy and ultraviolet photemission spectroscopy for electronic structure. A common conclusion is that molecular adsorption predominates below 150 K, with no activation barrier as suggested by high sticking coefficients, while above 150 K, atomic adsorption occurs first. Adsorbed molecular oxygen is recognized by a vibrational band around 870 cm^{-1}, which is interpreted as the signature of a peroxo species O_2^{2-} with a bond order of 1, further supported by UPS showing that orbitals derived from $\pi_g^\star$ orbitals of molecular oxygen are filled in the adsorbed dioxygen complex. By contrast, adsorbed atomic oxygen is identified by a IR band around 490 cm^{-1}. The O_2 saturation coverage at 150 K is 0.4 ML. Upon heating, two thirds first evaporate, and the rest dissociates to form a 2×2 atomic oxygen structure. TDS peaks first at 150 K and then in the 400-600 K temperature range are associated with molecular and atomic oxygen desorptions respectively. The molecular state binding energy is evaluated around 37 kJ/mol. However, analysis of thermal desorption data is complicated by the onset of the atomization reaction which occurs during the desorption process. Interestingly, adsorption of molecular oxygen on

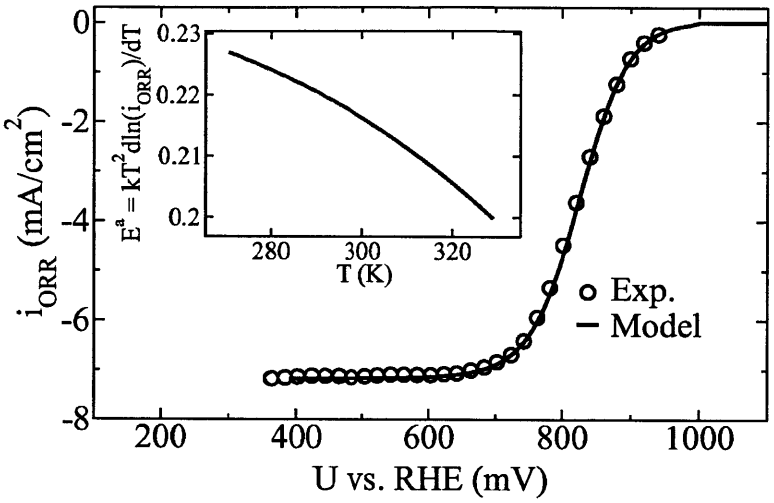

Figure 3-8: Polarization curve for typical scenario in zone 3, along with experimental data from [63]. Total current was computed by including mass transfer limitation assuming a RDE rotation speed of 2500 rpm. The inset is the activation energy at $\eta = 0.3$ V vs. temperature. The average value matches experiment [95].

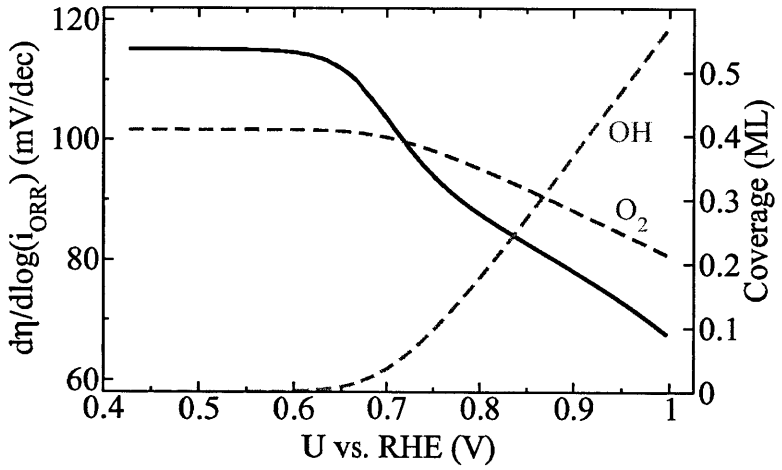

Figure 3-9: Tafel slope for polarization curve of Fig. 3-8 and adsorbate coverages ("strong" O_2 adsorption destabilizes O, which gets completely depleted below 1 V/RHE).

Table 3.9: Electronic configurations of O_2 and O.

	Electronic structure	Energy DFT-GGA/DFT-exp (eV)
O	$2s^2 2p^4\ (^3P_2)$	-430.53/-430.94
O_2	$(\sigma_s^b)^2(\sigma_s^\star)^2(\sigma_z^b)^2(\pi_{x,y}^b)^4(\pi_x^\star)^1(\pi_y^\star)^1$	-867.79/-867.16

top of a previously formed 2×2 structure is also observed and results in simple desorption kinetics, still around 150 K, due to the reduced probability of atomization during desorption. Incidentally, oxygen adsorption is responsible for a sizable change in the work function, up to a positive 0.8 V. In another work, Shao et al. used in-situ surface-enhanced infrared reflection absorption spectroscopy (SEIRAS) - with the advantage of large surface sensitivity - to study O_2 adsorption on platinum in alkaline medium. They found a feature around 1000 cm^{-1}, which they attributed to a superoxide anion (O_2^-) form of oxygen.

Arguing for weak binding energies below 0.4 eV - as suggested by the multiparameter analysis and experimental measures - using ab-initio calculations is not straightforward. Shao et al. found O_2 binding energies at low coverage to be 0.76 eV [64]. Our own calculations yield a binding energy at low coverage around 0.9 eV (Fig. 3-6). A possible source of discrepancy is DFT intrinsic errors. For instance, it is known that the triplet state of O_2 is not described accurately by DFT, leading to a wrong enthalpy for the following reaction:

$$H_2O \rightarrow \frac{1}{2}O_2 + H_2 \tag{3.14}$$

Therefore, in this work and similarly to [99], electronic energies and ZPEs (Table 3.5) of H_2O and H_2 were first calculated, then the energy of O_2 in the gas phase was deduced in order to match the experimental enthalpy of reaction (3.14). Table 3.4 gives a comparison of energies obtained direcly from DFT with those obtained by means of the thermodynamic manipulation. Here, we also report results when using pbe-van-bm pseudopotentials instead of pbe-rrkjus ones, along with electronic configurations of O_2 and O, and similar differences with respect to thermodynamically corrected values appear (Table 3.9). A difference of 0.5 eV appears in the case of O_2, so that O_2 binding energy approaches 0.4 eV if the gas phase energy is taken from DFT directly! In light of experimental observations and of calculations concerning O_2-O lateral interactions, another explanation would be to argue that atomic oxygen poisoning occurs at all potentials and is responsible for the weak effective O_2 binding energy. At high potentials (above 0.9 V/RHE), atomic oxygen is produced by water oxidation, as already included in the model; at lower potentials (below 0.9 V), the depletion of water discharge products makes

O_2 dissociation possible, until a self-poisoning oxygen coverage around a quarter monolayer makes the dissociation highly activated again, as suggested by our DFT calculations. Nolan et al. used EELS and molecular beam techniques to examine high translational energy adsorption of oxygen and estimated the dissociation barrier to be 0.29 eV [100]. At low O coverage, Liang et al. find a O_2 DFT dissociation barrier between 0.27 and 0.37 eV. These results imply that partial dissociation on the surface would be kinetically possible before O_2 reduction proceeds with a barrier around 0.4 eV. Dissociative atomic oxygen saturation at coverage 1/4 followed by weakly bound molecular adsorption is in addition consistent with experiments described previously. Interestingly, the possibility of this phenomenon can be related to a remark by Rossmeisl et al. that there is no systematic one-to-one correspondence between shifts in polarization curve potentials and OH coverage changes given by shifts in voltammogram half-wave potentials [101]. However, they gave a different interpretation, arguing for a change of the rate-limiting step on different surfaces based on their Sabatier analysis. The O_2 dissociation mechanism was not captured in our kinetic model because it is a transient. The deductive path that we followed illustrates current difficulties to understand ORR. Progress in experiment and ab-initio predictions have certainly shed some light on the mechanism, but information especially on the detailed nature of the surface as the reaction proceeds remains to be gained.

3.4 Conclusion

In this chapter, we developed a kinetic model of ORR on Pt(111) and performed a sensitivity analysis to obtain constraints on energy predictions. The choice of reactions and several assumptions are based on previous experimental and DFT findings. Predicted currents are compared with accurate polarization curves on the well-defined Pt(111) surface. Interestingly, we found that DFT intrinsic uncertainties overlap with quite different ORR scenarios, having to do with O_2 binding energy and coverage on the surface. Poisoning effects are usually seen to originate from parallel reactions, namely water oxidation on the surface at sufficiently high potentials. Here, we show that O_2 self-poisoning by transient dissociation at low coverage is consistent with kinetic and energetic considerations, and could be one more source of ORR sluggishness. If so, preventing O_2 initial dissociation could be one more guideline for ORR catalyst design.

Chapter 4

Electrostatics of Isolated Charged Systems

4.1 Electrostatics in vacuum

4.1.1 Corrective potential

Working in periodic boundary conditions allows the convenient use of plane-wave formalism combined with efficient fast Fourier transform techniques (see App. D). As a consequence, when studying a supposedly isolated molecule or a system of finite extent in some direction, the potential profile obtained in the unit cell is not the one from that single item, but rather from the full array including its periodic images. One implication is that no reference vacuum potential can be extracted from the calculation, which is a problem for electrochemical applications. Another consequence is that the realistic study of charged systems is precluded, as the energy of an infinitely charged system diverges. Denoting v the exact potential of the isolated system under study (neutral or charged), it satisfies the Poisson equation:

$$\nabla^2 v(\mathbf{r}) = -4\pi\rho(\mathbf{r})$$

with adequate boundary conditions. By contrast, the potential calculated in periodic-boundary conditions is denoted v'. The use of Fourier transforms in the calculation of the potential from the charge density introduces an artificial jellium background that neutralizes the system:

$$\nabla^2 v'(\mathbf{r}) = -4\pi(\rho(\mathbf{r}) - \langle\rho\rangle)$$

and v' is determined from:

$$v'(\mathbf{r}) = \sum_{\mathbf{g}\neq 0} \frac{4\pi}{\mathbf{g}^2}\rho(\mathbf{g})e^{i\mathbf{g}\cdot\mathbf{r}}$$

Therefore, the exact potential can be recovered by adding to v' a corrective potential satisfying the equation:

$$\nabla^2 v_{\text{corr}}(\mathbf{r}) = -4\pi\langle\rho\rangle \tag{4.1}$$

with adequate boundary conditions. Additional development of a correction scheme in Quantum-ESPRESSO has been done in collaboration with I. Dabo, in continuation of his primary work, described in [102].

4.1.2 Numerical scheme

There are several methods to find the exact potential, with different computational costs. Here, N denotes the number of grid points (in real or reciprocal space) in the unit cell.

Direct real-space resolution - Bypassing the corrective potential, the exact potential can be computed directly from the Green's functions approach:

$$v(\mathbf{r}) = \int \frac{\rho(\mathbf{r}')}{|\mathbf{r}-\mathbf{r}'|} d\mathbf{r}'$$

The computational cost is in $O(N^2)$. The corrective potential is then simply $v - v'$.

FFT and corrective potential - As mentioned in the previous section, a natural way to proceed is to first find the periodic potential v' by means of FFT techniques. The cost of that step is in $O(N\log N)$. The corrective potential is smoother than v' and v, it can therefore be determined on a coarser mesh with M grid points. Using multigrid techniques, Eq. (4.1) can be solved with a cost in $O(M\log M)$. Evaluating boundary conditions is actually more expensive, with a cost in $O(M^{5/3})$.

Two-dimensional periodicity - Periodicity in one or more directions opens the way to Fourier analysis. The 2D case was specifically studied by Otani and Sugino [103]. Assuming periodicity in x and y directions, the corrective potential can be expanded into:

$$v_{\text{corr}}(\mathbf{r}_\parallel, z) = \sum v_{\text{corr}}(\mathbf{g}_\parallel, z) e^{i\mathbf{g}_\parallel \cdot \mathbf{r}_\parallel}$$

taking the laplacian:

$$\nabla^2 v_{\text{corr}} = \sum \frac{d^2 v_{\text{corr}}(\mathbf{g}_\parallel, z)}{dz^2} e^{i\mathbf{g}_\parallel \cdot \mathbf{r}_\parallel} - \sum v_{\text{corr}}(\mathbf{g}_\parallel, z) g_\parallel^2 e^{i\mathbf{g}_\parallel \cdot \mathbf{r}_\parallel}$$

Identification with the right-hand side of Eq. (4.1) gives:

$$\begin{aligned} g_\parallel = 0 \;&\Rightarrow\; \frac{d^2 v_{\text{corr}}(0,z)}{dz^2} = -4\pi\langle\rho\rangle \\ &\Rightarrow\; v_{\text{corr}}(0,z) = -2\pi\langle\rho\rangle z^2 + az + b \end{aligned}$$

$$\begin{aligned} g_\parallel \neq 0 \;&\Rightarrow\; \left(\frac{d^2}{dz^2} - g_\parallel^2\right) v_{\text{corr}}(\mathbf{g}_\parallel, z) = 0 \\ &\Rightarrow\; v_{\text{corr}}(\mathbf{g}_\parallel, z) = Ae^{g_\parallel z} + Be^{-g_\parallel z} \end{aligned}$$

Coefficients a and b and, for each $\mathbf{g}_\parallel$, A and B, are obtained from boundary conditions on the left ($z = 0$) and the right ($z = L$) of the unit cell, computed by using Green's functions of the Fourier components of a periodic surface charge. It leads to:

$$\begin{aligned} v(0,0) &= -2\pi \int |z|\, \rho(0,z) dz \\ v(0,L) &= -2\pi \int |L-z|\, \rho(0,z) dz \end{aligned}$$

$$\begin{aligned} v(\mathbf{g}_\parallel, 0) &= 2\pi \int \frac{e^{-g_\parallel |z|}}{g_\parallel} \rho(\mathbf{g}_\parallel, z) dz \\ v(\mathbf{g}_\parallel, L) &= 2\pi \int \frac{e^{-g_\parallel |L-z|}}{g_\parallel} \rho(\mathbf{g}_\parallel, z) dz \end{aligned}$$

In-plane FFTs to obtain $\rho(\mathbf{g}_\parallel, z)$ cost $O(KN^{2/3}\log N^{2/3})$, where K is the number of planes that do contain a charge. Computation of boundary conditions costs $O(KN^{2/3})$, therefore at most $O(N)$. Finally, in-plane FFTs to get the charge density in real space have a cost in $O(N^{1/3} \times N^{2/3}\log N^{2/3})$. The overall cost is then in $O(N\log N)$.

4.1.3 Corrective energy and force

Adding v_{corr} to v' at the end of a self-consistent cycle in Quantum-ESPRESSO ensures that the potential used for the next cycle is the exact potential corresponding to the explicit charge density distribution inside the unit cell. However, the total energy and forces on ions are computed using v'. Therefore, a correction is required for them as well. It turns out that:

$$E_{\text{corr}} = \frac{1}{2} \int (\rho_i(\mathbf{r}) - \rho_e(\mathbf{r})) v_{\text{corr}}(\mathbf{r}) d\mathbf{r}$$

ρ_i and ρ_e being the ionic and electronic charge densities respectively. And:

$$F_{\text{corr}} = -q_{\text{ion}} \nabla v_{corr}$$

4.2 Electrostatics in solution

4.2.1 The double layer

In an electrochemical system, the electrode is immersed in an electrolyte, with the presence of water as a solvent in proton-exchange devices. The electrode potential varies as a function of the net charge present at the surface (an excess or a deficit of electrons). Overall charge neutrality is maintained by electrolyte ions of opposite charge that accumulate near the electrode surface. Because of that screening effect, the electrostatic potential becomes flat in the bulk of the electrolyte, thus defining a reference potential $v(\infty) = 0$. Classical models for this electrochemical double-layer include the Helmholtz model, the Gouy-Chapman model, and a combination of the two, known as Stern-Gouy-Chapman model [104]. Ions in solution which do not adsorb on the electrode are assumed to keep a minimum distance to the surface, given by the outer Helmholtz plane (OHP). The region between the surface and the OHP is called compact layer. Outside this region, ions are free to diffuse in solution, hence the name of diffuse layer. When the system is charged, ion concentrations in the diffuse layer differ from their bulk values. The diffuse layer thickness is given by a characteristic quantity $1/\kappa$ which is a function of ion concentration. For instance, it is 3 Å for a concentration of 1 M, 9.6 Å for 10^{-1} M, 30.4 Å for 10^{-2} M, 96.2 Å for 10^{-3} M.

Then, the double layer is a complex region, where chemical interactions coexist with long-range electrostatic phenomena. In the context of ab-initio electrochemical calculations, the goal is to find a way to describe interactions in the double layer [105], while coping with characteristic lengths that can quickly exceed the size of reasonable unit cells.

4.2.2 First-principles simulations under electric bias

Here, a review of some of the strategies found in the literature is provided:

> Rather than to explicitly charge the system, one method is to simply apply an external field across the unit cell, as a way to model the electrostatic field inside the double layer. This approach has been in particular used by **Nørskov et al.** for studying the effect of field on adsorption energies [106].

A second level of simplification is to replace water with a dielectric continuum, with parameters to capture the behavior of water in the interfacial region. In particular, the work of Dabo et al. is based on a continuum solvent model introduced by Fattebert and Gygi, in which the dielectric constant ε is taken to be locally dependent on the quantum charge density ρ [115]. Precisely, an analytical formula is devised so that the permittivity goes smoothly to 1 in regions of high charge density, where the solvent cannot penetrate:

$$\varepsilon(\rho) = 1 + \frac{\varepsilon_\infty - 1}{2}\left(1 + \frac{1-(\rho/\rho_0)^{2\beta}}{1+(\rho/\rho_0)^{2\beta}}\right)$$

ε_∞ is the permittivity in the bulk of the solvent, ρ_0 is an adequately chosen charge density cutoff, and β is a parameter that controls the smoothness of the permittivity transition. This parameter is fitted so that solvation energies of a representative set of neutral and charged species are correctly predicted [116].

However, one issue is that β has also been shown to be correlated with the surface dipole, and as such, it should in general be a function of the surface chemistry. Trasatti studied the potential of zero charge vs. the work function in vacuum for different *sp* and *d* metals and different facet orientations, and established that the reduction of the work function upon solvation is proportional to the chemical affinity between the metal surface and water and, likewise, is related to the surface atomic density, in the order (111) < (100) < (110) [117, 118]. Therefore, a continuum model should be adopted with the caveat that additional specific interactions may have to be included.

In general, the chemical and electrostatic behavior of water on transition metal surfaces is notoriously difficult. More experiments are required to completely elucidate the structure of water on different substrates and its sensitivity to specific factors. Computational approaches have to tackle a system with numerous local minima, and be informed of uncertainties inherent to the DFT description of water-water and water-metal interactions. The behavior of water in strong electric fields as encountered in the double layer is more precisely the topic of chapter 7.

4.2.4 Simulations at fixed potential

Recently, more sophistication has been added to the description of charged systems with the ability to perform simulations at fixed voltage directly [119, 120].

Lozovoi and Alavi have used a model in which the counterions are represented by a charged layer in the vacuum region, providing the desired screening effect for defining a reference potential [107]. Non-linear capacitance effects associated with the diffuse layer are not included.

In the method of **Neurock et al.**, the electrode potential is also tuned by adding explicit charge on the surface, but the counter-charge distribution is a uniform background [108]. This method was applied to assess the binding energy of oxygen on platinum as a function of potential [109].

The model of **Otani and Sugino** can handle a counter-ion density immersed in a solvent continuum, characterized by a relative permittivity ε [103]. In addition, explicit molecules and ions can be added in the double layer. The presence of a counter-electrode is equally possible by setting $\varepsilon = +\infty$ in the corresponding region. Electrostatics are treated by resorting to the Green's function formalism, and the presence of ions requires to solve a Poisson-Boltzmann equation.

The model of **Dabo** is equally suited for capturing diffuse layer effects. The Poisson-Boltzmann equation is solved by multigrid techniques and imposing realistic boundary conditions [110]. A model by **Jinnouchi and Anderson** was developed along the same lines [111].

In the approach of **Skúlason et al.**, the counter-ion distribution is an explicit set of hydronium ions added among water molecules [112]. The electrode potential is controlled by changing the number of ions and neutralizing electrons on the surface. A possible drawback is that sufficiently large unit cells are required so that the resulting surface charge is not too high, and extrapolation schemes are needed between integer charges.

Using their models, Otani et al. and Skúlason et al. studied the Volmer step of the hydrogen evolution reaction [113, 114].

4.2.3 The case of water

Approaches described above have in common to include a screening effect from which a reference potential can be defined. One additional source of complexity is the presence of water. Water can be described with the same degree of accuracy as the solute (e.g. by means of Car-Parinello molecular dynamics), with limitations from computation power to be considered. A first level of simplification is offered by QM-MM methods, in which, typically, solvent-solvent and solute-solvent interactions are reduced to electrostatic and van der Waals terms (the latter having the form of a Lennard-Jones potential).

Chapter 5

Nature of the Stretching Frequency Shift of CO on Pt(111) under Potential Bias

5.1 Chemistry vs. electrostatics

A wide body of literature has been devoted to the chemisorption and infrared spectra of carbon monoxide on transition metal surfaces. Trends across surface chemistries and adsorption sites have been successfully rationalized in terms of the interaction between the metal *d* states and the CO 5σ and $2\pi^*$ orbitals [121, 122, 123]. Specifically, the red shift of the CO stretching frequency ν_{CO} has been related to the amount of electron back-donation from the metal to the antibonding $2\pi^*$ orbital, which in turn can be linked to the position of electronic levels at the metal surface[1]. In parallel, electrochemical experiments have been performed in which the CO vibrational frequency is measured as a function of electrode bias [124]. In line with previous developments, the red shift observed upon negative potentials was first viewed as a change in chemical bonding. Later, this interpretation was challenged by studies proposing an electrostatic mechanism akin to a Stark tuning effect.

The goal of this paper is to bring complete clarification as to the nature of the potential dependence of the CO stretching frequency on platinum in UHV conditions. First, a brief summary of previous studies and methodologies is provided to pose the problem in terms of an alternative between chemical and electrostatic explanations. Then, a first-principles scheme allowing for an exact treatment of charged systems is presented and applied to calculate the CO stretching frequency under potential bias using three different methods: transferring charge to the system, applying an external electric field, and resorting to perturbation theory. Finally, a discussion of the results concludes about the validity of the Stark tuning effect interpretation,

[1] By contrast, adsorption on an oxide can give rise to a violet shift.

and emphasizes the conceptual importance of metal screening.

In an electrochemical setup, the potential varies as a function of the net charge density present at the metal surface. Adding electrons causes an upshift of the Fermi level, while simultaneously an electric field is created outside the electrode. Initial studies investigated the CO stretching mode in connexion with the position of the Fermi level. S. Mehandru and A. Anderson proposed a model in which the electron affinity of Pt was tunable, which led them to attribute the calculated red shift to an enhancement of the electronic back-donation mechanism [125]. Then, first-principles studies employed the converse approach, applying an external electric field F in place of the potential bias. They found vibrational shifts in qualitative agreement with experiment and proved that similar results could be obtained from perturbation theory, implying that chemical effects are negligible [126, 127, 128]. However, it is not completely clear whether this approach is an adequate description of reality, as no charge is added on the electrode. Therefore, at an intermediate level, some studies used an external electric field while interpreting the results in light of a charge density transfer to the CO molecule, concluding that the field does perturb the chemical bonding [129, 130, 131, 132, 133]. Incidentally, more recent studies also insist on the importance of substrate geometry for reliable predictions. When modeling the Pt surface as a cluster, A. Lozovoi and A. Alavi find a CO vibration tuning rate $\frac{d\nu_{CO}}{dF}$ in the range 102-120 $cm^{-1}V^{-1}Å$, whereas slab calculations give 45.2 $cm^{-1}V^{-1}Å$ [136], in much better agreement with the experimental value of 56 $cm^{-1}V^{-1}Å$ [124]. Finally, I. Dabo et al. showed that careful modeling of the electrochemical double layer led to equally satisfactory predictions of the vibration tuning rate in aqueous environment [119].

5.2 Determining the stretching frequency shift

5.2.1 Computational setup

Here, ab-initio calculations are performed using the Quantum-ESPRESSO package [137]. The metal surface is represented by a 4-layer slab with normal z in the [111] direction and a lattice parameter of 4.0 Å (Fig. 5-1). The CO molecule is adsorbed on one side of the slab within a $(2 \times \sqrt{3})$ unit cell, implying a coverage of 1/4. The PBE density functional is used in combination with ultrasoft pseudopotentials for ionic cores. The plane-wave cutoff is 30 Ry, and a 7×7×1 k-point mesh is used for Brillouin zone sampling. Because of the plane-wave formalism, periodic images of the slab in the z-direction are implicitly included in the calculation. Exact treatment of the electrostatics of the isolated, possibly charged, system is achieved by means of a correction scheme described in [102]. The exact electrostatic potential v in the unit cell is obtained as the sum of the periodic potential v' and a corrective potential v_{corr}, satisfying

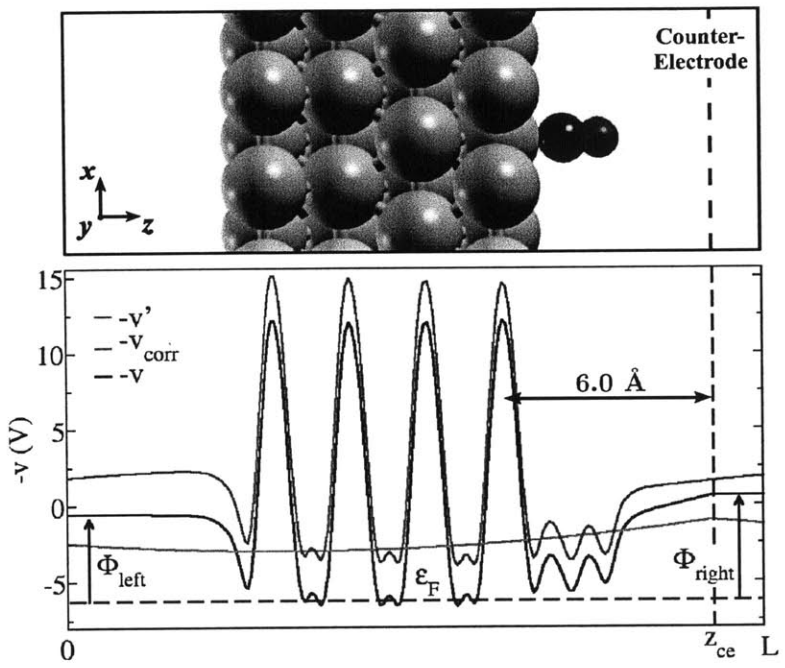

Figure 5-1: Longitudinal view of the setup. CO is adsorbed on a 4-layer Pt slab, a planar counter-electrode is placed 6 Å from the metal surface. A correction is applied so that the electrostatic potential in the unit cell is the exact contribution from the isolated slab and the counter-electrode. Here, $-v$ is plotted to visualize the potential of electrons.

the equation

$$\nabla^2 v_{corr} = -4\pi\langle\rho\rangle$$

where $\langle\rho\rangle$ is the average charge density (ions + electrons), while boundary conditions are enforced at the two extremities of the unit cell using Green's functions. As a result, the average potential drop across the unit cell is correctly related to the system dipole (per unit area) p [134, 135]:

$$v_{xy}(L) - v_{xy}(0) = 4\pi p \tag{5.1}$$

where $p = \int_0^L z\rho_{xy}(z)dz$, the subscript $_{xy}$ standing for quantities averaged in the xy plane. For cases where a net charge is present on the slab, a fictitious counter-electrode with opposite charge uniformely distributed in the xy plane is placed at a distance of 6 Å from the metal surface holding the CO molecule. The screening potential v_{ce} from the counter-electrode is included in the corrective potential, ensuring that the total potential v converges to flat values on both ends of the unit cell. An absolute potential Φ can then be definied on each side:

$$\Phi_{left} = -v_{xy}(0) - \varepsilon_F \tag{5.2}$$

$$\Phi_{right} = -v_{xy}(L) - \varepsilon_F \tag{5.3}$$

where ε_F is the Fermi level. Incidentally, comparison of Eqs. (5.1) and (5.3)–(5.2) implies:

$$\Phi_{right} = \Phi_{left} - 4\pi p \tag{5.4}$$

5.2.2 Methods

Using that setup, the CO stretching frequency under potential bias is determined using three different methods:

Method 1 - The system is put under bias by transferring a fraction of electron from the slab to the counter-electrode (or reciprocally). Surface charges σ from -7.1 μC/cm^2 to 7.1 μC/cm^2 are considered, generating electric fields $F = 4\pi\sigma$ from -0.8 V/Å to 0.8 V/Å between the two electrodes. For every given surface charge, the CO molecule and the topmost metal layer are fully relaxed. Then, a set of four calculations are performed where C and O are displaced around their equilibrium positions. The 2×2 dynamical matrix is computed by taking finite differences of the forces and the CO stretching frequency is obtained from the larger eigen-

value of the matrix.

Method 2 - An external electric field is applied on the slab. This is achieved by placing charge on the counter-electrode while keeping the slab neutral. To obtain the same magnitude of fields as in method 1, twice the amount of charge has to be taken. The reason for the factor 2 is that here only the counter-electrode contributes to the field, while in method 1 fields from both electrodes were adding up. Then, for every given field, the same procedure as in method 1 is used to get the CO vibration frequency.

Method 3 - The $\nu_{CO}(F)$ dependence is computed using perturbation theory. Keeping the system neutral with no field applied, a set of 25 calculations are performed where C and O are displaced around their equilibrium positions: $z_c = z_c^{eq} + \zeta_c$, $z_o = z_o^{eq} + \zeta_o$. The total energy per unit area E_0, and the dipole p, obtained from Eq. (5.1), are expressed as third-degree polynomials of ζ_c and ζ_o:

$$E_0 = \sum_{0 \le j \le i}^{3} a_{ij} \zeta_c^{i-j} \zeta_o^j \tag{5.5}$$

$$p = \sum_{0 \le j \le i}^{3} b_{ij} \zeta_c^{i-j} \zeta_o^j \tag{5.6}$$

where the 10 coefficients a_{ij} (resp. b_{ij}) are found by a least-square fit on the 25 values of E_0 (resp. p)[2]. In the linear response regime, the energy change of the system per unit area in an external electric field F is equal to $-F \times p$, from which the energy becomes:

[2]Here is how it goes, with the dipole for instance:
A set of m measures are taken where the dipole is reported as a function of positions. The dipole is not a linear function of positions, but rather is expressed as a polynomial of degree 3. The matrix of explanatory variables, also called design matrix, has m rows and 10 columns:

$$X = \begin{pmatrix} 1 & \zeta_{c,1} & \zeta_{o,1} & \zeta_{c,1}^2 & \cdots & \zeta_{c,1}\zeta_{o,1}^2 & \zeta_{o,1}^3 \\ 1 & \zeta_{c,2} & \zeta_{o,2} & \zeta_{c,2}^2 & \cdots & \zeta_{c,2}\zeta_{o,2}^2 & \zeta_{o,2}^3 \\ & & & \vdots & & & \\ 1 & \zeta_{c,m} & \zeta_{o,m} & \zeta_{c,m}^2 & \cdots & \zeta_{c,m}\zeta_{o,m}^2 & \zeta_{o,m}^3 \end{pmatrix}$$

Denoting β the vector of unknown coefficients and Y the vector of measures, we have:

$$\beta^t = (b_{00}, b_{10}, b_{01}, b_{20}, ..., b_{12}, b_{03})$$

$$Y^t = (p_1, p_2, ..., p_m)$$

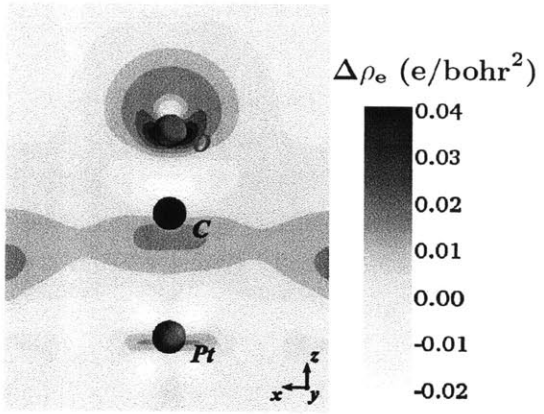

Figure 5-2: Excess electron density (integrated over y) after charging up the system. 0.08 e^- is added, corresponding to a surface charge of -4.4 μC/cm^2. Part of the charge accumulates in the electron spillover plane of the metal, while the rest is transferred to the CO molecule.

$$E = E_0 - Fp = \sum_{0 \le j \le i}^{3} c_{ij} \zeta_c^{i-j} \zeta_o^{j} \tag{5.7}$$

with $c_{ij} = a_{ij} - F b_{ij}$. Equilibrium displacements $\zeta_c^{eq}(F)$ and $\zeta_o^{eq}(F)$ are found at the energy minimum $(\frac{\partial E}{\partial \zeta_c})_{\zeta_c^{eq}} = (\frac{\partial E}{\partial \zeta_o})_{\zeta_o^{eq}} = 0$, and the dynamical matrix is derived from second-order derivatives of the energy evaluated at ζ_c^{eq} and ζ_o^{eq}, allowing for determination of $\nu_{CO}(F)$.

5.2.3 Results

CO stretching frequencies determined by the three methods are identical (Fig. 5-3). The tuning rate at the origin is 48.6 cm^{-1}V^{-1}Å, in agreement with previous studies [136, 119], and the experimental value of 56 cm^{-1}V^{-1}Å [124].

5.3 Discussion

Implications from those results are:

Eq. (5.6), $X\beta = Y$, implies minimization of the quantity $||Y - X\beta||^2$. Expanding:

$$||Y - X\beta||^2 = Y^t Y - \beta^t X^t Y - Y^t X\beta + \beta^t X^t X\beta$$

Differentiating with respect to β:

$$0 = -2X^t Y + 2X^t X\beta$$

from which we get:

$$\beta = (X^t X)^{-1} X^t Y$$

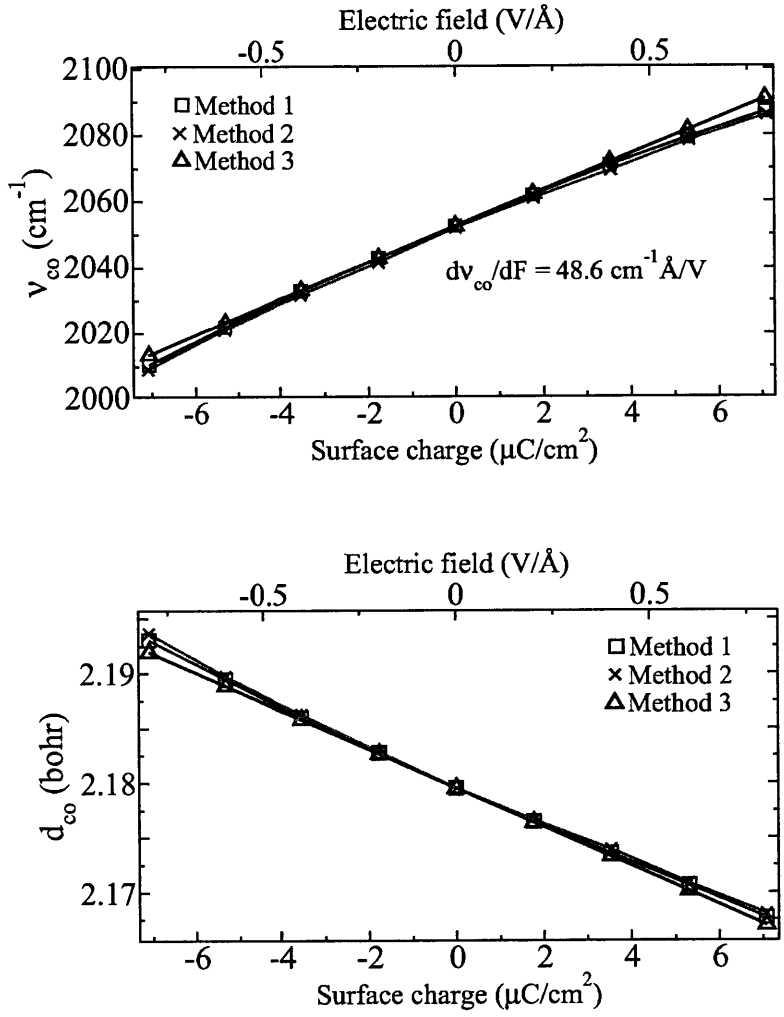

Figure 5-3: CO stretching frequency and inter-atomic distance as a function of excess charge (method 1) or external electric field (methods 2 and 3).

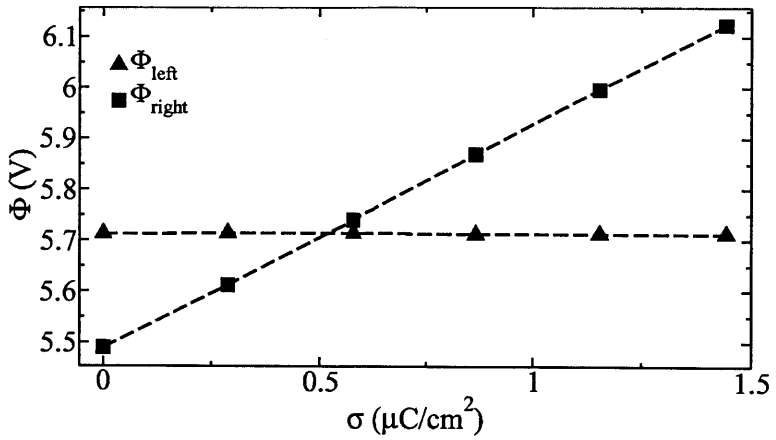

Figure 5-4: Absolute potentials on each side of the slab as a function of surface charge.

(i) applying an external electric field is a valid approach to reproduce experiments where charge is added to the electrode;

(ii) the tuning rate is predictable from the z_c, z_o-dependence of the energy and dipole in zero field, which proves that polarization effects and chemical changes are negligible, as implied by the Stark effect interpretation;

(iii) it is only at higher charge/field, when the fully variational values start to slightly deviate from linearity, that chemistry does have an effect.

To rationalize point (i), one could argue that the charge placed on the metal surface generates a field that acts on CO exactly like the external field. However, at the electronic level, there is no clear frontier between the metal surface and the CO molecule. In fact, plots of the charge density reveal that part of the charge added to the slab is transferred to CO orbitals (Fig. 5-2). More instructive is the behavior of absolute potentials upon slab charging (Fig. 5-4). Φ_{left} remains constant, while Φ_{right} varies linearly with the charge, demonstrating the effect of metal screening at the atomistic level. Similarly, it can be shown that Φ_{left} is unaffected by C and O displacements:

$$\frac{\partial \Phi_{\text{left}}}{\partial \zeta_c} = \frac{\partial \Phi_{\text{left}}}{\partial \zeta_o} = 0 \tag{5.8}$$

When a surface charge σ is transferred from the counter-electrode to the slab, the first-order change in energy per unit area is $\sigma\Phi_{\text{right}}$, and combining with Eq. (5.4), the energy becomes

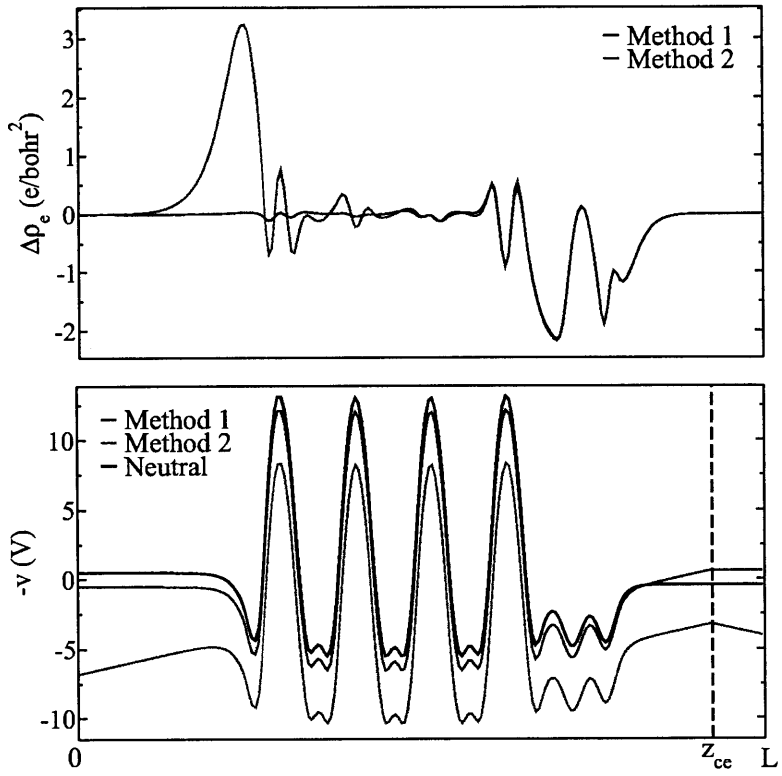

Figure 5-5: Excess electron density and potential. **Method 1**: 0.08 e^- is transferred from the slab to the counter-electrode, corresponding to a surface charge of 4.4μC/cm^2. **Method 2**: 0.16 e^- is placed on the counter-electrode, corresponding to an external field of 0.5 V/Å applied on the neutral slab. Only the charge density on the slab is represented, the one on the counter-electrode is implicit.

$E = E_0 + \sigma\Phi_{\text{left}} - 4\pi\sigma p$. From Eqs. (5.5), (5.6) and (5.8), it follows:

$$E = \sum_{0\leq j\leq i}^{3} c_{ij}\zeta_c^{i-j}\zeta_o^j \tag{5.9}$$

with $c_{00} = a_{00} + \sigma\Phi_{\text{left}} - 4\pi\sigma b_{00}$, and for $i \geq 1$, $c_{ij} = a_{ij} - 4\pi\sigma b_{ij}$. Similarity of Eqs. (5.7) and (5.9) and the fact that ν_{co} is only a function of the $(c_{ij})_{i\geq 1}$ confirm that the tuning rate from adding a charge is equal to the one from applying a field, with the correspondance $F = 4\pi\sigma$.

Further visualization of the role of metal screening is brought by comparison of charge densities and potentials as obtained from methods 1 and 2 (Fig. 5-5). When transferring charge from the counter-electrode to the slab, the equilibrium excess charge density on the slab is localized to the surface facing the counter-electrode. When having twice the charge on the counter-electrode while keeping the slab neutral, two opposite surface charge densities build up on each side of the slab in order to screen the external field. The two charge densities appearing on the right-hand side of the slab from methods 1 and 2 are perfectly identical, illustrating the validity of classical models of the metal down to the atomic scale, and bringing additional insight into the electrostatic nature of the $\nu_{\text{co}}(\sigma)$ dependence. In this case, it should be stressed that the CO molecule becomes part of the metal. The partial charge transfer occurring on CO has no effect on the vibrational tuning rate, as revealed by the perturbative approach. Rather, it is a signature of the presence of CO orbitals in the hybridized states at the Fermi level. Suppression of the HOMO-LUMO gap upon adsorption is constitutive of the complete metallization of the system, a requirement for the screening effect to be fully operative.

5.4 Conclusion

In summary, a first-principles scheme has been developed in which the potential of an electrode is realistically monitored by adding charge to the system. Comparison with the external electric field method and the perturbative approach has demonstrated that the potential dependence of the CO stretching frequency can be reduced to a purely electrostatic mechanism, in spite of charge density transfers occurring on the surface. Screening effects from the metal are identified as the key concept for full rationalization. It should however be reminded that chemical effects start being significant for strongly charged systems. This can be in particular the case for nanoparticles on oxide supports [138].

Chapter 6

Hydrogen Under-Potential Deposition on Platinum: Effect on Nanoparticle Equilibrium Shape

After addressing the main aspects of reaction mechanism and activation barrier, theoretical studies have been increasingly emphasizing the importance of the catalyst surface state in rationalizing differences in activities. Experimental availability of pure single crystals has brought evidence of the significance of facet orientation for reactivity [38]. Other studies have related improved catalytic activities to a reduction in adsorbate surface coverage mitigating the site-blocking effect [50]. On the modeling side, ab-initio methods are pursuing increased accuracy and have been successively applied to extract valuable predictors [44]. Open to more thorough investigation is the structure of the electrochemical double layer. While the effect of potential bias has been sometimes included by application of an external electric field, converse approaches playing with charge non-neutrality have emerged [110, 103, 112].

6.1 Electrochemical equilibrium at the electrode - electrolyte interface

The purpose of this section is to obtain fundamental equations of electrochemistry for a surface in a unified way. In the original derivation of Gibbs adsorption isotherm, a concept of surface excess concentration is used. The present derivation is a variant which ensures correct treatment of cases where some species only exist at the interface. It is notably true when an *electrosorption* reaction occurs, by which a species in solution, A^n, is adsorbed on the surface

and reduced (or oxidized) in the process[1]:

$$A^n + * + ne^- \rightarrow A^*$$

Let then an electrode - of potential Φ_e - be connected to an electron reservoir of potential Φ. Electrons in the reservoir have energy $-e\Phi$. Let us consider the process by which the electrode surface area is increased by S_a, costing an energy $S_a\gamma$, where γ is the surface energy. $G(N,q)$ is the electrode Gibbs free energy per surface area S_a, assuming the presence of N electrosorbed molecules A and q free charges. The electrode consists of M metal atoms per surface area S_a, with chemical potential $\mu(M)$. $\mu(A^n)$ is the chemical potential of A^n in solution. We find an expression for γ by writing the energy balance during the surface creation process:

$$S_a\gamma = G(N,q) - M\mu(M) - N\mu(A^n) + (Nne - q)\Phi$$

Subtracting $S_a\gamma_0 = G(0,0) - M\mu(M)$ (γ_0 being the surface energy of the neutral, bare electrode) on both sides:

$$S_a(\gamma - \gamma_0) = G(N,q) - G(0,0) - N\mu(A^n) + (Nne - q)\Phi$$

which differentiates into:

$$S_a d\gamma = \left[\frac{\partial G}{\partial N}dN + \frac{\partial G}{\partial q}dq - \mu(A^n)dN + (nedN - dq)\Phi\right] + (Nne - q)d\Phi$$

$$S_a d\gamma = [\mu(A)dN + \Phi_e dq - \mu(A^n)dN + (nedN - dq)\Phi] + (Nne - q)d\Phi$$

The chemical potential of A on the surface, $\mu(A) = \frac{\partial G}{\partial N}$, is defined at *constant surface charge*, and is here supposed to be fixed. Now, assuming that, for any fixed value of ϕ, the system is at electrochemical equilibrium, the differential inside the brackets must be equal to zero,

[1]This reaction notation is meant to be generic and should not mislead the reader into thinking that only ions can get electrosorbed or that no splitting reaction could occur along the way. Different examples of electrosorption are:

$$H^+_{aq} + e^- \rightarrow H^*$$

$$Cl^-_{aq} \rightarrow Cl^* + e^-$$

$$H_2O \rightarrow 2H^+_{aq} + 2e^- + O^*$$

The first and second examples are respectively a reduction and an oxidation with $n = 1$ and $n = -1$. The third example, involving a neutral species, is also an oxidation with $n = -2$.

implying:

$$\boxed{\mu(A) - \mu(A^n) + ne\Phi = 0} \tag{6.1}$$

$$\Phi_e = \Phi \tag{6.2}$$

$$\boxed{d\gamma = -\tilde{\sigma} d\Phi} \tag{6.3}$$

Eq. (6.1) is the traditional Nernst equation. Eq. (6.2) expresses electric equilibrium, and in the remaining, Φ will be used in place of Φ_e. Eq. (6.3) is the so-called electrocapillary equation, in which the total surface charge $\tilde{\sigma}$ is defined:

$$\begin{aligned} \tilde{\sigma} &= -\frac{Nne}{S_a} + \frac{q}{S_a} \\ &= -\theta n \alpha e + \sigma \end{aligned}$$

where in turn are defined:

- θ, the adsorbate coverage on the surface,
- α, the surface atomic density,
- σ, the free surface charge.

Note the important distinction between *free* and *total* surface charges. The former accounts for charge actually present at the surface, also called non-faradaic charge, when the latter also includes charge transfered from the external circuit upon electrosorption, by contrast called faradaic charge[2]. Correspondingly, two capacitances are defined:

$$\frac{1}{c_{\mathrm{dl}}} = \frac{\partial \Phi}{\partial \sigma}$$

$$\frac{1}{c_{\mathrm{ps}}} = \frac{\partial \Phi}{\partial \tilde{\sigma}}$$

c_{dl} being the double-layer capacitance and c_{ps} being the pseudo-capacitance, directly measurable in cyclic voltammetry.

[2]The reason for that denomination is that, assuming constant free surface charge, electrosorption of 1 mole of molecules leads to an amount of charge transfered from the external circuit to the electrode exactly equal to $-nF$, where F is Faraday's constant, that is 96485 C.

In the following, Eqs. (6.1) and (6.3) are applied to the case of hydrogen under-potential deposition in order to calculate deposition curves and surface energies as a function of electrode potential.

6.2 Hydrogen under-potential deposition on electrified Pt surfaces

The adsorption of atomic hydrogen on platinum surfaces starting around 0.5-0.3 V/RHE in a cathodic sweep is called under-potential deposition, in reference to the fact that hydrogen evolution (production of dihydrogen gas from protons in solution) starts only at negative potentials. This pre-reduction on the surface is due to the hydrogen chemical affinity for the metal. Here, the purpose is to quantify this phenomenon taking into account chemical and electrostatic factors in the double layer.

6.2.1 Free energy of adsorption

Following the approach suggested in [139], the electrosorption of the proton ($H^+ + e^- \rightarrow H^*$) is decomposed into the two-step process:

$$H^+_{aq} + e^- \rightarrow \frac{1}{2}H_2(g)$$

$$\frac{1}{2}H_2(g) \rightarrow H^* \tag{6.4}$$

By definition, the first reaction is at equilibrium when the working electrode is at the potential of the reversible hydrogen electrode (Φ_{RHE}). Therefore, for a potential U with respect to RHE, the overall free energy change upon electrosorption of one proton is:

$$\Delta G_{tot} = eU + \Delta G(\theta) + kT \ln \frac{\theta}{1-\theta} \tag{6.5}$$

where $\Delta G(\theta)$ is the free energy of reaction (6.4) (it is a function of coverage) and the last term accounts for the change in configurational entropy on the surface. In turn, ΔG is computed as:

$$\Delta G = \Delta E_{el} + \Delta ZPE + Ts$$

with Ts being the entropic free energy of $\frac{1}{2}H_2$ in the gas phase, that is 0.20 eV at room temperature and atmospheric pressure [66].

Variations in electronic energy and zero-point energy are calculated with the use of ab-initio package Quantum-ESPRESSO [137]. The metal surface is represented by a 4-layer slab in the (111) or (100) direction with a lattice parameter of 4.0 Å. Adsorption energies are computed within a $(2 \times \sqrt{3})$ unit cell with H being placed at the preferential site, i.e. the fcc site on (111) and the bridge site on (100). Relaxation of the topmost metal layer is allowed. The PBE density functional is used in combination with ultrasoft pseudopotentials for ionic cores. The plane-wave cutoff is 30 Ry, and a $7\times7\times1$ k-point mesh is used for Brillouin zone sampling.

The electrode potential is monitored by adding explicit charge on the slab. A correction scheme, as exposed in [102], is applied to obtain the exact potential profile of the isolated slab in the unit cell. The electrochemical double layer is modeled by placing a planar counter-charge at a distance of 3 Å from the metal surface. The dipolar response of water is rendered by inserting a continuum dielectric medium inside the double layer. Cyclic voltammetry and impedance spectroscopy measurements at 1 KHz in 0.1-1 M electrolytes have yielded a double layer capacitance c_{dl} in the range 20-100 $\mu F/cm^2$ [140]. Here, a representative value of 40 $\mu F/cm^2$ is chosen, which, for that geometry, implies a relative permittivity of 13.6. The absolute electrode potential Φ is computed as $-v(\infty) - \varepsilon_F$, where $v(\infty)$ is the value of the electrostatic potential in the flat region outside the double layer, and ε_F is the Fermi energy. Since this model ignores the chemical effects of water, and in particular its contribution to the surface dipole, an estimate of the charge needed by default on the uncovered surface is derived from experimental measures of the potential of zero charge (PZC). Using the CO-charge displacement method, A. Cuesta estimated $\Phi_{PZC} \simeq 0.23$ V/SHE [141], while the impedance spectroscopy measurements of T. Pajkossy and D.M. Kolb suggest $\Phi_{PZC} \simeq 0.34$ V/SHE [140]. This is also consistent with an estimate found by Otani et al. using molecular dynamics [142] (interestingly, Otani et al. also find a relative dielectric constant of the water slab between 15 and 25). Incidentally, those values happen to be very close to the onset of hydrogen adsorption in acidic medium. Therefore, in this study, the metal surface at 0.3 V/RHE in acidic medium (pH = 0) is treated as neutral. However, when the pH is brought to alkaline values, the absolute potential of the reversible hydrogen electrode is modified. Thus, at room temperature:

$$\Phi_{RHE} = \Phi_{SHE} - 0.059 \times pH$$

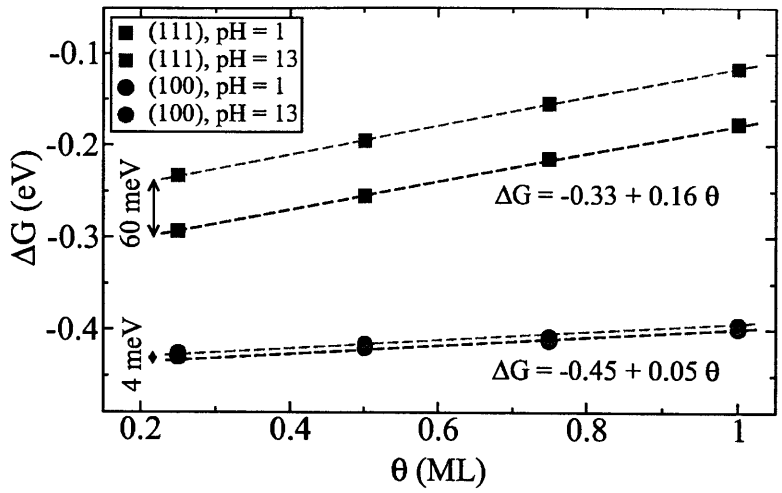

Figure 6-1: Free energy of $\frac{1}{2}H_2(g) \rightarrow H^*$ reaction on Pt(111) and Pt(100) for pH = 1 and pH = 13, along with linear fits. The configurational entropy on the surface is not included.

Consequently, the metal surface with the same relative potential of 0.3 V/RHE now bears a non-zero charge density:

$$\sigma = -0.059 \times c_{dl} \times \text{pH} \tag{6.6}$$

Using this electrochemical model, ΔG is calculated in acidic (pH = 1) and alkaline (pH = 13) conditions (Fig. 6-1). Interestingly, changing the pH has almost no effect on adsorption energies on (100), while a sizeable effect is observed on (111).

6.2.2 Surface dipole

To understand the difference, the electrode absolute potential is plotted as a function of hydrogen coverage (Fig. 6-2). The resulting line for (100) has almost zero slope, suggesting that hydrogen atoms adsorbed on that surface induce only a small change in the surface dipole. By contrast, adsorption of one monolayer of hydrogen on the (111) surface lowers the potential by about 0.5 V, a result that is consistent with the relative electropositivity of hydrogen. The link between adsorption energy and surface dipole can be formalized by deriving the adsorbate chemical potential μ_H from an expression of the surface free energy. Considering a surface with N hydrogen adsorbates and q free charges, its free energy is:

$$G(N,q) = G(N,0) + \int_0^q \frac{\partial G}{\partial q'} dq'$$

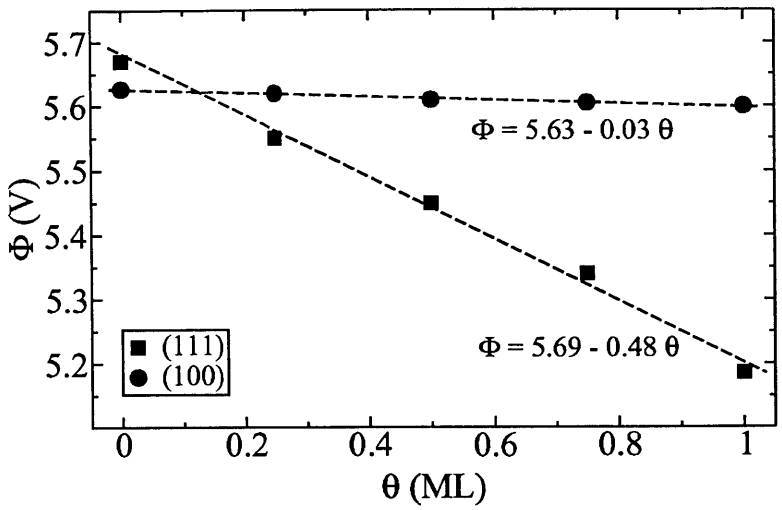

Figure 6-2: Electrode absolute potential vs. hydrogen surface coverage, along with linear fits.

$$G(N,q) = G(N,0) + \int_0^q \Phi(N)dq'$$

Taking the derivative with respect to N to get the chemical potential:

$$\mu_H = \frac{\partial G}{\partial N}(N,0) + \int_0^q \frac{\partial \Phi}{\partial N}(N)dq'$$

or, rewriting in terms of the coverage θ and the surface charge density σ:

$$\mu_H = \mu_{H,zc} + \frac{1}{\alpha}\int_0^\sigma \frac{\partial \Phi}{\partial \theta}(\theta)d\sigma'$$

where α denotes the surface atomic density, and $\mu_{H,zc}$ is the chemical potential on the neutral surface. Φ varies linearly with θ, leading to the compact expression:

$$\mu_H = \mu_{H,zc} + \frac{\sigma\Delta\chi}{\alpha}$$

where $\Delta\chi$ is the surface dipole change for a full monolayer of hydrogen (-0.03 on (100), -0.48 on (111)). Using Eq. (6.6) for the expression of σ, the chemical potential change upon variation of the pH is given by:

$$\Delta\mu_H = -0.059 \times \frac{c_{dl}\Delta\mathrm{pH}\Delta\chi}{\alpha}$$

Table 6.1: Atomic densities for unreconstructed Pt surfaces (cm^{-2}).

(111)	1.44×10^{15}
(100)	1.26×10^{15}
(110)	0.89×10^{15}

This result confirms that the pH dependence of the adsorption energy is directly proportional to the surface dipole induced by adsorbates.

6.2.3 Electrosorption valency

The previous effect can be related to the concept of electrosorption valency [143]. Here specifically, the electrosorption valency λ of the proton is the number of electrons transfered to the electrode from the external circuit upon adsorption of one proton at constant potential. This is equal to 1 plus a corrective quantity to compensate for the induced change in the surface potential. Adsorption of one proton on a unit surface area perturbs the potential by $\delta\Phi = \frac{\Delta\chi}{\alpha}$, which is compensated by adding $\eta = \frac{c_{dl}\Delta\chi}{\alpha e}$ electrons to the surface. Consequently, for the particular value of the capacitance:

$$\lambda_{111} = 1 + \eta = 0.91$$

$$\lambda_{100} = 0.98$$

where differences in surface atomic densities have been accounted for (Table 6.1). Extending the analysis of the surface energy in the case where $\mu(A)$ is allowed to change, one can relate faradaic and non-faradaic charge transfers when the pH is modified. Building on previous derivations by Frumkin et al., Garcia-Araez et al. showed [144]:

$$\frac{c_{\mathrm{dl}}}{c_{\mathrm{ps}}} = 1 - e\left(\frac{\partial\Phi}{\partial\mu_{\mathrm{H^+}}}\right)_{\tilde{\sigma}}$$

Using this relation, they determined the potential as a function of pH for fixed total charges, and inferred the double layer capacitance, offering an interesting alternative to impedance spectroscopic methods.

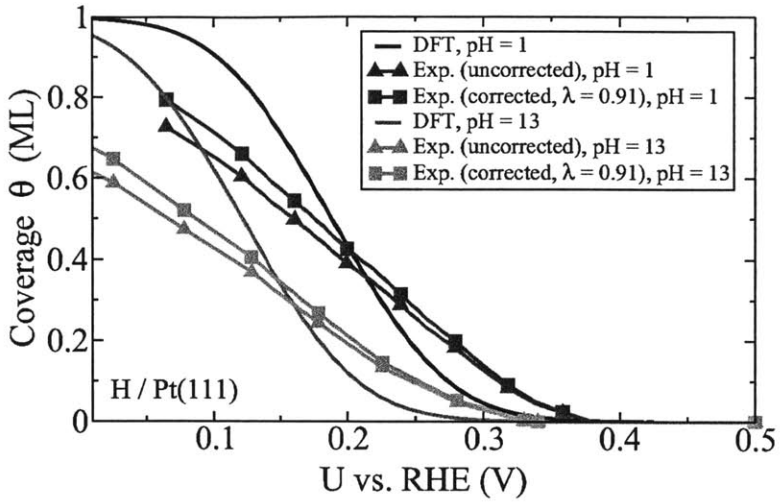

Figure 6-3: Hydrogen deposition on Pt(111) in the low potential region for acidic and alkaline conditions. Experimental adsorption curves are corrected taking into account the non-integer electrosorption valency. Experimental data are from [145, 146, 147].

6.2.4 Deposition curves

Within the under-potential deposition region (U = 0-0.5 V/RHE), the hydrogen surface coverage at equilibrium is obtained by setting $\Delta G_{tot} = 0$ in Eq. (6.5) (Figs. 6-3 and 6-4). On (111), experimental coverages obtained from integration of voltammetric currents are included for comparison. Initial integration assumed that 1 e^- is exchanged per hydrogen adsorption. A corrected curve is proposed with the value of the electrosorption valency including the assumption on the capacitance. Although noticeable, the correction is small. On (100), integration of the voltammetric current in alkaline conditions is difficult as it overlaps with the current from OH formation. Therefore, the peak current is used as a more reliable reference point. In all cases, DFT results are found in very satisfying agreement with reported measures, in spite of a certain underestimation of H-H lateral interactions on (111). Of interest is to note the shift of the (111) curve towards lower potentials for higher pH, a direct consequence of the electrosorption valency effect discussed earlier.

6.3 Nanoparticle equilibrium shape

The potential dependence of the surface energy is expressed by the electrocapillary equation [148]:

$$d\gamma = \theta\lambda\alpha e dU$$

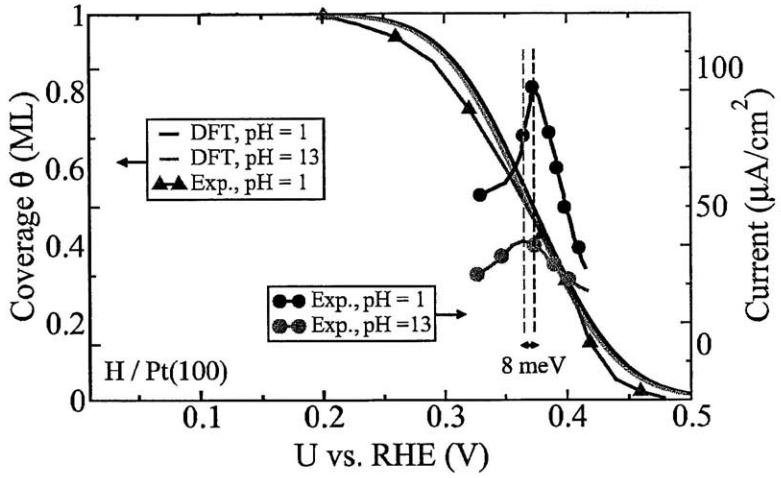

Figure 6-4: Hydrogen deposition on Pt(100) in the low potential region for acidic and alkaline conditions. Peak voltammetric currents are displayed for comparison as integration of the current in KOH electrolyte is hindered by overlap with OH discharge current. Experimental data are from [145, 146, 147].

In other words, the surface energy can be directly obtained by integrating the $\theta(U)$ curve from high to low potentials (Fig. 6-6). The starting point, i.e. the surface energy of the bare facet, is taken from [149], where they show that $\gamma_{111} = 1.49$ J/m^2 and $\gamma_{100} = 1.81$ J/m^2. Now, in a simple model where a Pt nanoparticle would only consist of (111) and (100) facets, the energy-minimizing shape can be found by applying the Wulff construction [150][3]. In this case, a degree of "cubicity" κ can be defined as the ratio of (100) facets over the total nanoparticle surface area, and must depend[4] only on the surface energy ratio $\frac{\gamma_{111}}{\gamma_{100}}$ (Fig. 6-5). As the

[3]This is based on the assumption that the nanoparticle is large enough so that surface energies are not affected by size effects. For very small nanoparticles, see for instance [151]. They show that above 1.5 nm i.e. 140 atoms, the truncated octahedron is the most stable shape. Smaller than that, the tetrahexahedron is more stable.

[4]We have calculated explicitly κ as a function of $\frac{\gamma_{111}}{\gamma_{100}}$:

$$\frac{\gamma_{111}}{\gamma_{100}} < \frac{1}{\sqrt{3}} \Rightarrow \kappa = 0$$

$$\frac{1}{\sqrt{3}} \leq \frac{\gamma_{111}}{\gamma_{100}} < \frac{2}{\sqrt{3}} \Rightarrow \kappa = \frac{1}{1+\sqrt{3}\left(\frac{(\frac{\gamma_{111}}{\gamma_{100}})^2}{\left(\frac{\gamma_{111}}{\gamma_{100}}\sqrt{3}-1\right)^2}-1\right)}$$

$$\frac{2}{\sqrt{3}} \leq \frac{\gamma_{111}}{\gamma_{100}} < \sqrt{3} \Rightarrow \kappa = 1 - \frac{1}{1+\left(\frac{2\sqrt{3}}{\left(3-\frac{\gamma_{111}}{\gamma_{100}}\sqrt{3}\right)^2}-\sqrt{3}\right)}$$

$$\frac{\gamma_{111}}{\gamma_{100}} \geq \sqrt{3} \Rightarrow \kappa = 1$$

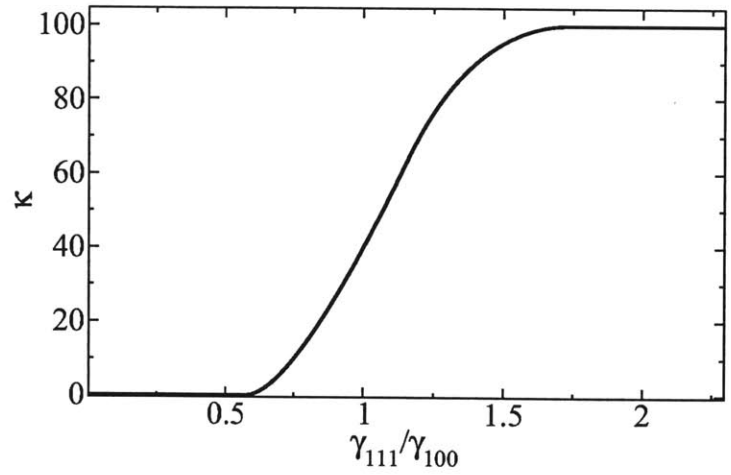

Figure 6-5: Particle cubicity vs. $\gamma_{111}/\gamma_{100}$.

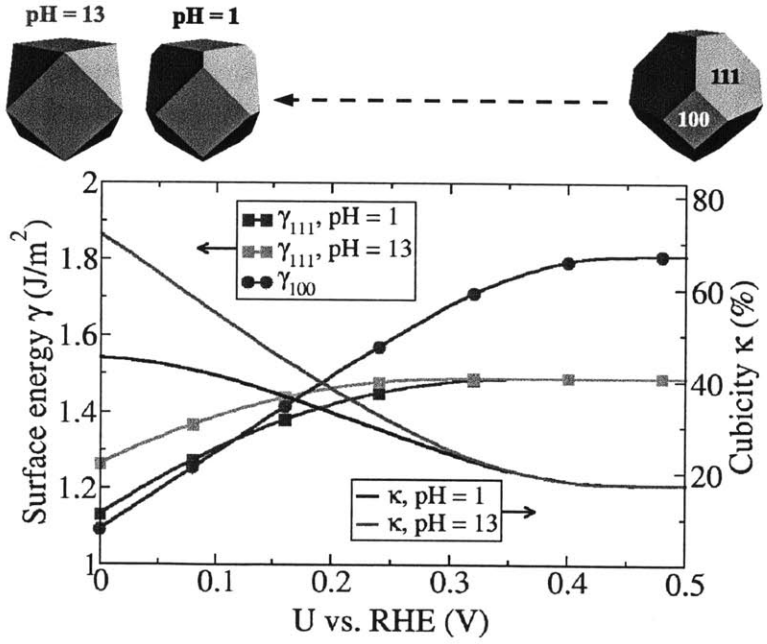

Figure 6-6: (111) and (100) surface energies as obtained from application of the electrocapillary equation to the hydrogen deposition curves for different pHs. Subsequent change in the nanoparticle cubicity.

electrode potential is scanned to lower potentials, hydrogen deposition occurs earlier on (100) due to a higher reactivity, leading to greater stabilization of the surface compared to (111). As a consequence, the equilibrium nanoparticle shape becomes more cubic. In alkaline conditions, this effect is reinforced by the reduced affinity of the (111) surface. This approach provides a route for quantification of a phenomenon already observed experimentally: P. J. Ferreira and Y. Shao-Horn have shown that hydrogen permeating from the anode to the cathode of a proton exchange membrane fuel cell can reduce Pt ions present in solution and produce nanoparticles having a more pronounced cubic aspect as the hydrogen concentration is larger [152].

6.4 Conclusion

In summary, a model for the electrochemical double layer has been developed in which the electrode bias is realistically monitored through placing explicit charge on the surface. Applied to the prediction of hydrogen electrodeposition on Pt surfaces, it has led to the first determination of electrosorption valencies from first-principles and illuminated how the pH can indirectly affect adsorbate energies through the surface charge of the RHE. Finally, derivation of surface energies has illustrated how first-principles approaches combined with experimental insight have now increasing power to relate significant factors of catalytic activity, namely electric bias, adsorbate coverage, surface stability and catalyst geometry. It should be kept in mind however that observed nanoparticle shapes are not necessarily the most stable ones thermodynamically, as kinetic and hysteretic effects may be dominant (e.g. see nanoparticle shape monitoring by periodic potential treatment [153]).

Chapter 7

Water Permittivity Saturation Effects in Double Layer Electric Fields

7.1 Structure of water on transition metal surfaces

Water is an important component in systems that have been studied so far. Besides participating directly in some reactions, it plays an essential role as being the solvent. Assessment of its contributions to chemical, diffusive, electrostatic processes is required for a better understanding of the double layer properties. More generally, a large number of physical systems involve water at an interface. Knowledge of its wetting properties on metals, oxides and other compounds can lead to the right choice of boundary conditions in flow problems. In the past decades, special efforts have been devoted to studying the structure of water on transition metal surfaces. The reason is the availability of well-characterized single-crystal surfaces which facilitate comparison with models. In addition, numerous surface science techniques need electronic conductivity of the surface. In spite of this amount of work, water on surfaces remains the subject of uncertainties and is open to further investigations. Experimentally, the arrangement of protons in water structures is still a challenge to the resolution of spectroscopic techniques. On the computational side, water lies at the limit of ab-initio capabilities in several regards: different proton arrangements are often very close in energy, and an accuracy of the order of 10 meV per bond would be desirable; the quantum behavior of the proton plays a significant role, calling for methods going beyond the Born-Oppenheimer approximation [154]; water-water interactions are partially non-local through van der Waals and hydrogen bonds; the configurational space is very large because of proton disorder, with statistics not necessarily accessible by molecular-dynamics tools; interactions with metal surfaces are to be considered with caution owing to ab-initio own uncertainties on those systems. However, progress has certainly been made, and this section aims at summarizing the main findings on the structure

of water on transition metal surfaces, and particularly on platinum [155].

7.1.1 Single molecule adsorption

The simplest problem is adsorption of a single water molecule on the metal surface. Performing DFT calculations, Michaelides et al. showed that an isolated water molecule adsorbed on a closed-packed metal surface lies preferentially on the atop site, parallel to the surface so as to interact with its $1b_1$ orbital [156]. Binding energies are relatively weak, most of them on the order of 30-50 kJ/mol.

7.1.2 Monolayer adsorption

UPS and XPS spectroscopies applied to the study of a water monolayer adsorbed on platinum have produced features supporting molecular adsorption, which is to say that water does not dissociate on the surface [157]. A first set of LEED studies were then conducted, and it was suggested that above 125 K, the water layer adopts a $(\sqrt{3} \times \sqrt{3})R30°$ arrangement [158, 159]. Remarkably, the naturally occurring ice crystal is also hexagonal, with a lattice constant close to $\sqrt{3}$ times the inter-atomic distance of group VIII metals. It was therefore tempting to conclude that water can grow epitaxially on the surface in the form of ice, satisfying both metal-water and water-water affinities.

This framework was further explored in the work of Ogasawara et al. [160]. After performing a combination of XAS, XPS and XES measurements, they looked for the geometric arrangement that was most consistent with experimental lineshapes (O core level shift). Uncoordinated OH bonds can be detected through their effect on the O near edge x-ray adsorption fine structure (NEXAFS), which is used to selectively probe the local unoccupied orbital structure in different orientations in the layer. Comparing the calculated O K-edge spectra for different structural models with experiment provides information about the orientation of water in the film, particularly the presence of uncoordinated OH groups that are pointing into the vacuum. To guide the search, DFT calculations for a commensurate $(\sqrt{3} \times \sqrt{3})R30°$ water bilayer were completed, with two possible configurations: one where alternate protons in the top layer were pointed upward, away from the surface, the other where they were pointed down, toward the surface. Given that uncoordinated OH bonds should be characterized by XAS features in the low energy part of the spectrum (around 535 eV), and that no such features were found experimentally, they suggested that only the H-down configuration is the preferred one. Furthermore, the best spectral fit was obtained for a water layer thickness of 0.25 Å, in contrast with 0.96 Å for the bilayer in bulk ice, and these findings were also supported by energy results from DFT. In short, they concluded that the water overlayer is almost flat on the surface and that

all molecules participate in the binding. Later, IR spectroscopy measurements added more evidence to the fact that water molecules adsorb in the H-down configuration, since no high frequency feature near 3770 cm^{-1}, that would correspond to OH dangling bonds, was measured.

Nonetheless, later studies showed that water arrangement on the surface was richer than initially expected. He scattering and new LEED experiments, with improved non-invasiveness[1], revealed a long range registry between water and Pt(111), with appearance of a $(\sqrt{39} \times \sqrt{39})R16°$ structure upon completion of a full monolayer [165], inducing a 3% compression relative to bulk ice. With DFT calculations, Feibelman found that the $(\sqrt{39} \times \sqrt{39})R16°$ structure is 0.07 eV more stable than the simple $(\sqrt{3} \times \sqrt{3})R30°$ structure, and reported that even partial dissociation occurs. This more complex arrangement is also consistent with substantial broadness of IR spectral lines. Given that the OH stretching frequency depends on the strength of the hydrogen bond and is therefore strongly correlated to the O-O separation, only systems where water has a limited number of adsorption geometries can display sharp stretching bands [157].

Note however that the bilayer model turns out to be correct on some surfaces, e.g. the SnPt(111) surface [166].

7.1.3 Multilayer adsorption and wetting

Kimmel et al. studied the wetting properties of water on Pt(111) using TPD techniques in combination with rare gas physisorption [165]. They found that the first adsorbed layer wets at all temperatures (20-150K) and confirmed the formation of a commensurate $(\sqrt{39} \times \sqrt{39})R16°$ structure. When a second layer is adsorbed, wetting prevails below 120K for kinetic reasons, whereas above 135K, non-wetting crystalline ice is formed, with an incommensurate $R30°$ relaxed structure. This observation is in line with predictions on the hydrophobic nature of the first layer based on the absence of OH dangling bonds. In addition, it clarifies other measurements:

[1] In a similar way, early conclusions from the work of Held and Menzel for water on ruthenium had to be revisited when it was realized that LEED measurements can perturb the system. Studying water adsorption on Ru at low temperature (below 150 K), they found that oxygen atoms are arranged in a coplanar way, supporting the idea of partial dissociation [161]. This conclusion was consistent with calculations by Feibelman et al. and Michaelides et al. [162, 163, 164], showing that half-dissociation stabilizes the system by at least 0.2 eV per molecule.

However, a subsequent study was conducted by Hodgson, who used IR spectroscopy and showed that, below 150 K, there is no dissociation and that the bilayer arrangement prevails in a metastable state. Dissociation occurs only at higher temperature, right before evaporation starts, at 160 K. In other words, the electron beam in the Held-Menzel experiment was producing a partial artefact. Formed OH was pinning the water layer into a $\sqrt{3} \times \sqrt{3}$ structure.

- In He scattering experiments, no intensity oscillations are observed during the growth of crystal ice films on Pt(111), suggesting that the growth does not proceed in a layer-by-layer fashion.
- Crystal ice films grown on Pt(111) are found to have an abundance of dangling OH bonds with nearly isotropic distribution. This can be attributed to the different facets of 3D ice crystallites.
- The $(\sqrt{39} \times \sqrt{39})R16°$ structure is consistently observed by LEED up to a 5 ML adsorption. The reason is that even at those high coverages, less than 50% of the surface is covered with 3D ice crystallites.
- Incidentally then, observation of zero-order water desorption kinetics cannot be invoked to support multilayer water wetting.

Studies on other metals, Cu, Ag, Au, also concluded that multi-layer water does not wet, forming 3-D ice clusters on the surface.

Carrasco et al. applied the vdW-DF functional to water adsorption on Cu and Ru in an attempt to solve the long-standing problem that semi-local functionals predict bulk ice to be always more stable than metal-water structures, in contradiction with the observation of the wetting adlayer [167]. They showed that inclusion of non-local correlation does stabilize water over the metal surface, owing to the greater polarizability of metal atoms compared to oxygen and hydrogen. C_6 coefficients from time-dependent DFT calculations of Ru, Cu, O and H are 79, 44, 2 and 1 respectively (in a.u.) [168].

The work of Noguchi et al. illustrates the power of sum frequency generation (SFG) spectroscopy for surface investigation [169]. On Pt, they observed two broad peaks in the OH stretching region at ca. 3200 cm^{-1} and ca. 3400 cm^{-1}, which are know to be the symmetric OH stretching of tetrahedrally coordinated, i.e. strongly hydrogen bonded "ice-like" water, and the asymmetric OH stretching of water molecules in a more random arrangement, i.e. weakly hydrogen bonded "liquid-like" water, respectively. On Au, domination of the 3400 cm^{-1} band indicates that water on Au is less ordered than on Pt.

7.1.4 Water modeling

Early simulations of the platinum-water system were done using classical potentials, usually the TIP4P potential for water-water interactions and some empirical potential for platinum-water interactions [170, 171]. Computed quantities included the water structure at the interface,

the dipole change induced by water, and effects of an electric field from the metal electrode. With the increase of computational power, ab-initio studies were then undertaken. Simulation of pure water is a notably difficult problem in itself. DFT tends to overcorrelate water, predicting a melting temperature as high as 400 K [172]. Factoring in nuclear quantum effects has been shown to substantially improve the correlation function. This can be done by using path-integral techniques [154]; freezing the water intramolecular degrees of freedom has also turned out successful [172, 173]. Interestingly, path-integral techniques were also used to assess the effect of water quantization in a model for electron transfer at the platinum-water interface, and they were shown to have a possibly substantial impact on tranfer kinetics [72]. Insights into the electronic structure between platinum and water were provided by Vassilev et al. They showed that electron bands around the Fermi level of the metal extend over the water adlayer, so that the surface as a whole maintains full metal conductivity, an observation of great importance in the context of electron transfer through the surface [68].

Summary - The structure of water on transition metal surfaces is a complex balance between surface bonding and hydrogen bond optimization. The picture of hexagonal ice epitaxial growth is too simple to capture structure variablity, but offers an interesting starting point to understand competing trends. Along the same line, it suggests that insight into the electrostatic structure of the double layer can be gained by first addressing the question of ice Ih permittivity.

7.2 Permittivity of ice

7.2.1 Literature review

7.2.1.1 Analytical approaches

Different phases of ice exist, the naturally occurring one being hexagonal ice Ih. In any phase, energy minimization imposes rules on the direction of hydrogen bonds, called *ice rules* (see further for more detail). In spite of those constraints, a very large number of proton configurations are allowed, and several properties are determined by this *proton disorder*. One, of course, is the entropy of ice, and consequent phase transitions. Another is the permittivity, which is determined by the statistics of dipole orientation. Using probability arguments, Pauling calculated a residual entropy for ice of $k\ln\frac{3}{2}$, in good agreement with the experimental value [174]. An exact solution for the problem of the entropy of ice was found in two dimensions [175], while series expansion methods must be used when going to three dimensions [176].

7.2.1.2 Monte Carlo simulations

Analytical or semi-analytical techniques are quickly limited when refinements are introduced, like energy differences between configurations. Given the size of the configurational space, a method of choice has therefore been the Monte Carlo technique. Barkema and Boer developed a statistical model of ice in which a point charge model of H_2O was used [177]. Rick and Haymet studied ice Ih using classical force fields (including two flavors of TIP4P, one non-polarizable, the other polarizable) to obtain energies and polarizations [178]. They devised an ergodic move algorithm to sample proton configurations. Performing Metropolis runs, they obtained the permittivity of ice, and showed the improvement brought by polarizable models. Later, Knight et al. and Kuo used DFT to calculate the energy of different proton configurations in ice VII and ice Ih in small unit cells [179, 180]. Then, combining cluster expansion techniques and the concept of graph invariant, they were able to extract a discrete hamiltonian with 3 invariants (or 7 for ice VII), which could be used to predict energies in larger cells. Then, Monte Carlo simulations using the Rick-Haymet algorithms allowed them to predict proton-ordering phase transitions at low temperatures, around 100 K for the ice Ih/XI phase transition.

7.2.1.3 Molecular dynamics

Sharma et al. did an ab-initio molecular dynamics study of liquid water in which the molecular dipole was determined from the charge density distribution of the Wannier functions [181]. They obtained a good estimate of the permittivity and emphasized the importance of both dipole correlations and the large water molecule dipole in condensed phase.

Summary - Different works in the literature show that a common issue in finding the permittivity of ice is to have access to the right molecular dipole. Classical models provide a direct answer, but are naturally prone to uncertainties and may need ad-hoc additions, such as polarizability. Ab-initio approaches, on the other hand, often run into the well-known problem of defining polarization under periodic boundary conditions, unless transformations are made such as wannierization. In the next section, we propose a statistical approach using ab-initio calculations, in which, nonetheless, the polarization is determined from a charge density distribution in real space. In addition, we address the issue of dielectric saturation of water when subject to strong fields.

7.2.2 General theory of permittivity for a polar and polarizable medium

The electric permittivity of a medium measures its ability to respond to an electric field by creating a macroscopic polarization. Virtually all materials are polarizable through the response

of their electrons. In a polar material, an additional polarization may appear from alignment of pre-existing individual dipoles. This is the case for water, whose molecule is well known to possess a dipole moment. As a starting point for studying permittivity, let us fix some notations and write the formalism by which microscopic dipoles and macroscopic fields are related:

$\vec{E}$ = electric field
$\vec{D}$ = displacement field
$\vec{\mu}_g$ = individual dipole of a given molecule in the gas phase
$\vec{m}$ = individual dipole of a given molecule in the condensed phase
$\vec{M}$ = total dipole moment ($\mathrm{C}\cdot\mathrm{m}$) in a piece of material of volume Ω
$\vec{P}$ = polarization ($\mathrm{C/m^2}$)

These definitions imply:

$$\vec{M} = \sum_{\text{molecules}} \vec{m} = N\langle\vec{m}\rangle$$

$$\vec{P} = \vec{M}/\Omega = n\langle\vec{m}\rangle$$

where N is the number of molecules in volume Ω and n is the density. In general, the dipole moment on a molecule in the condensed phase differs from the one in the gas phase. The additional polarization originates on one hand from the new specific chemical environment and on the other hand from the molecule response to two external fields, identified in Onsager's original theory [182] (see also [183] for extensive derivation and discussion): the reaction field, $\vec{R}$, is the field created by all other molecules in response to the molecule own dipolar field, and is therefore proportional to $\vec{m}$, $\vec{R} = \beta_1\vec{m}$; the cavitation field, $\vec{G}$, is the external field that acts on the molecule as a result of application of an external field to the material, and is therefore proportional to $\vec{E}$, $\vec{G} = \beta_2\vec{E}$. The molecule responds to each of those fields with its polarizability α, from which it results:

$$\begin{aligned}\vec{m} &= \vec{\mu}_g + \vec{\delta\mu}_c + \vec{\delta\mu}_1 + \vec{\delta\mu}_2 \\ &= \vec{\mu}_c + \alpha\beta_1\vec{m} + \alpha\beta_2\vec{E}\end{aligned}$$

where $\vec{\mu}_c = \vec{\mu}_g + \vec{\delta\mu}_c$, $\vec{\delta\mu}_c$ being the additional polarization upon condensation. Factorizing in $\vec{m}$ and reordering:

$$\begin{aligned}\vec{m} &= \frac{\vec{\mu}_c}{1-\alpha\beta_1} + \frac{\alpha\beta_2}{1-\alpha\beta_1}\vec{E} \\ &= \vec{\mu} + \frac{\chi_{\text{opt}}}{n}\vec{E}\end{aligned} \tag{7.1}$$

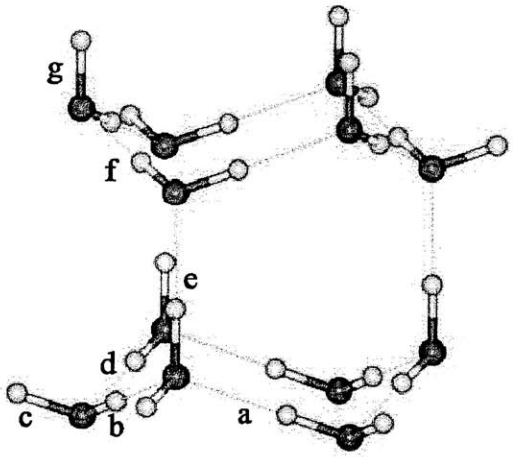

Figure 7-1: Water molecule arrangement in ice Ih.

In the case of water, the effective dipole $\vec{\mu}$ includes the original dipole in the gas phase, the effect of hydrogen bonding and van der Waals interactions, and polarization from the reaction field. Turning now to the fundamental equation of electrostatics in dielectric media:

$$\begin{aligned} \vec{E} &= \vec{D} - 4\pi\vec{P} \\ &= \vec{D} - 4\pi\left(n\langle\vec{\mu}\rangle + \chi_{\text{opt}}\vec{E}\right) \end{aligned} \tag{7.2}$$

and introducing the optical permittivity $\varepsilon_{\text{opt}} = 1 + 4\pi\chi_{\text{opt}}$:

$$\varepsilon_{\text{opt}}\vec{E} = \vec{D} - 4\pi n\langle\vec{\mu}\rangle \tag{7.3}$$

7.2.3 Effective molecular dipole $\vec{\mu}$

In his theory, Onsager derives the permittivity of a polar and polarizable medium using the "intrinsic" dipole in the condensed phase $\vec{\mu}_c$. However, in a computational setup, where the molecule is embedded in a medium, one will only be able to access the effective dipole $\vec{\mu}$. If the computational scheme uses periodic boundary conditions, one runs into the notorious problem that the dipole moment cannot be uniquely determined from the real-space charge density. One way to go around that issue is, following the example of Sharma et al., to resort to the Wannier function formalism [184, 185], from which a charge density specific to each molecule can be extracted. Alternatively, it is also possible to perform a Berry phase calculation [186]. Here, we propose another solution, where $\vec{\mu}$ is determined from the real-space charge density

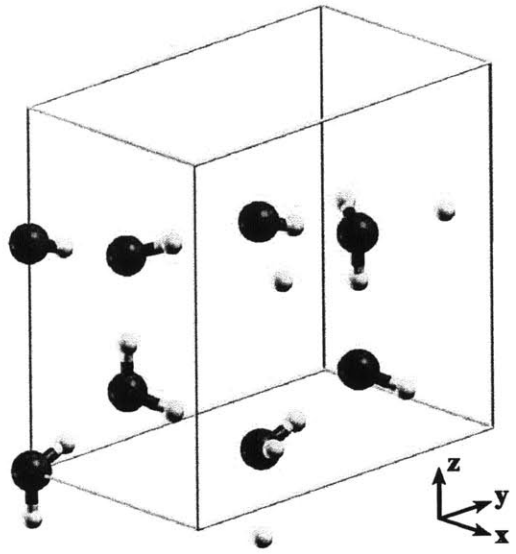

Figure 7-2: Orthorhombic unit cell.

distribution of a piece of ice with one finite dimension.

7.2.3.1 Simulation supercell

As mentioned earlier, ice Ih has the structure of a stack of layers each with hexagonal arrangement (Fig 7-1). Vertical positions within a layer are distorted so that each water molecule is located at the center of a tetrahedron in which it is connected to four other molecules through hydrogen bonds, two "outgoing" bonds corresponding to hydrogen atoms belonging to the molecule, and two "incoming bonds" corresponding to hydrogen atoms belonging to other molecules. These *ice rules* impose an important constraint on the position of oxygen atoms, while being compatible with a lot of configurations for the position of protons. This "proton disorder" is what gives ice an important part of its properties. Here, we define an orthorhombic unit cell containing two layers in the z-direction, with four molecules in each layer, implying a total of eight molecules (Fig. 7-2). Using synchrotron radiation, Röttger et al. measured the lattice parameters of ice and established that the tetrahedron surrounding an oxygen atom is perfect [187]. At 265 K, they found for the hexagonal lattice parameters: $a = 4.52$ Å, $c = 7.36$ Å. Using GGA-DFT (PBE functional), we determined the value of a minimizing the energy with the ratio c/a fixed and found $a = 4.37$ Å vs. 4.50 Å experimentally at 0 K, implying a 3% error. In the following, DFT calculations at the water melting temperature are done with the experimental lattice parameter, translating into:

$$\Omega_{\text{unit cell}} = 1762 \text{ bohr}^3$$

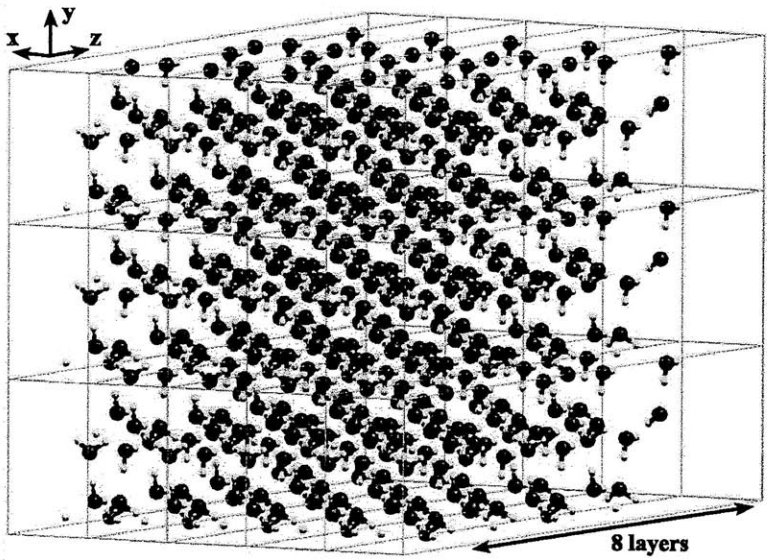

Figure 7-3: Ice slab.

$n = 3.07 \times 10^{28}\ \mathrm{m}^{-3} \Leftrightarrow 0.917\ \mathrm{kg/L}$

By placing four unit cells on top of each other and leaving some free space below and above, we obtain a supercell describing a slab of ice with a thickness of 26.5 Å and of infinite dimension in the x,y plane. Fig. 7-3 gives a representation of the supercell repeated 5 times along x and 3 times along y.

7.2.3.2 Maximum polarization

Maximum absolute polarization with respect to proton arrangement is achieved when all vertical hydrogen bonds in the supercell are placed, for instance, in the downward position. Furthermore, associating a dipole $\vec{m}$ to every molecule and summing all their projections on the z-axis, the assumption of perfect tetrahedron gives for the polarization P along z:

$$P = -0.579 \times n \times m \tag{7.4}$$

m being the norm of $\vec{m}$.

7.2.3.3 Displacement field

At this point, the electrostatic correction scheme implemented in Quantum-ESPRESSO is applied to the supercell, so that the potential profile across the cell is consistent with the charge

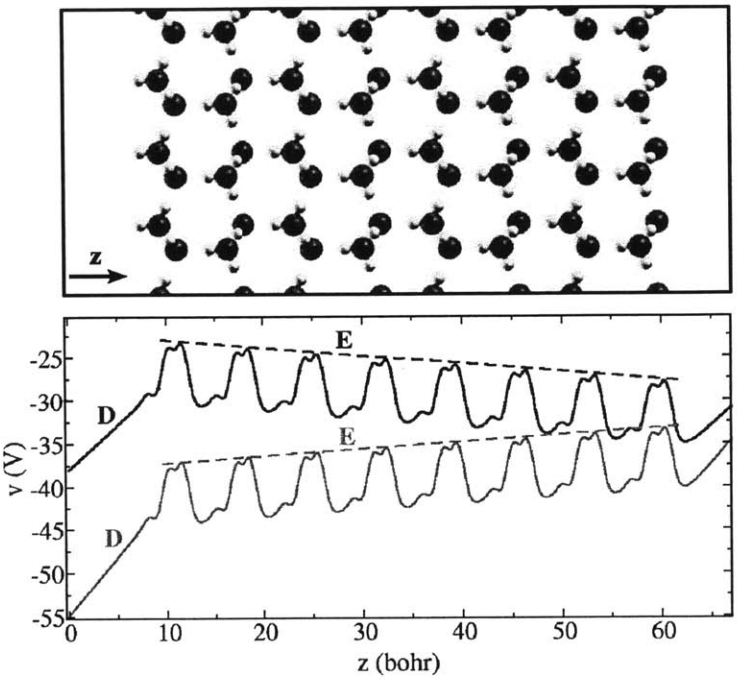

Figure 7-4: Longitudinal potential profile in the ice slab.

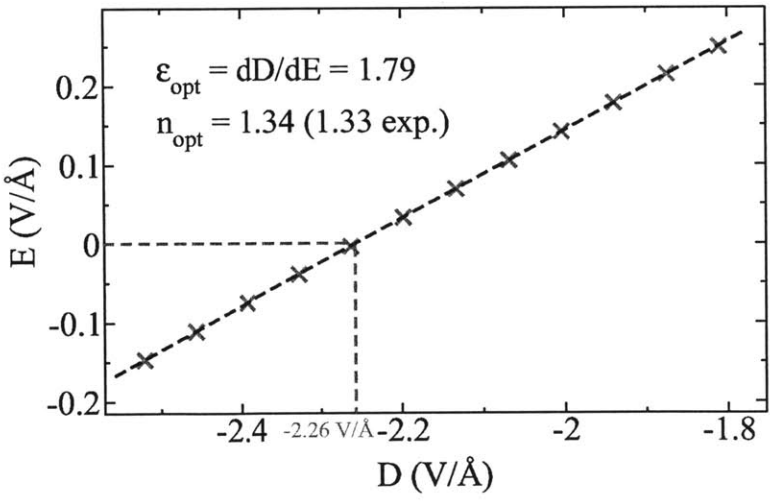

Figure 7-5: Electric field vs. displacement field in ice. Polarization is found at the point where $E = 0$.

density distribution. Simultaneously, an external displacement field, $\vec{D}$, is applied to the slab in the z-direction. The total electric field $\vec{E}$ inside the slab is found by taking the slope of the line tangent to the potential profile (Fig. 7-4). The resulting dependence $E(D)$ is plotted in Fig. 7-5. From Eqs. (7.1) and (7.2), it results, respectively:

$$E = 0 \Rightarrow m = \mu$$

$$E = 0 \Rightarrow D = 4\pi P$$

which, combined with Eq. (7.4), imply:

$$D_{E=0} = 4\pi P = -4\pi \times 0.579 \times n \times \mu \tag{7.5}$$

Therefore, by taking in Fig. 7-5 the displacement field (in Ha/bohr) for which the electric field in ice is zero, we find the corresponding polarization:

$$\begin{aligned} -P &= 0.00349 \text{ e/bohr}^2 \\ &= 0.0125 \text{ e/Å}^2 \\ &= 0.200 \text{ C/m}^2 \end{aligned}$$

and using Eq. (7.5) with the right density of ice Ih, we deduce the effective dipole moment:

$$\begin{aligned} \mu &= 1.33 \text{ e}\cdot\text{bohr} \\ &= 0.70 \text{ eÅ} \\ &= 3.39 \text{ D} \\ &= 11.30 \times 10^{-30} \text{ Cm} \end{aligned} \tag{7.6}$$

This is very close to the value of 3.32 D found by Sharma et al. In addition, from Eq. (7.3), it results:

$$\varepsilon_{\text{opt}} = \frac{dD}{dE}$$

Taking the inverse of the slope of $E(D)$ yields $\varepsilon_{\text{opt}} = 1.79$, from which the refraction index is $n_{\text{opt}} = \sqrt{\varepsilon_{\text{opt}}} = 1.34$, in very close agreement with the experimental value of 1.33.

7.2.4 "Protonic" permittivity ($\chi_{opt} = 0$)

In this section, we look for the permittivity of ice as a polar, but non-polarizable medium, assuming that it is made of dipoles of fixed moment $\vec{\mu}$. Notice however a subtlety, in the fact that the electronic response does play a partial role here in the very definition of $\vec{\mu}$ as given in Eq. (7.1). In other words, only the electronic response to microscopic, dipolar fields is still on, while it is turned off with respect to the macroscopic displacement field.

7.2.4.1 Statistics

Keeping the same notations, let us consider a piece of material of volume Ω and dipole moment $\vec{M}$, which is a function of the configuration ν of its dipoles. The susceptibility χ is by definition the ratio of the average polarization over the electric field:

$$\chi = \frac{\langle M_z \rangle}{\varepsilon_0 \Omega E} \tag{7.7}$$

where here we are only interested in the z-direction. Assuming thermal equilibrium, the statistics of M_z follow Boltzmann's distribution:

$$\langle M_z \rangle = \sum_{\nu} \frac{M_z}{Z} e^{\frac{M_z E}{kT}} = \frac{kT}{Z} \frac{dZ}{dE}$$

where $Z = \sum_{\nu} e^{\frac{M_z E}{kT}}$ is the partition function. Differentiating once with respect to E:

$$\frac{1}{kT} \frac{d\langle M_z \rangle}{dE} = -\frac{1}{Z^2} \left(\frac{dZ}{dE} \right)^2 + \frac{1}{Z} \frac{d^2 Z}{dE^2} \tag{7.8}$$

Using the relation $\frac{1}{Z} \frac{d^2 Z}{dE^2} = \frac{\langle M_z^2 \rangle}{(kT)^2}$, we obtain:

$$\frac{d\langle M_z \rangle}{dE} = \frac{\langle M_z^2 \rangle - \langle M_z \rangle^2}{kT}$$

If, furthermore, the system is symmetric, the average dipole in the absence of external field should be zero, implying:

$$\left(\frac{d\langle M_z \rangle}{dE} \right)_{E=0} = \frac{\langle M_z^2 \rangle}{kT}$$

More generally, $\left(\frac{d^m Z}{dE^m}\right)_{E=0} = 0$ whenever m is odd. Now, differentiating Eq. (7.8) twice with respect to E:

$$\frac{1}{kT}\frac{d^3\langle M_z\rangle}{dE^3} = -\frac{6}{Z^4}\left(\frac{dZ}{dE}\right)^4 + \frac{12}{Z^3}\left(\frac{dZ}{dE}\right)^2\frac{d^2Z}{dE^2} - \frac{3}{Z^2}\left(\frac{d^2Z}{dE^2}\right)^2 + \frac{1}{Z}\frac{d^4Z}{dE^4}$$

from which the first two terms disappear when evaluating the expression at zero field:

$$\left(\frac{d^3\langle M_z\rangle}{dE^3}\right)_{E=0} = \frac{\langle M_z^4\rangle - 3\langle M_z^2\rangle^2}{(kT)^3}$$

Now writing a Taylor expansion for M_z:

$$M_z(E) = M_z(0) + M_z'(0)E + \frac{M_z''(0)}{2}E^2 + \frac{M_z'''(0)}{6}E^3$$

it comes:

$$\varepsilon_0\Omega\chi(E) = \frac{M_z(E)}{E} = M_z'(0) + \frac{M_z''(0)}{2}E + \frac{M_z'''(0)}{6}E^2$$

implying:

$$\chi(0) = \frac{M_z'(0)}{\varepsilon_0\Omega} = \frac{\langle M_z^2\rangle}{\varepsilon_0\Omega kT} \tag{7.9}$$

$$\chi''(0) = \left(\frac{d^2\chi}{dE^2}\right)_{E=0} = \frac{M_z'''(0)}{3\varepsilon_0\Omega} = \frac{\langle M_z^4\rangle - 3\langle M_z^2\rangle^2}{3\varepsilon_0\Omega(kT)^3} \tag{7.10}$$

Moreover, it is possible to prove that for N independent dipoles $\vec{\mu}$ with an isotropic orientation distribution[2]:

$$\langle M_z^2\rangle = \frac{N}{3}\mu^2$$

[2]For N independent, identical and isotropic dipoles:

$$\begin{aligned}\langle M_z^4\rangle &= \langle(\mu_{1z} + ... + \mu_{Nz})^4\rangle \\ &= \langle N\mu_{1z}^4 + \frac{N(N-1)}{2}\cdot 6\cdot\mu_{1z}^2\mu_{2z}^2\rangle \\ &= N\langle\mu_z^4\rangle + 3N(N-1)\langle\mu_z^2\rangle^2\end{aligned} \tag{7.11}$$

And:

$$\langle M_z^2\rangle = N\langle\mu_z^2\rangle \tag{7.12}$$

Using Eqs. (7.11) and (7.12):

$$\langle M_z^4\rangle - 3\langle M_z^2\rangle^2 = N\left(\langle\mu_z^4\rangle - 3\langle\mu_z^2\rangle^2\right) \tag{7.13}$$

$$\langle M_z^4 \rangle - 3\langle M_z^2 \rangle^2 = -\frac{2}{15} N\mu^4$$

Using that, Eqs. (7.9) and (7.10) can be rewritten:

$$\boxed{\chi(0) = \frac{\langle M_z^2 \rangle}{\varepsilon_0 \Omega k T} = \frac{n\mu^2}{3\varepsilon_0 k T} G} \tag{7.14}$$

$$\boxed{\chi''(0) = \frac{\langle M_z^4 \rangle - 3\langle M_z^2 \rangle^2}{3\varepsilon_0 \Omega (kT)^3} = -\frac{2}{45} \frac{n\mu^4}{\varepsilon_0 (kT)^3} G_2} \tag{7.15}$$

where, in the case of independent dipoles, $G = G_2 = 1$. To check that this is correct, we remind that the Langevin-Debye theory for independent and isotropic dipoles provides an explicit analytical formula for the susceptibility [188]:

$$\boxed{\chi = \frac{n\mu}{\varepsilon_0 E} \left[\coth\left(\frac{\mu E}{kT}\right) - \frac{kT}{\mu E} \right]} \tag{7.16}$$

Applying on that the asymptotic expansion $\coth(x) = \frac{1}{x} + \frac{x}{3} - \frac{x^3}{45}$ brings, for small fields:

$$\chi \sim \frac{n\mu^2}{3\varepsilon_0 k T} - \frac{n\mu^4}{45\varepsilon_0 (kT)^3} E^2$$

which is equivalent to Eqs. (7.14) and (7.15) provided that $G = G_2 = 1$.

The experimental value of ice Ih permittivity at the melting point is 96 [189]. Given Eq. (7.14) and the value of μ shown in Eq. (7.6), G should be equal to 2.46. Interestingly, as Sharma et al. already pointed out, this is very close to the estimate by Barkema and Boer with their classical, point-charge model of water-water interactions. In the following, we look for an estimate of G and G_2 first without, then including, DFT energy differences between proton configurations.

Performing integrals with the isotropic distribution, we find:

$$\langle \mu_z^2 \rangle = \frac{\mu^2}{3}$$

$$\langle \mu_z^4 \rangle = \frac{\mu^4}{5}$$

Putting that in Eq. (7.13), we obtain:

$$\langle M_z^4 \rangle - 3\langle M_z^2 \rangle^2 = -\frac{2N}{15} \mu^4$$

7.2.4.2 Monte Carlo algorithm

Now the purpose is to determine the permittivity of ice, a system in which dipoles are not independent, due to ice rules. This is, mathematically, a very difficult problem, and no exact solution has been found so far, thus calling for statistical approaches. Similarly, we here opt for the Monte Carlo technique in order to determine the statistics of the dipole:

- **Simulation cell** - A supercell $n_x n_y n_z$ is constructed using the unit cell defined earlier. Periodic boundary conditions are assumed.
- **Starting point** - An initial configuration respecting ice rules is easy to find by placing all protons in the upward position.
- **Move algorithm** - One needs to move within the configurational space that respects ice rules. The Rick-Haymet algorithm has been shown adequate while ensuring ergodicity: (a) randomly select a molecule in the cell - (b) randomly choose one of its four neighbors; it is connected to it through an "outgoing" or an "incoming" hydrogen bond - (c) starting from this new molecule, randomly select one of the two neighbors to which it is connected with the same directionality (outgoing or incoming) - (d) repeat step c until the resulting path crosses itself (always happens in a finite system); from that, it is possible to extract a loop along which all hydrogen bonds are in the same direction - (e) inverse all hydrogen bonds inside the loop (which amounts to rotating every molecule of the loop around the axis of its hydrogen bond that does not belong to the loop); a new configuration has been found which respects ice rules.
- **Acceptance** - Acceptance of a move is determined by the change in energy.
- **Dipole** M_z - Like for the calculation of the maximum polarization, the dipole of a configuration in the z-direction is determined by assigning a dipole $\vec{\mu}$ to every molecule in the supercell (with different orientations) and projecting them on the vertical axis.

7.2.4.3 Equipartition of proton configurations

First, energy differences between proton configurations are ignored. At every step of the Monte Carlo algorithm, the trial configuration is accepted. Simulations of 10 million steps are performed for different sizes of the supercell. From the dipole distribution, $\langle M_z^2 \rangle$ and $\langle M_z^4 \rangle$ are calculated, from which G and G_2 can be determined (Table 7.1). Convergence on G is clearly achieved, interestingly for a supercell as small as 222. The convergence value, 3.04, is consistent with the value found by Nagle with his expansion series method for perfect hexagonal ice. By contrast, convergence on G_2 seems much more difficult to obtain. For the larger cells 444 and 555, values of G_2 reported in parenthesis are manifestly far from convergence, implying

Table 7.1: Values of G and G_2 found after 10-million-step Monte-Carlo runs in supercells of increasing size.

Supercell	G	G_2
111	3.53	60.13
211	2.86	32.69
222	3.04	60.24
333	3.04	61.06
444	3.04	(18.95)
555	3.04	(132.93)

that a simulation much longer than 10 million steps would be required. However, based on the rapid convergence on G, we postulate that results for 222 and 333 are enough to get information on the real statistics. Plugging values of G and G_2 of supercell 222 into Eqs. (7.14) and (7.15) with the value of μ found earlier, we get, at 273 K:

$$\chi_{273}(0) = 117$$

$$\chi''_{273}(0) = -2.83 \times 10^5 \text{ (Å/V)}^2$$

Furthermore, from the dipole distributions of simulations 222 and 333 (Fig. 7-6), we can explicitly calculate the average polarization as a function of field, and using Eq. (7.7), deduce the susceptibility $\chi(E)$. The corresponding curves are in red and orange in Fig. 7-7. Clearly, the hump in the orange curve is unphysical and must therefore be attributed to a poor sampling in the 333 supercell. Fig. 7-6 suggests that the most probable source of error is in high polarizations, where an uncertainty in the already very small probability must have a dramatic impact. As the supercell gets larger, high-polarizability configurations become rare events, with a probability decreasing exponentially with supercell size. Simulations of 10 million steps are too short to obtain a correct statistical sampling. Considerably longer simulations would be required to converge the 333 supercell, and brute-force convergence on larger cells would be virtually impossible. In an attempt to overcome this problem, we tried to apply the umbrella sampling method. The idea is to add a constraint on the configuration polarization in order to explore a limited window around a given polarization, and calculate its free energy profile. Varying the constraint, other windows are explored, and in the end, the full free energy profile can be reconstructed by aligning profiles at the boundary between windows. We found that this method was not successful in the case of ice because of the peculiar "connectivity" of the

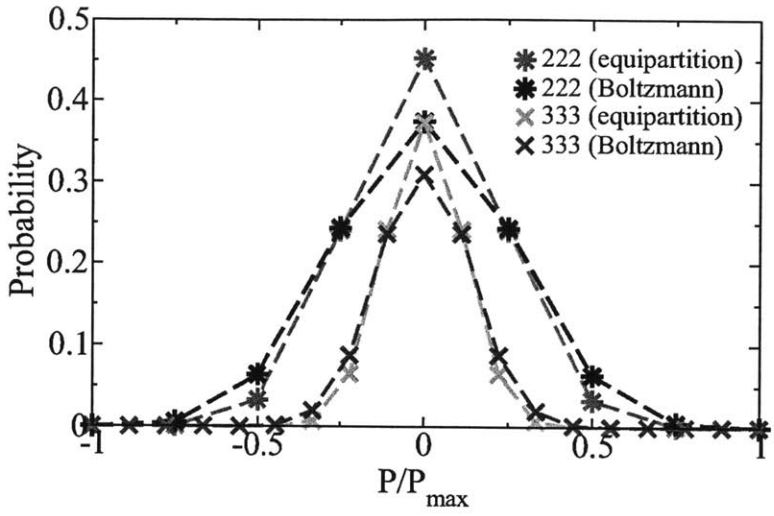

Figure 7-6: Polarization probabilities in 222 and 333 supercells obtained from Monte Carlo runs. Only individual points have a meaning. Lines are only to guide the eye, and must not be taken for probability distributions.

configurational space. More precisely, when the system is in a high-polarization state, there are very few moves that lead directly to another state of comparable polarization. The system has to follow a detour, by which it loses great part of its polarization, and then is polarized again in order to reenter the original window in a different configuration. This poor intra-connectivity of high-polarization windows is what prevents the umbrella sampling approach from working.

As an alternative strategy, we decided to estimate how reliable the susceptibility of supercell 222 (red line) can be. For that purpose, two lines are drawn corresponding to what the asymptotic behavior of the susceptibility must be at low and high fields. One (magenta dashed line in Fig. 7-7) is the parabola of maximum $\chi_{273}(0)$ and curvature $\chi''_{273}(0)$. The other (blue dashed line) is the hyperbola $\frac{P_{max}}{\varepsilon_0 E}$, representing the system under dielectric saturation. The true susceptibility curve must converge towards each of these curves in the corresponding field regimes. Arguably, these are rather restrictive conditions, which are perfectly satisfied by the red curve, in contrast with the orange curve.

Conclusion - Most likely, the field dependence of the susceptibility is well predicted by the results of the 10-million-step Monte-Carlo run in a supercell of size 222.

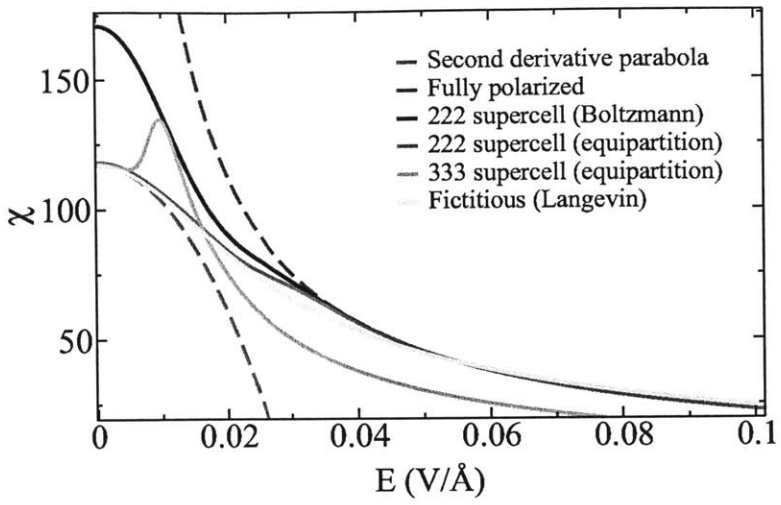

Figure 7-7: "Protonic" susceptibility vs. electric field with different approximations. For 222 and 333 supercells, χ is computed directly from polarization probabilities. The system of independent dipoles (Langevin) is fitted so that $\chi(E)$ agrees with the correlated system to the second order around the origin.

7.2.4.4 Boltzmann distribution of proton configurations

Now, we want to assess the effect of energy differences between proton configurations. Following the method introduced by Knight et al. [179], a discrete hamiltonian is developed for the hydrogen bond lattice. Each bond constitutes a site, receiving value -1 or 1 depending on the orientation of the bond. Nearest-neighbor interactions are for bonds sharing an oxygen atom, while second-nearest neighbor interactions are for bonds connected to a third bond in common. The total energy of a configuration is developed as:

$$E_{\text{tot}} = \beta_1 \Pi_1 + \sum_{\gamma} \beta_2^{\gamma} \Pi_2^{\gamma}$$

where[3]:

$$\Pi_1 = \sum_{i,j \in S_1} s_i s_j$$

[3] In fact, it is slightly more subtle than that. Bonds are oriented "arbitrarily" in the first place. Therefore, in the actual algorithm, an additional product is placed in front of $s_i s_j$ so that a product value ± 1 has always the same geometric meaning. In our case, +1 means that both bonds are converging to (or diverging from) the bond that they have in common.

$$\Pi_2^\gamma = \sum_{i,j \in S_2^\gamma} s_i s_j$$

and:

- S_1 are pairs of first-nearest neighbors;
- β_1 is the energy coefficient for first-nearest-neighbor interaction (one coefficient is assumed);
- S_2^γ are pairs of second-nearest neighbors of given symmetry γ;
- β_2^γ is the corresponding energy coefficient;
- s_i is the value of site i (± 1).

It is possible to show that ice rules cause the first-nearest neighbor sum to be always equal to 0. For second-nearest neighbors, we refer to Fig. 7-1 to describe the interaction symmetry. There are six possibilities and for each, we give a representative pair of the symmetry:

$\gamma = 1$: a-c
$\gamma = 2$: a-d
$\gamma = 3$: d-e
$\gamma = 4$: e-g
$\gamma = 5$: b-f
$\gamma = 6$: a-f

Actually, products Π_2^γ derived from these interactions are not independent, still because of ice rules. It may be shown that $(1, \Pi_1, \Pi_2, \Pi_5)$ is a "basis", and simply (Π_1, Π_2, Π_5) for evaluating energy differences. Coeffficients β_2^1, β_2^2 and β_2^5 were determined by computing DFT energies[4] for 14 proton configurations of our unit cell (any other configuration among the 114 allowed ones have the same product vector as one of these 14). Different functionals were tested as well as the effect of relaxation (Table 7.2), showing moderate differences. Then, cross validation of the coefficients was performed against DFT energy results for the representative 65 proton configurations of the $2\times1\times1$ supercell (2970 configurations in total) (Fig. 7-8).

Monte Carlo runs with the same algorithm as previously were performed on the 222 and 333 supercells including energy differences. The acceptance of a trial configuration of higher energy is designed to respect Boltzmann statistics. Subsequent polarization probabilities are shown in black and purple in Fig. 7-6. It is already apparent that the energy correction tends to favor

[4]Energies are calculated in a regular periodic-boundary setup with no electrostatic correction. This is exactly what we need. What interests us is differences in *chemical* energies. Energies must be obtained for configurations in zero field. Fluctuations may create local polarizations, but the macroscopic field is zero. This is what the PBC DFT calculation recreates artificially when implicitly introducing an artifical "background" field for polarized configurations.

Table 7.2: Fitted coefficients (eV) of the discrete hamiltonian from different DFT functionals.

Functional	β_2^1	β_2^2	β_2^5
GGA (PBE) (unrelaxed)	1.00×10^{-3}	4.96×10^{-4}	7.05×10^{-4}
GGA (PBE) (relaxed)	1.26×10^{-3}	6.24×10^{-4}	4.90×10^{-4}
LDA (PZ)	1.22×10^{-3}	5.96×10^{-4}	4.79×10^{-4}
vdW-DF	1.20×10^{-3}	5.72×10^{-4}	5.80×10^{-4}

global states of larger polarization. The resulting susceptibility $\chi(E)$ for the 222 supercell is showned in black in Fig. 7-7. Characteristics for the permittivity are then:

$G = 4.43$
$G_2 = 144.67$
$\chi_{273}(0) = 170$
$\chi''_{273}(0) = -6.80 \times 10^5$ (Å/V)^2

The predicted value of the zero-field permittivity is now further from the experimental value. In DFT, the configuration of lowest energy is the one precisely depicted in Fig. 7-1 (also the cross in (0,0) in Fig 7-8). In a layer, molecules lying flat are all oriented in the same direction, hence a large negative value of Π_2^1 and a strong energy benefit through the largest coefficient β_2^1. However, successive layers are oriented in opposite directions, making this configuration anti-ferroelectric horizontally. By contrast, all vertical bonds point in the same direction, hence a ferroelectric behavior vertically. These observations are consistent with findings by Knight et al. Performing Monte Carlo runs for decreasing temperatures, they obtained a first-order phase transition toward the ferroelectric state at 98 K, in agreement with an observed transition at 72 K in KOH-doped ice samples. By contrast, Barkema et Boer find a decreasing value of G upon cooling, with convergence to a anti-ferroelectric state with $G = 0$. Of course, G is not measurable, because the molecular dipole moment in bulk ice is not accessible. Various alternatives are possible to rationalize these elements:

- G is indeed larger than 3 because of a tendency to ferroelectricity, and the value of μ is overestimated by DFT.
- G is smaller than 3. DFT predictions are wrong. Furthermore, the experimental phase transition is in fact due to KOH impurities.
- Ice is a material far more complicated than the one simply described here.
- Etc.

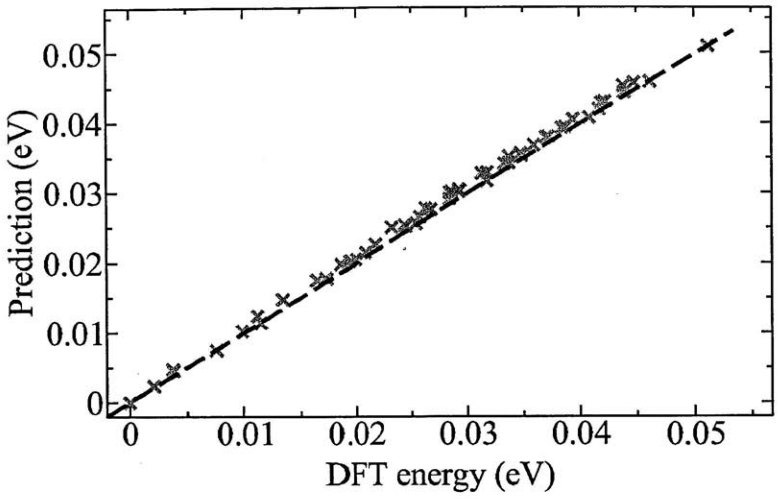

Figure 7-8: Cross validation for the hamiltonian coefficients. x-axis: relaxed GGA-DFT relative energies for the 211 supercell (16 molecules in total); y-axis: values predicted from the discrete hamiltonian.

Performing simulations with classical potentials including TIP4P, Aragones et al. suggested that G is, in this case, related to the ratio of the dipolar to quadrupolar moment [190].

7.2.5 Effect of polarizability ($\chi_{\text{opt}} \neq 0$)

7.2.5.1 Clausius-Mossotti correction

Let us turn on the molecular polarizability. For every dipole configuration in the system, a field $\vec{E}$ exists as a result of the displacement field, of the dipole arrangement, and of the material electronic response. As expressed in the Clausius-Mossotti formalism, the external field acting on a molecule, $\vec{E}_{\text{ext}}$, is larger than the total field $\vec{E}$, the difference coming from electronic polarization of the molecule itself:

$$E_{\text{ext}} = \frac{n_{\text{opt}}^2 + 2}{3} E$$

The "protonic" response to $\vec{E}_{\text{ext}}$ is given by the previous statistical treatement. Therefore, the total permittivity at zero field becomes:

$$\varepsilon(0) = 1 + \chi_{\text{opt}} + \chi_{273}(0)\frac{E_{\text{ext}}}{E} = \varepsilon_{\text{opt}} + \chi_{273}(0)\frac{n_{\text{opt}}^2 + 2}{3} \tag{7.17}$$

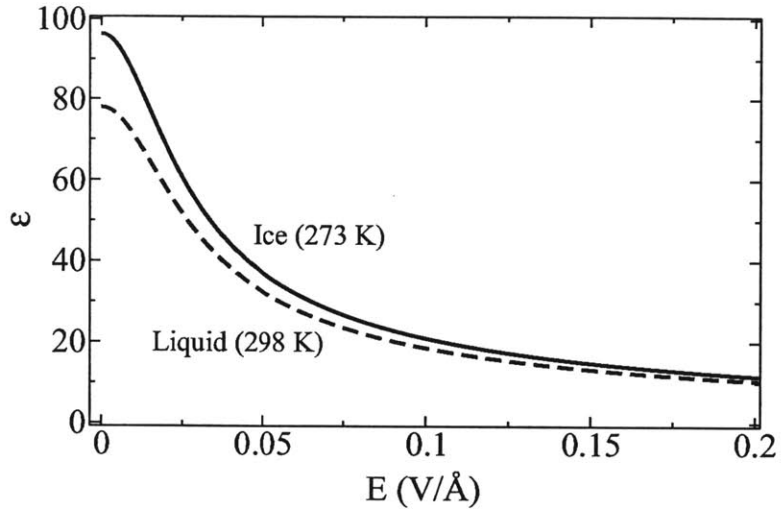

Figure 7-9: Total permittivity vs. electric field.

7.2.5.2 Comparison with Onsager's formula

In Onsager's theory, the final implicit expression for the permittivity at low field is:

$$\frac{(\varepsilon - n_{\text{opt}}^2)(2\varepsilon + n_{\text{opt}}^2)}{\varepsilon(n_{\text{opt}}^2+2)^2} = \frac{4\pi n}{9kT}\mu_c^2$$

After some simplifications based on assumption that $n_{\text{opt}}^2 \ll \varepsilon$, the increase of ε upon inclusion of the electronic response is:

$$\frac{\varepsilon}{\varepsilon_{n_{\text{opt}}=1}} = \left(\frac{n_{\text{opt}}^2+2}{3}\right)^2$$

Notice the factor $\left(\frac{n_{\text{opt}}^2+2}{3}\right)^2$ as opposed to simply $\frac{n_{\text{opt}}^2+2}{3}$ in Eq. (7.17). This difference is reminiscent of the distinction between μ_c and μ introduced at the very beginning. In Onsager's theory, when the electronic response is turned on, a double polarization acts on the dipole: one from the reaction field, the other by the cavity field. In our case, the effect of the reaction field is already embedded in μ, implying that only polarization by E remains to be included, hence the simple factor.

The effect of polarization adds to the discrepancy with experiment.

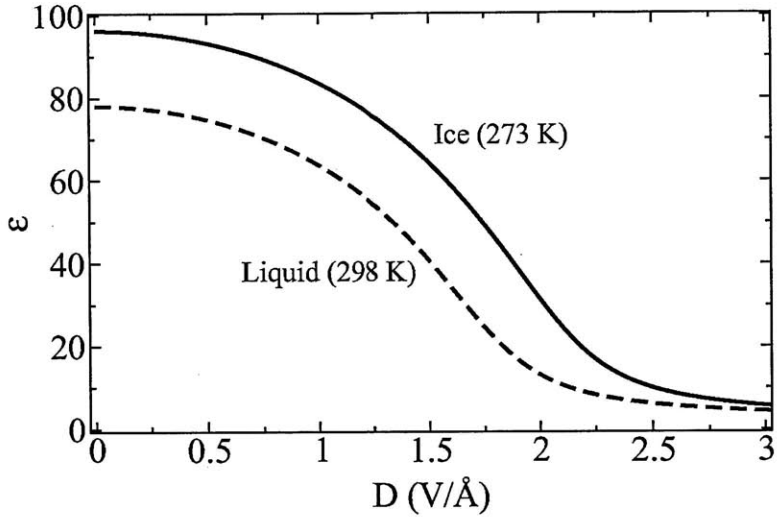

Figure 7-10: Total permittivity vs. displacement field.

7.2.6 Fictitious system of independent dipoles

For the following, it would be convenient to have an analytical expression for the permittivity of water as a function of field. First, we perform a fit of the susceptibility of ice that we found in the equipartition case (on the 222 supercell) and without polarizability effects, so that uncertainties on the real value of G are factored out. The fit has the simplest form of a Langevin function, implying a fictitious system where dipoles are independent. As apparent in Eq. (7.16), the Langevin-Debye model has only two parameters, the material density n and the individual dipole moment μ. Let us denote $\tilde{n}$ and $\tilde{\mu}$ those quantities for the fictitious system. One possible approach is to impose that the fictitious system should have the same $\chi(0)$ and $\chi''(0)$ as the real system. First, getting rid of $\tilde{n}$:

$$\frac{\chi(0)}{\chi''(0)} = -\frac{15}{2}\frac{(kT)^2}{\tilde{\mu}^2}$$

implies:

$$\tilde{\mu} = kT\sqrt{\frac{15}{2}\frac{(-\chi''(0))}{\chi(0)}}$$

From there, $\tilde{n}$ can be found using the relation:

$$\chi(0) = \frac{n\tilde{\mu}^2}{3\varepsilon_0 kT}$$

Numerically, those relations give:

$$\tilde{\mu} = 3.17 \text{ eÅ (as opposed to } \mu = 0.70 \text{ eÅ)}$$

$$\tilde{n} = 4.55 \times 10^{27} \text{ m}^{-3}$$

The susceptibility of this fictitious system is plotted in Fig. 7-7 (green curve) and has equation:

$$\chi = \frac{\tilde{n}\tilde{\mu}}{\varepsilon_0 E}\left[\coth\left(\frac{\tilde{\mu}E}{kT}\right) - \frac{kT}{\tilde{\mu}E}\right] \tag{7.18}$$

It is very close to the red curve, and in particular, the deviation at high fields does not exceed 2. Not so surprisingly, ice rules induce a correlation between dipoles, so that on a mesoscopic level, everything appears as if ice was made of larger dipoles. The plot of ε as a function of E is shown in Fig. 7-9 (solid line). Here, ε is scaled to reproduce the experimental permittivity at low field. It can also be convenient to have ε as a function of D (Fig. 7-10), obtained from numerical resolution of self-consistent equation $\varepsilon = \varepsilon(D/\varepsilon)$ for any given value of D.

What about liquid water? The permittivity of liquid water at room temperature is known to be 78, corresponding to a 14.4% decrease with respect to permittivity of ice at the same temperature (89). Heats of fusion and vaporization for water are respectively 6.01 kJ/mol and 40.65 kJ/mol, implying a heat of sublimation equal to 46.66 kJ/mol, and an energy of 0.12 eV per hydrogen bond. Upon fusion, $6.01/46.66 = 12.9\%$ of hydrogen bonds are broken. It is therefore interesting to conclude that in this regime, G scales with the number of hydrogen bonds. However, this simple analysis gives no information on the behavior of G_2. Here, we obtain the permittivity of water simply by scaling the one of ice. Then, $\varepsilon(D)$ is calculated by resolution of the same self-consistent equation as previously. Results are the dashed lines in Figs. 7-9 and 7-10.

7.2.7 Connexion with experiment

If the permittivity of water is well studied as a function of field frequency [191], measures of the saturation effect seem more limited. Here, a connexion with the work of Pajkossy and Kolb is proposed [140]. Using impedance spectroscopy methods, they determined the double-layer capacitance of Pt(111) single crystal electrodes. As a reminder, the total, pseudo-capacitance at the electrode-electrolyte interface is the sum of the double layer capacitance (the "real" capacitance), c_{dl}, and the faradaic capacitance (due to electrosorption reactions), c_{ad}. By using a high-frequency potential excitation exceeding the kinetics of adsorption, they

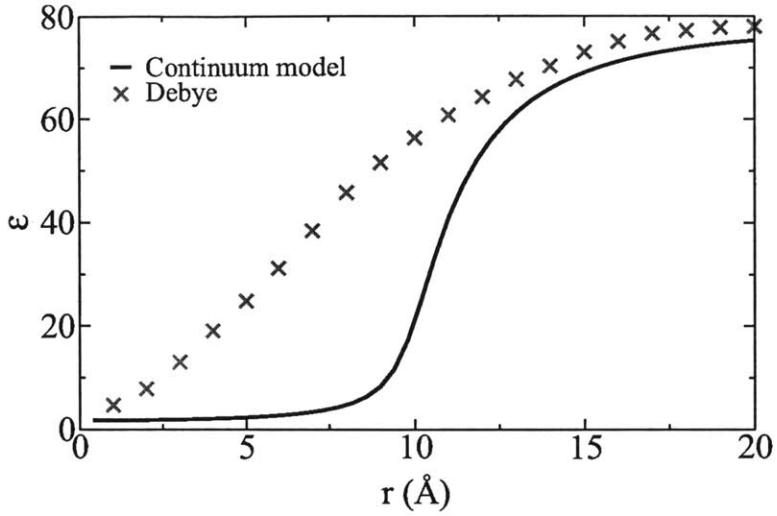

Figure 7-12: Permittivity saturation around an ion, as predicted by Debye and in our continuum model.

The plot is in Fig. 7-12, and values predicted in the work of Debye are also reported. Dielectric saturation begins at comparable distances in both theories, but at shorter distances, the continuum model predicts a stronger dipole alignment.

7.3.2 Frumkin effect

7.3.2.1 Apparent vs. intrinsinc rate constants

Accurate measurement or prediction of electrochemical reaction rates is an important element in the development of catalytic models. The influence of the double layer structure on interfacial reaction rates was studied by Frumkin in the 30s, who brought to light a phenomenon which today is known as the *Frumkin effect*. Let a reaction be at the metal-electrolyte interface, where one of the reactant is a species in solution, for instance a proton:

$$A^* + H^+ + e^- \rightarrow AH^*$$

A current is measured and related to the proton bulk concentration $[H^+]_0$ through a rate constant k_0 and the Butler-Volmer relation:

$$i = k_0 \exp\left(-\frac{e\alpha\eta}{kT}\right)[H^+]_0 \tag{7.19}$$

Applying this formula at low fields, with $\varepsilon_{298}(0) = 78$ for the bulk permittivity, gives $c_{\mathrm{dl}} = 231\ \mu\mathrm{F/cm}^2$, which is more than twice the actual measured value. If $\tilde{\mu}$ is assumed to be correct, as justified previously, it implies that $\tilde{n}$ in Eq. (7.18) should have a lower value in this interfacial environment. A qualitative argument can easily be made in this direction. Counterions in the vicinity of the compact layer screen the electrode field, implying that the average field acting on dipoles of the compact layer, and on their correlated dipoles just outside, is smaller than the field in the compact layer. Energetically speaking, this is equivalent to having the same value of the field with *fewer* dipoles subject to it, that is a smaller density $\tilde{n}$.

Conclusion - Application of the bulk model to the prediction of saturation effects at an interface should be considered with care. A more extended study should address aspects which may not be neglected: the contribution of the diffuse layer to the capacitance (at 0.1 M, it should already be substantial); the chemical interaction with the metal [192, 193]; general steric effects; the broken translational symmetry at the interface; etc. However, interesting connexions can be drawn leading to a better understanding of dielectric saturation effects.

7.3 Saturation effects in electrolytes

Here, results from the previous section are included in continuum models quantifying the effect of dielectric saturation on the behavior of electrolytes.

7.3.1 Saturation by ions

The field created in the vicinity of an ion in solution is strong enough to produce complete orientation of water molecules in the hydration sheath and to some extent beyond. Combination of this effect from a collection of ions in solution induces a general decrease of the electrolyte permittivity. Known as *dielectric decrement*, it is a function of ionic concentration. At strong molarities, a change in slope occurs due to partial recombination of anions and cations, lowering the local strength of the field. More generally, calculation of the dielectric decrement is difficult, owing to the complex structure of the electric field in the electrolyte and to additional contribution from chemical interactions. Here instead, dielectric saturation of the solvent by a single ion is calculated. The approach assumes the solvent to be a continuum, whose permittivity is a function of displacement field as given by the dashed line of Fig. 7-10. The displacement field at a distance r from the ion center comes directly from Gauss' law. In case of a monovalent cation of charge e:

$$D(r) = \frac{e}{4\pi\varepsilon_0 r^2}$$

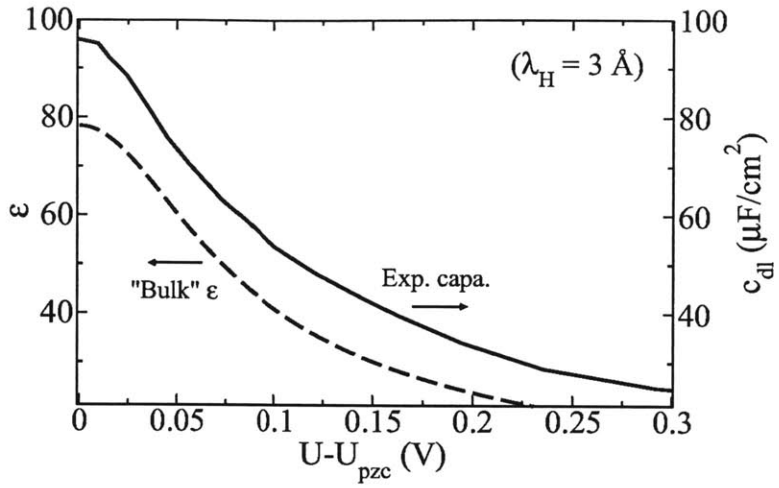

Figure 7-11: Comparison of permittivity saturation effects in our model and from measuring the double layer capacitance. Measures by impedance spectroscopy are described in [140]. Note the different axis: the theoretical permittivity is reported, which can in general be related to the capacitance.

were able to suppress the faradaic response and measure the contribution from the sole double-layer capacitance. They found that the capacitance has a maximum for a given value of the electrode potential, which they identified with the potential of zero charge; then, as the potential is moved above or below that value, the capacitance drops rapidly, an effect that they attributed to the saturation of water permittivity in the double layer. Let us find out if our results agree quantitatively with their measures. In case of a strong electrolyte molarity, most of the potential drop in the double layer occurs inside the compact layer, also known as Helmholtz layer. The potential drop is then related to the field by $\Delta V = E\lambda_H$, where λ_H, the thickness of Helmholtz layer, is commonly taken to be equal to 3 Å, roughly the thickness of a water layer. On the same figure (Fig. 7-11), let us have on one hand the experimental measure of the capacitance as a function of potential, and on the other hand the permittivity as given by the dashed line of Fig. 7-9, plotted as a function of potential by means of the field-potential correspondance that was just mentioned. The very close trends of c_{dl} and ε suggest that direct application of our bulk model (no surface effects have been included) is good at capturing saturation effects in the double layer. More precisely, the field dependence of ε is coded in $\tilde{\mu}$, which itself includes both the magnitude of the water molecule dipole and the effect of dipole-dipole ice-rule correlations. Now turning to the absolute value of the capacitance, and looking at the compact layer only, the expression is:

$$c_{\mathrm{dl}} = \frac{\varepsilon_0 \varepsilon}{\lambda_H}$$

where η is the overpotential (if it is negative, the reaction is faster) and now α is the symmetry factor. Microscopic details of the reaction are included in the rate constant. However, this kinetic equation assumes that the reaction proceeds directly from a proton in solution, which, in reality, is not the case. Usually, the proton has first to come into the surface vicinity, on the outer Helmholtz plane (OHP), and then only is likely to react. If the kinetics are not diffusion-limited, the second step is the rate determining one. The real, intrinsic rate constant k must then be defined based on the proton concentration $[H^+]$ at the OHP. If ions in solution are in thermal equilibrium, their concentration follows the Boltzmann distribution, and the proton concentration at the OHP is:

$$[H^+] = \exp\left(-\frac{e\Psi}{kT}\right)[H^+]_0$$

calling Ψ the potential at the OHP[5], with the convention that the potential far in the bulk of the electrolyte is 0. In addition, the overpotential felt by the electron is now[6] $\eta - \Psi$. Therefore, the reaction rate expression using the intrinsic rate constant is:

$$i = k\exp\left(-\frac{e\alpha(\eta-\Psi)}{kT}\right)\exp\left(-\frac{e\Psi}{kT}\right)[H^+]_0$$

Identification with Eq. (7.19) provides the expression of the intrinsinc rate constant k in terms of the apparent rate constant k_0:

$$k = k_0\exp\left(\frac{e(1-\alpha)\Psi}{kT}\right) \tag{7.20}$$

When $\Psi \geq 0$, relying on the bulk concentration leads to underestimate the reaction rate constant.

One way to determine the Ψ potential experimentally is by measuring a streaming potential in a parallel plate capillary system and relate it to the potential profile. The technique of the streaming potential has been extended to rotating disk electrodes [194].

[5]For that reason, the Frumkin effect was also called, in the Russian literature, the Ψ effect.

[6]Actually, the chemical potential of an electron remains $\Phi + \eta$. It is rather the energy of the ion that is affected by an amount $e\Psi$. The fact that we need to include this correction clarifies the definition of the intrinsic rate constant. It is defined at the potential of equilibrium and assumes that the proton is at zero potential. This is indeed a formal definition, since this is not what happens in reality. However, k does capture the specific energy path of electron transfer, and as such it is meaningful.

7.3.2.2 Dielectric saturation in the Gouy-Chapman model

Ψ is the potential change across the diffuse layer. Here, the purpose is to see how predictions by the Gouy-Chapman model are modified by the inclusion of dielectric saturation effects and how interfacial rate constants are in turn modified through the Frumkin effect. One has to solve the Poisson-Boltzmann equation in the case where the permittivity is a function of the field strength. The derivation was originally proposed by Conway, Bockris and Ammar [195], and is here reproduced[7]. The potential Φ in the diffuse layer must satisfy the Poisson equation:

$$-\mathrm{div}(\varepsilon(\Phi')\mathrm{grad}\Phi) = 4\pi\rho$$

where the ionic charge density ρ is given by the Boltzmann distribution:

$$\rho = nze\left(\exp\frac{-ze\Phi}{kT} - \exp\frac{ze\Phi}{kT}\right) = -2nze\sinh\frac{ze\Phi}{kT}$$

where here n is the absolute valency of ions ($+n$ and $-n$ for cations and anions respectively, assuming a symmetric electrolyte). Writing $k' = 8\pi nze$ and $k'' = \frac{ze}{kT}$, it comes:

$$\frac{d}{dx}\left[\varepsilon(\Phi')\Phi'\right] = k'\sinh k''\Phi$$

Developing the term in brackets, and then multiplying by $\Phi' dx = d\Phi$, gives:

$$\left[\Phi'\varepsilon(\Phi') + \Phi'^2\varepsilon'(\Phi')\right]d\Phi' = k'\sinh k''\Phi d\Phi$$

[7] If ε is a function of ionic concentration, therefore of Φ, like in the case of dielectric saturation, we propose the following derivation:

$$\frac{d}{dx}\left(\frac{d\Phi}{dx}\varepsilon(\Phi)\right) = 4\pi \times 2nze\sinh\frac{ze\Phi}{kT} = f(\Phi)$$

Multiplying by $\varepsilon(\Phi)d\Phi$:

$$\varepsilon(\Phi)\frac{d\Phi}{dx}d\left(\frac{d\Phi}{dx}\varepsilon(\Phi)\right) = \varepsilon(\Phi)f(\Phi)d\Phi$$

$$\frac{1}{2}d\left(\frac{d\Phi}{dx}\varepsilon(\Phi)\right)^2 = \varepsilon(\Phi)f(\Phi)d\Phi$$

$$\frac{d\Phi}{dx} = \frac{\left(2\int_0^\Phi \varepsilon(\Phi)f(\Phi)d\Phi\right)^{\frac{1}{2}}}{\varepsilon(\Phi)}$$

where boundary conditions in the solution bulk have been included. x is obtained from the relation:

$$dx = \frac{d\Phi}{d\Phi/dx}$$

In a more general case, ε would be a function of both ionic concentration and field.

Integrating by parts:

$$\left[\Phi'^2\varepsilon(\Phi')\right]_0^{\Phi'} - \int_0^{\Phi'} \Phi'\varepsilon(\Phi')d\Phi' = \frac{k'}{k''}\cosh k''\Phi - \frac{k'}{k''}$$

which can be rewritten:

$$F_1(\Phi') + \frac{k'}{k''} = \frac{k'}{k''}\cosh k''\Phi$$

where $F_1(\Phi')$ is a function of Φ' which can be calculated numerically. Inverting that relation, we obtain:

$$\Phi = \frac{1}{k''}\cosh^{-1}\frac{k''}{k'}\left[F_1(\Phi') + \frac{k'}{k''}\right] \tag{7.21}$$

x comes directly from:

$$x = \int \frac{dx}{d\Phi}d\Phi = \int \frac{d\Phi}{\Phi'} \tag{7.22}$$

Now, to determine the potential profile from those equations, we propose a slightly different procedure from the original paper:

(i) choose a maximum value of the field, Φ'_{max}, and divide the interval $[0, \Phi'_{max}]$ into N equal segments, defining N field values from $\frac{\Phi'_{max}}{N}$ to Φ'_{max} (e.g. N = 1000);

(ii) for every value of the field, compute the corresponding value of the potential using Eq. (7.21), and taking differences, compute $d\Phi$;

(iii) having $d\Phi$ and Φ', x can be obtained using Eq. (7.22).

In the end, one has Φ as a function of x. In the process, the boundary condition $\Phi' = 0 \Rightarrow \Phi = 0$ has been used. Interestingly, one can notice that the potential is computed segment by segment starting from the solution bulk, implying that the potential profile in this direction is agnostic to the final value of the potential at the electrode surface. However, the diffuse layer thickness does increase with potential.

Using this procedure, the potential profile is determined in an electrolyte of unit molarity, assuming the charge on the electrode is 20 μC/cm^2 (Fig. 7-13). The case where ε is constant and equal to 78, as in the original Gouy-Chapman model, is compared to the case where dielectric saturation is included (dashed line of Fig. 7-9). In the latter case, the field close to the OHP appears sufficiently strong to lower the value of ε, inducing a steeper potential evolution compared to the Gouy-Chapman result. The final potential difference between the two scenarios is

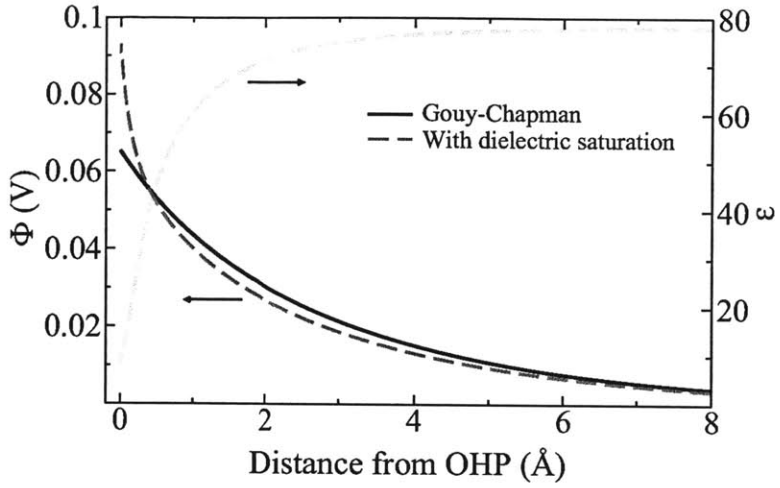

Figure 7-13: Longitudinal electric potential profile beyond the OHP with and without dielectric saturation. Solution concentration is 1 M, and charge on the electrode is 20 μC/cm^2.

relatively modest, around 25 mV. A more pronounced effect appears if looking at the uncertainty on the Frumkin effect in connexion with the reactant coordinate. If, instead of reacting on the OHP, the proton becomes active 1 Å ahead of it (which is only one third the thickness of a water monolayer), the potential at which it reacts changes by 20 mV in the Gouy-Chapman case, and by 60 mV if there is dielectric saturation. Referring to Eq. (7.20), the reaction rate then changes by a factor 1.5 and 3.2 respectively.

7.4 Summary

In this chapter, we have performed a multiscale study of water to assess its dielectric behavior in the strong electric fields of the double layer. We have experienced that water is a complex medium to understand and to simulate, and dipolar correlation effects are certainly still an open subject of debate. However, modularity of the multiscale approach allowed us to get an order of magnitude for the effects of dielectric saturation on reaction kinetics in the double layer. They appear to be rather small (although they should always be kept in mind), especially when compared to uncertainties on chemical energies.

Chapter 8

CO Adsorption on Transition Metals

8.1 CO in heterogeneous catalysis

CO is one of the most studied molecules in surface science. Reasons include the fact that it appears as an intermediate in a lot of hydrocarbon oxidation reactions or reforming processes[1], it is a simple molecule that can serve as a probe for chemical and electrostatic properties of the surface, it is also a strongly binding molecule with possible poisoning effects. This is notably the case in fuel cell devices. In proton exchange membrane fuel cells, experience suggests that concentrations well below 10 ppm are required for proper utilization of the anode catalyst. Therefore, determining appropriate catalysts for CO oxidation is a question of general interest. Here, the purpose is to present some elements of the research, including our own calculations on CO adsorption energies.

8.1.1 CO electrooxidation

It is usually accepted that CO electrooxidation proceeds through a Langmuir-Hinshelwood mechanism, where the first step is formation of OH adsorbates by water splitting:

$$H_2O \leftrightarrow OH_{ads} + H^+ + e^- \tag{8.1}$$

[1] For instance, the production of hydrogen from the reaction between methane and steam:

$$CH_4 + H_2O \rightarrow 3H_2 + CO$$

If a reformed hydrocarbon is to be used in a fuel cell, the carbon monoxide must be shifted to carbon dioxide using more steam:

$$CO + H_2O \rightarrow H_2 + CO_2$$

This water gas shift reaction does not easily go to completion, and some CO will be left in the reformed gas stream, on the order of 0.25 to 0.5% (2500-5000 ppm), with effects on the anode performance [196].

then reacting with CO on the surface:

$$CO_{ads} + OH_{ads} \rightarrow COOH_{ads} \tag{8.2}$$

followed by a second electron transfer:

$$COOH_{ads} \rightarrow CO_2 + H^+ + e^-$$

In strongly alkaline media, CO_2 reacts rapidly with OH^- ions to form carbonate ions CO_3^{2-} that can stay adsorbed on the surface [197]. Reaction (8.2) is believed to be the rate determining step, in particular on the basis of Tafel slopes measured in the 60 mV/dec vicinity (which also implies that OH is present at very low coverage). Furthermore, reaction (8.1) must be at equilibrium if, at fixed potential vs. SHE, one observes that activity increases like the pH. Assuming CO is in equilibrium with a gas phase and everything is in standard conditions, the equilibrium potential for the overall CO electrooxidation reaction is close to 0 V/RHE. However, CO oxidation currents in stripping voltammetry or bulk oxidation experiments on platinum are observed at much higher potentials, typically 0.6 V/RHE confirming the small rate of the limiting step. Koper et al. performed chronoamperometry experiments of CO oxidation on step surfaces [198]. They found that CO diffusion on the surface is fast enough so that a "mean-field" kinetic formalism can be used, and showed that the presence of steps on the surface is critical in increasing the activity by promoting formation of OH adsorbates.

8.1.2 Surface electronic structure

CO adsorbs strongly on platinum (Fig. 8-1). High coverages on the surface imply that CO-CO lateral interactions are important. Equilibrium is expressed by a Frumkin isotherm:

$$\frac{\theta_{CO}}{1-\theta_{CO}} = \exp\left[\frac{-E_{ads}(\theta_{CO}) - Ts}{kT}\right]$$

where the entropic free energy of CO in standard conditions is $Ts = 0.61$ eV, resulting in a CO surface coverage close to 0.7 ML. By contrast, below 0.6-0.7 V/RHE, OH is present at small coverages, described by a Langmuir isotherm:

$$\frac{\theta_{OH}}{1-\theta_{CO}} = \exp\left[\frac{-\Delta E_{split} - E_{ads}^{OH} + eU}{kT}\right]$$

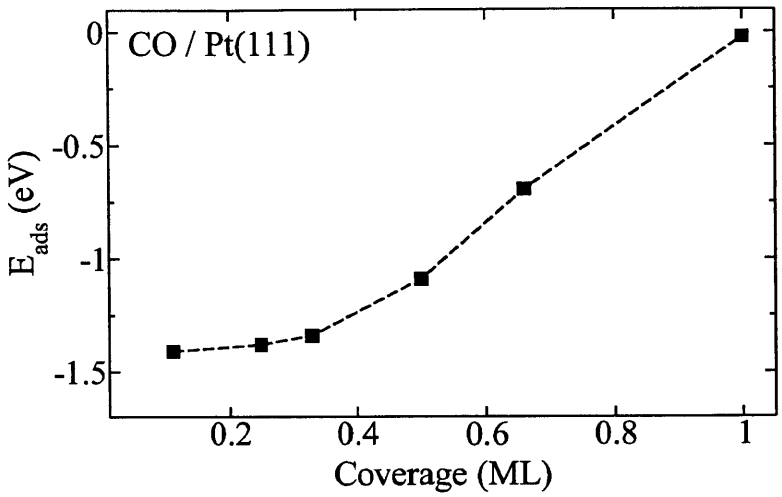

Figure 8-1: GGA CO adsorption energy on Pt(111) (atop site) vs. coverage. Here, only electronic energies are included. Curve has been shifted so that binding energies at low coverage match experimental enthalpies (reported in [199]). See next section for more information on this correction.

where $\Delta E_{\text{split}} = 3.37$ eV is the cost of the water splitting reaction (see Table 3.3).

Binding energies may be changed by tuning the surface electronic structure. For instance, in nanoparticles made of platinum and gold, a heat treatment leads to segregation of gold towards the surface, with various effects on the binding energy (Figs. 8-2 and 8-3):

- On Pt substrate, having gold only in the outmost layer has a moderate effect on CO binding energy (triangles in Fig. 8-3). This is consistent with electronic structure calculations showing an upshift of the Pt d-band center caused by neighboring Au [200].

- By contrast, when Au is introduced in underneath layers, binding energies are substantially reduced. Atop adsorption is more affected than fcc adsorption (not shown here), owing to the directionality of bonds: CO adsorbed on top interacts with the Pt d_{z^2} orbital, which is perpendicular to the surface.

- When the subtrate is gold, binding energies have a non-monotonic trend vs. the amount of Pt at the surface. If only the 2-3 outmost layers are made of platinum, electronic localization in these layers causes a d-band center upshift responsible for higher reactivity [201, 202]. As more Pt is added, the localization effect disappears (i.e. intra-metal hybridization widens d-band) and adsorption energies become less negative. The binding energy converges to a value which is still larger than on pure Pt(111), due to lattice

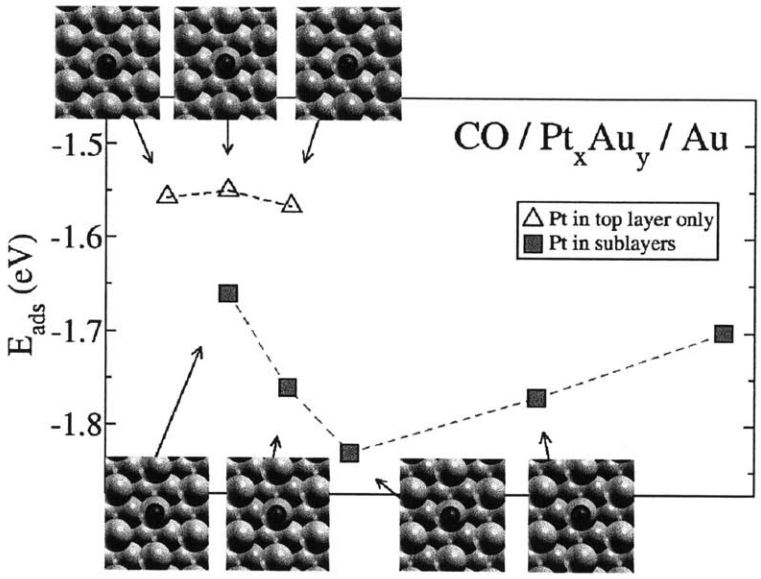

Figure 8-2: GGA CO adsorption energy (atop site) on Au substrate with Pt at the surface. Here, GGA electronic energies have not been corrected.

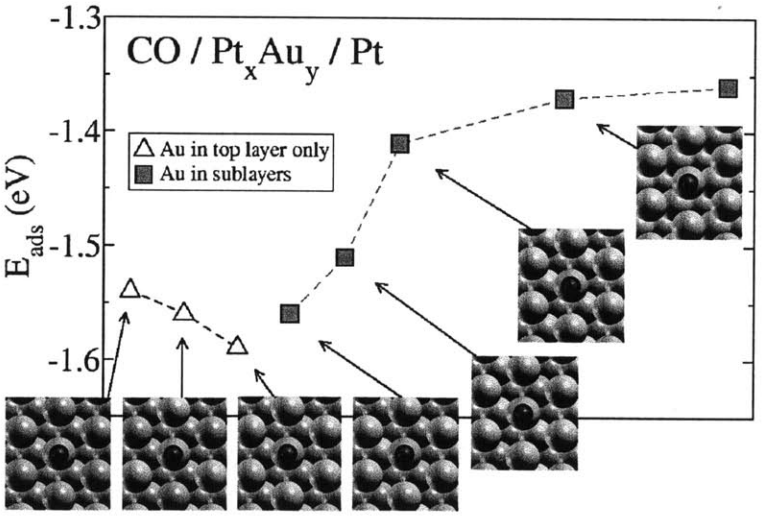

Figure 8-3: GGA CO adsorption energy (atop site) on Pt substrate with Au at the surface. Here, GGA electronic energies have not been corrected.

stretching from the gold substrate.

8.1.3 Guidelines for a good COox catalyst

Koper et al. have formulated guidelines for a good catalyst towards monoxide electrooxidation [197]:

- The pH range should be 8-10. Larger alkalinity should be avoided because of the formation of adsorbed carbonate which hinders CO diffusion on the surface.
- Cations such as Li^+ and Be^+ can improve water dissociation and the associated adsorption of oxygenated species.
- A high density of steps on the surface is desirable, for helping the formation of OH adsorbates as well.

Particularly, it was observed that CO oxidation is more active in alkaline media, and the understanding is still not complete. However, it is useful to remind that in alkaline medium, an electrode of given potential vs. RHE is in fact more negative. This implies the possibility that OH on the surface is stabilized by solvated cations attracted by the electrode [203].

8.2 CO adsorption puzzle

Accurate prediction of molecular adsorption energies is critical for all aspects of heterogeneous catalysis. Surface coverages, reaction barriers, surface stability, site selectivity are all derived from adsorption energies. DFT has proven successful in reaching chemical accuracy in a wide range of situations. However, sizable discrepancies with experimental measures may still be found in specific cases, notably molecular adsorption on transition metal surfaces. In this regard, the CO molecule, well studied experimentally, can be used as a benchmark to see whether a functional captures more of the subtle chemistry at the metal surface.

Specifically, GGA DFT overestimates CO adsorption energies on late transition metals and also, usually, finds erroneous ordering of adsorption sites. On Cu, Rh and Pt (111) surfaces, GGA predicts preferential adsorption on the fcc site, when in fact it is on the atop site. This discrepancy is sometimes called the "CO adsorption puzzle" [204]. By contrast, DFT performs well in the description of vibrational modes. The calculated CO stretching frequency is 2050 cm^{-1} on atop site vs. 1743 cm^{-1} on fcc site. Experimental frequencies vary between 1760-2070 cm^{-1} and a stronger peak around the upper value is evidence for atop adsorption.

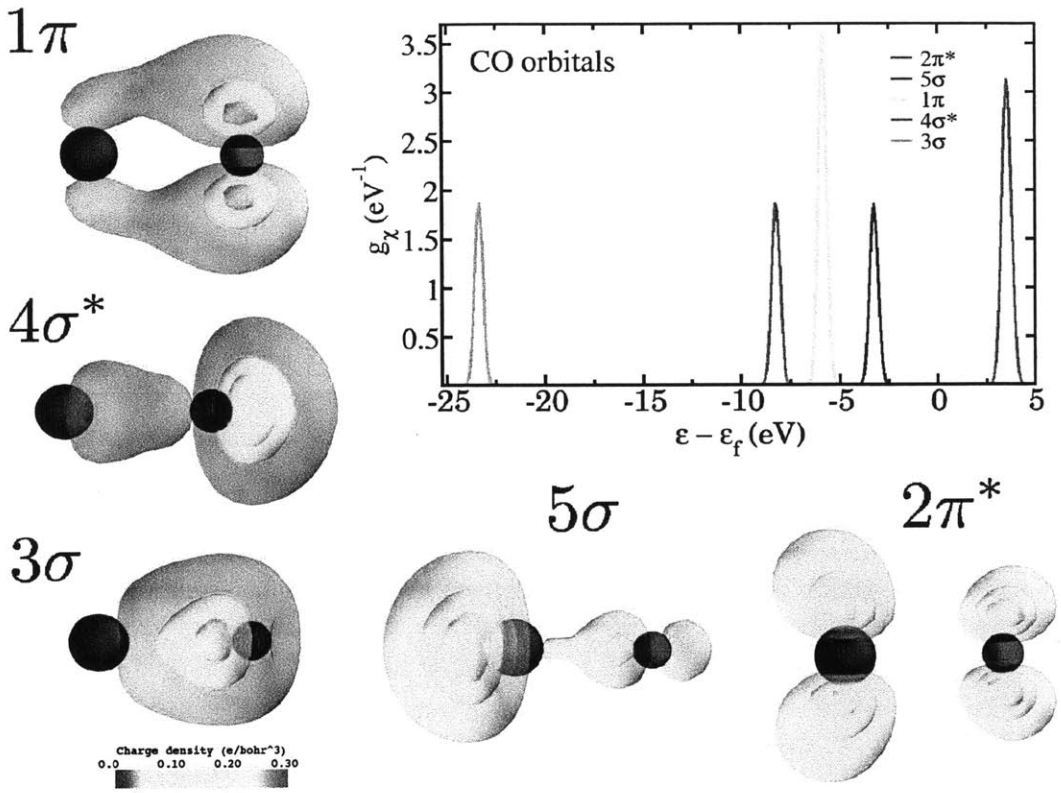

Figure 8-4: CO orbitals and their energies.

It has been argued that an important part of the puzzle comes from self-interaction in common local and semi-local DFT functionals, causing incorrect prediction of the one-electron energy gap. Equivalently, this is related to the inability of those functionals to correctly predict orbital energies at non-integer occupations. While energy vs. occupation should be a series of straight lines connecting at integer occupations, self-interaction results in a convex curve, thus favoring electronic structures with partially occupied states [205]. In the case of CO, it leads to underestimate the HOMO-LUMO gap and to predict excessive hybridization between metal orbitals and the CO LUMO state (Fig. 8-4). This excess of back-donation, in turn, artificially favors adsorption on site geometries with more overlap with the 2π orbital. By contrast, orbital-resolved force analysis shows that back-donation contributes negligibly to the vibrational spectrum, explaining why DFT predicts correct stretching frequencies.

One attempt to correct for self-interaction is to reintroduce part of the exact electronic exchange by means of hybrid functionals. Good results for CO binding energies and site ordering are

Table 8.1: Lattice constants (Å) calculated with different functionals. Numbers in parenthesis are percent errors with respect to experiment. Experimental values are taken from http://www.webelements.com/, and have not been extrapolated to 0 K (an adjustment that would change the value by no more than ~0.1%).

	Exp.	PBE	RevPBE	PBE-vdW	RevPBE-vdW
Cu	3.61	3.67 (1.7)	3.71 (2.8)	3.72 (3.0)	3.76 (4.1)
Rh	3.80	3.86 (1.5)	3.88 (2.1)	3.89 (2.4)	3.91 (2.8)
Pd	3.89	3.97 (2.0)	4.00 (2.8)	4.02 (3.3)	4.05 (4.1)
Ag	4.09	4.16 (1.7)	4.20 (2.7)	4.23 (3.4)	4.27 (4.4)
Ir	3.84	3.90 (1.5)	3.91 (1.8)	3.93 (2.3)	3.94 (2.6)
Pt	3.92	4.00 (2.0)	4.01 (2.3)	4.04 (3.1)	4.06 (3.5)
Au	4.08	4.18 (2.4)	4.21 (3.2)	4.23 (3.7)	4.26 (4.4)

obtained using BLYP functional. Unfortunately, the same functional strongly underestimates metal cohesivity. The same kind of conflict has been identified for all local and semi-local functionals. PBEsol, PBE, RPBE and BLYP, in this order, improve CO binding energy but deteriorate description of the metal[2].

Orbital-dependent correction schemes have had more promising results. Imposing a penalty on the 2π orbital can lift the site ordering discrepancy [206]. More recently, a totally ab-initio orbital-dependent self-interaction-correction scheme, applicable to any type of functional, has shown excellent improvement on electronic affinities and ionization energies [22].

In parallel, we here want to investigate the effect of non-local correlation.

8.3 VdW-DF CO binding energies

8.3.1 Computational setup

In its current implementation, vdW-DF is based on GGA. The exchange part is unchanged (local + semi-local, i.e. gradient, terms). The correlation is replaced with the LDA local term plus a non-local E_c^{nl} term described in chapter 2:

$$E_{\text{vdW-DF}} = E_{\text{GGA}} - E_{\text{GGA,c}} + E_{\text{LDA,c}} + E_c^{nl}$$

[2]This trend is consistent with the first counter-intuitive observation that if in general GGA tends to underbind and in particular to underestimate surface energies, it usually overestimate chemisorption energies.

VdW-DF was specially developed to be used on top of revPBE-GGA[3] (revPBE-vdW). Comparison of vdW-DF with PBE must then be done by carefully separating contributions from exchange and correlation. To be fully self-consistent, pseudopotentials should be generated and then used with the same functional. However, vdW pseudopotentials were not yet available. In addition, preliminary studies have concluded that the error from using PBE pseudopotentials is negligible. Here, four functionals are compared: PBE, revPBE, PBE-vdW and revPBE-vdW. Extending the study found in [208], 7 metals were considered, using PBE pseudopotentials downloaded from quantum-espresso.org:

Cu: Cu.pbe-d-rrkjus
Rh: Rh.pbe-nd-rrkjus
Pd: Pd.pbe-rrkjus
Ag: Ag.pbe-d-rrkjus
Ir: Ir.pbe-n-rrkjus
Pt: Pt.pbe-nd-rrkjus
Au: Au.pbe-nd-rrkjus

The metal surface is modeled with a 4-layer slab in the [111] direction. A vacuum region of 13 Å is maintained between the slabs. A CO molecule is placed on atop site or fcc site in a $(2 \times \sqrt{3})$ surface unit cell implying 1/4 ML coverage (for atop, see Figs. 8-5 and 8-6). 30 Ry and 250 Ry cutoffs for plane-wave and charge density expansions are used and smearing is done with Fermi-Dirac distribution at 0.01 Ry temperature. The first Brillouin zone is sampled with a $7 \times 7 \times 1$ k-point mesh. Atomic positions of CO and of the first metal layer are fully relaxed.

First, self-consistent results are obtained, in which relaxed positions, charge densities and energies are computed with the same functional. Then, results will be analyzed by means of a perturbative approach.

8.3.2 Self-consistent results

8.3.2.1 Metal lattice constants

Metal equilibrium lattice parameters are calculated by fitting the Birch-Murnaghan isothermal equation of state[4] to energy data (Table 8.1). Calculations are for a pressure of zero Pa (good

[3]RevPBE has the same functional form as PBE; the only difference is in the numerical value of one parameter in the exchange enhancement factor. This functional is not to be confused with RPBE. In this case, the functional form is different in order to respect the Lieb-Oxford criterion locally [207].

[4]An equation of state built upon the experimental fact that the pressure derivative of the bulk modulus is about constant.

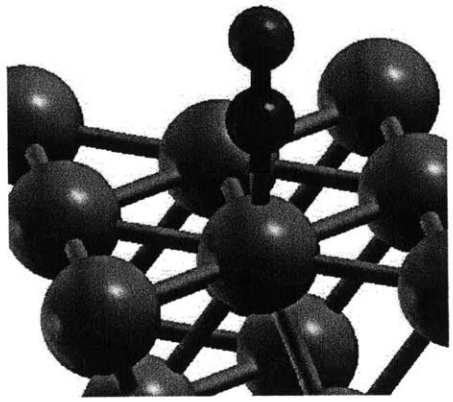

Figure 8-5: Configuration for CO atop adsorption.

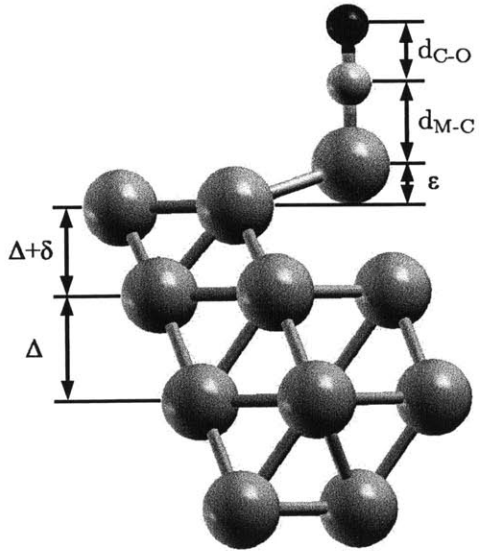

Figure 8-6: Geometric parameters defining atomic positions. Here, CO is adsorbed at the atop site.

Table 8.2: Values of geometric parameters (Å) after full relaxation of the system with two functionals - PBE and revPBE-vdW.

		PBE		revPBE-vdW	
		atop	fcc	atop	fcc
	Δ	2.123		2.165	
	δ	-0.058		-0.045	
Cu	ε	0.126	0.086	0.108	0.091
	d_{M-C}	1.880	1.428	1.922	1.475
	d_{C-O}	1.154	1.178	1.151	1.173
	Δ	2.227		2.254	
	δ	-0.040		-0.040	
Rh	ε	0.183	0.071	0.176	0.073
	d_{M-C}	1.855	1.398	1.874	1.418
	d_{C-O}	1.159	1.188	1.156	1.184
	Δ	2.309		2.342	
	δ	-0.029		-0.023	
Pt	ε	0.182	0.104	0.186	0.101
	d_{M-C}	1.861	1.346	1.883	1.326
	d_{C-O}	1.153	1.189	1.150	1.186

approximation to 1 atm since bulk moduli are on the order of Mbar). DFT energies are extrapolated to 0 K. A comparison is made with experimental values taken from webelements.com. As typically known, PBE tends to slightly underbind the system, resulting in a larger lattice parameter, but the error is within 2%. Using a different exchange with revPBE or a different correlation with PBE-vdW deteriorates the lattice parameter. With revPBE-vdW, the error roughly doubles.

8.3.2.2 Relaxed positions and adsorption energies

CO relaxed positions are reported in Table 8.2. Binding energies are shown in Fig. 8-7, with experimental error bars in orange. The new functional improves on binding energies. In addition, it almost entirely restores the right adsorption site order. On Cu and Rh, atop adsorption becomes preferential. On Pt, atop and fcc adsorptions are degenerate.

8.3.3 Perturbative approach

Equilibrium atomic positions and charge density minimize the total energy. Energy from a new functional can be quickly calculated by directly applying the new functional on the frozen positions and charge density of the previous functional. Error with respect to the fully self-consistent result is of second order in the perturbation. Here, the accuracy of the perturbative

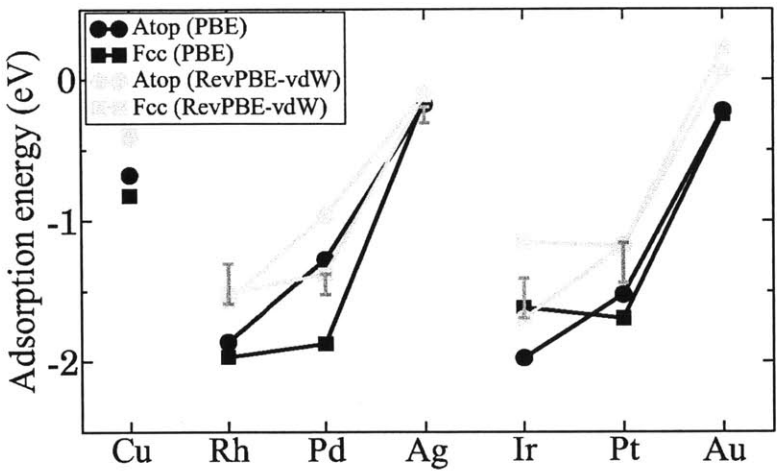

Figure 8-7: CO adsorption energy on late transition metals at atop and fcc sites, from PBE and revPBE-vdW functionals. Experimental error bars are from [199]. Coverage is 0.25 ML.

approach from PBE to revPBE-vdW is carefully examined. Successive approximations are considered, where every time, only one parameter is modified (Table 8.3).

CO adsorption energies on Cu, Rh and Pt are calculated within every scheme, so that approximations inherent to the perturbative approach can be systematically quantified (Table 8.4). Then, energy changes from PBE to revPBE-vdW are compared between fully self-consistent and perturbative treatments (Table 8.5). The perturbative approach gives reasonable estimates of "absolute" binding energy changes (atop and fcc), and is very close to self-consistency for the relative binding energy change (fcc - atop).

8.3.4 Exchange and correlation

As already expressed, the advantage of a perturbative approach is that energy from new functionals can be directly computed on the frozen charge density obtained from a previous functional. Applying revPBE-vdW on the PBE charge density, it becomes easy to separate changes from new exchange and correlation terms (Fig. 8-8). It appears that revPBE exchange (blue) is responsible for most of the improvement in binding energy. Non-local correlation plays an important role in stabilizing atop over fcc adsorption.

Table 8.3: Calculation schemes for the perturbative approach. Only two schemes are fully self-consistent: PBE and revPBE-vdW. In every other case, item in boldface is what differs from the setup above. PBEa and revPBE-vdWd differ only by their energy functional. More precisely, revPBE-vdWd energy is obtained by directly applying vdW-DF to PBEa charge density. The * means that CO charge density and energy in the gas phase are computed with the C-O distance of the adsorbed molecule. This is to facilitate charge transfer analysis upon adsorption.

Calculation setup	Energy functional	Lattice parameter	Atomic positions	Electronic density
PBE	PBE	a_{PBE}	PBE	n^{scf}_{PBE}
PBEa	PBE	a_{PBE}	**PBE***	n^{scf}_{PBEa}
revPBE-vdW	revPBE-vdW	$a_{revPBE\text{-}vdW}$	revPBE-vdW	$n^{scf}_{revPBE\text{-}vdW}$
revPBE-vdWa	revPBE-vdW	$\mathbf{a_{PBE}}$	revPBE-vdW	$n^{scf}_{revPBE\text{-}vdWa}$
revPBE-vdWb	revPBE-vdW	a_{PBE}	**PBE**	$n^{scf}_{revPBE\text{-}vdWb}$
revPBE-vdWc	revPBE-vdW	a_{PBE}	**PBE***	$n^{scf}_{revPBE\text{-}vdWc}$
revPBE-vdWd	revPBE-vdW	a_{PBE}	PBE*	$\mathbf{n^{scf}_{PBEa}}$

Table 8.4: Calculated CO adsorption energies on Cu, Rh, Pt, at atop and fcc sites for all setups described in Table 8.3.

Metal	Site	**PBE**	***PBEa***	**RPB-vdW**	RPB-vdWa	RPB-vdWb	RPB-vdWc	***RPB-vdWd***
Cu	E^{top}_{ads} (eV)	-0.679	-0.733	-0.447	-0.413	-0.353	-0.446	-0.441
	E^{fcc}_{ads} (eV)	-0.824	-0.954	-0.411	-0.395	-0.330	-0.465	-0.459
	$E^{top}_{ads} - E^{fcc}_{ads}$	**0.145**	***0.221***	**-0.036**	-0.018	-0.023	0.019	***0.018***
Rh	E^{top}_{ads} (eV)	-1.862	-1.981	-1.591	-1.570	-1.516	-1.676	-1.618
	E^{fcc}_{ads} (eV)	-1.968	-2.134	-1.535	-1.515	-1.465	-1.649	-1.594
	$E^{top}_{ads} - E^{fcc}_{ads}$	**0.106**	***0.153***	**-0.056**	-0.055	-0.051	-0.027	***-0.024***
Pt	E^{top}_{ads} (eV)	-1.523	-1.617	-1.270	-1.179	-1.117	-1.304	-1.234
	E^{fcc}_{ads} (eV)	-1.692	-1.859	-1.267	-1.184	-1.114	-1.338	-1.263
	$E^{top}_{ads} - E^{fcc}_{ads}$	**0.169**	***0.242***	**-0.003**	0.005	-0.003	0.034	***0.029***

Table 8.5: Correction in the CO adsorption energies upon application of the revPBE-vdW functional. In left column, correction is calculated fully self-consistently, whereas in right column, correction is calculated in a perturbative way.

Metal	Site	$E^{revPBE-vdW} - E^{PBE}$ (eV)	$E^{revPBE-vdW\,d} - E^{PBE\,a}$ (eV)
Cu	atop	0.23	0.29
	fcc	0.41	0.49
	fcc - atop	**0.18**	**0.20**
Rh	atop	0.27	0.36
	fcc	0.43	0.54
	fcc - atop	**0.16**	**0.18**
Pt	atop	0.25	0.38
	fcc	0.42	0.60
	fcc - atop	**0.17**	**0.21**

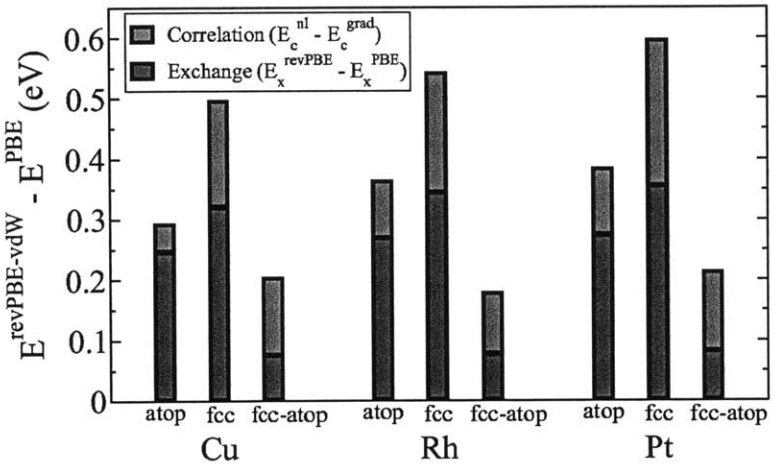

Figure 8-8: Change in CO binding energy from PBE to revPBE-vdW, from exchange and correlation terms.

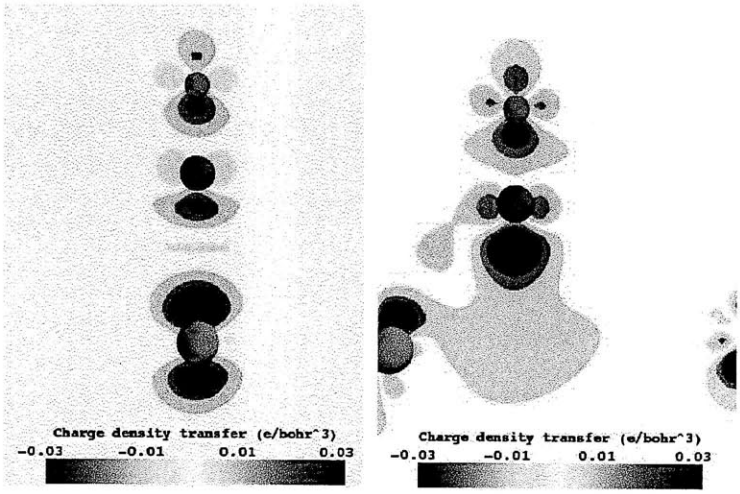

Figure 8-9: Electron charge density transfer upon adsorption at atop (left) and fcc (right) sites.

8.3.5 Charge and energy densities

In order to visualize where changes in exchange and correlation energies occur, electronic charge and energy densities are plotted (Figs. 8-9, 8-10 and 8-11). Examining the correlation energy change on fcc site, we see that destabilization of fcc adsorption comes essentially from giving up the gradient term, rather than specifically capturing non-local effects. Other implementations capturing dispersion forces from RPA, possibly in combination with exact exchange (EXX), have yielded better improvement of both metal properties (the surface energy) and chemisorption energies [209, 210].

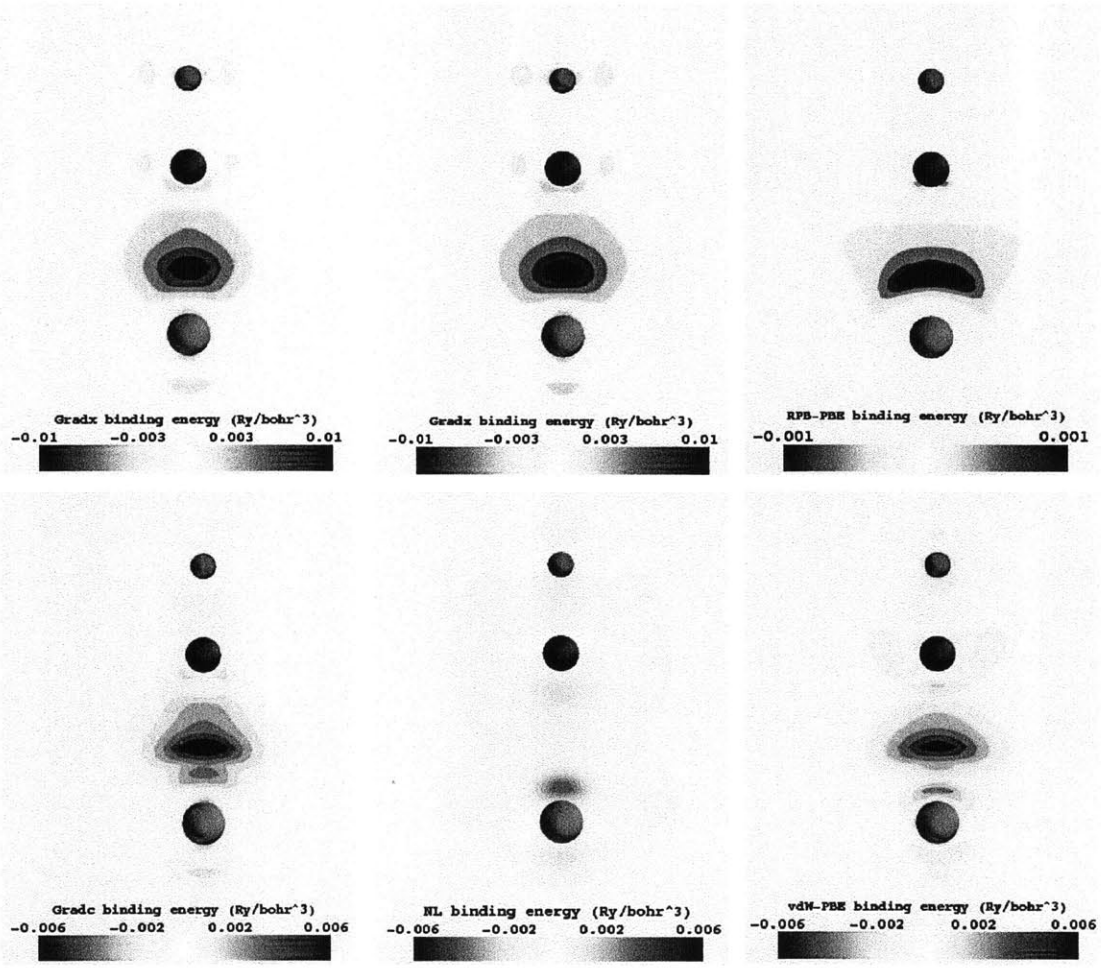

Figure 8-10: Binding energy density with PBE (left), revPBE-vdW (middle) and difference between the two (right), for atop adsorption. Top panels are for exchange, bottom panels are for correlation.

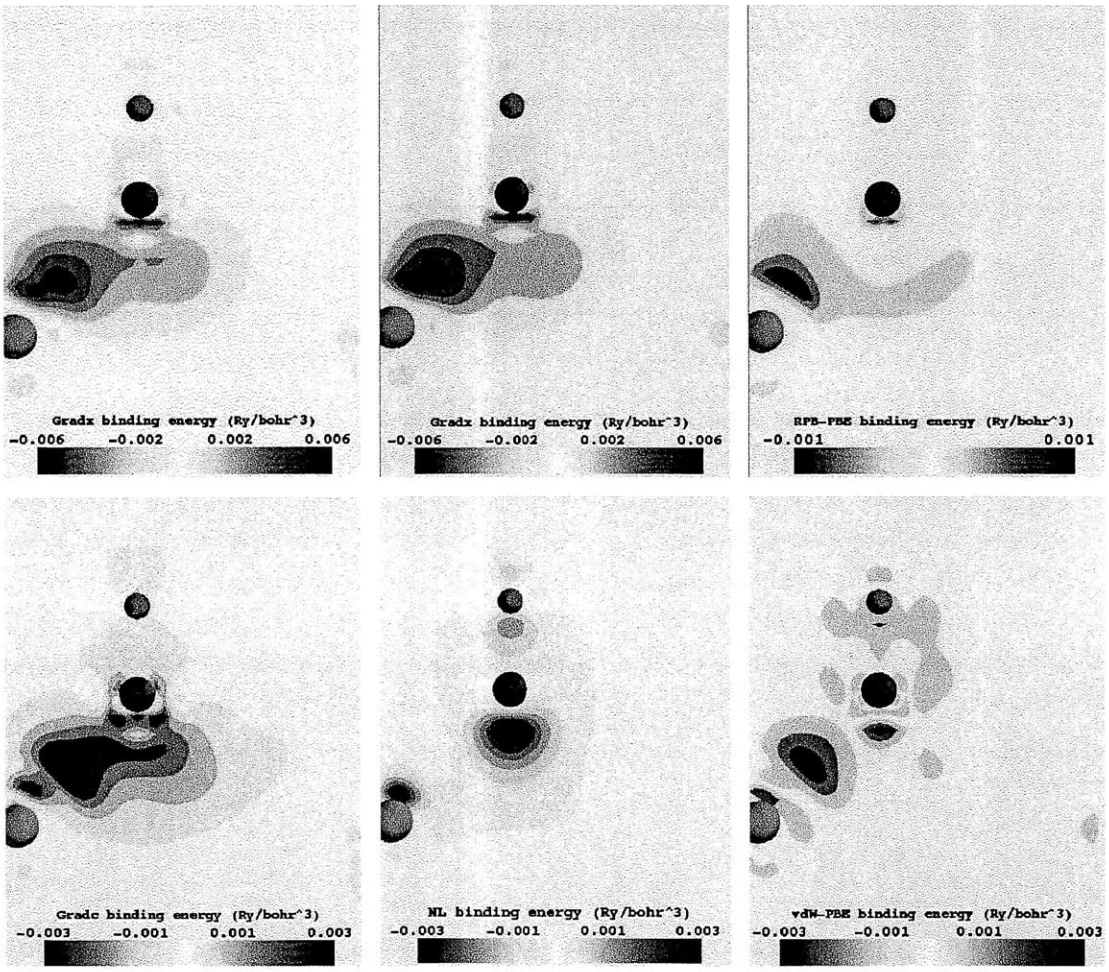

Figure 8-11: Binding energy density with PBE (left), revPBE-vdW (middle) and difference between the two (right), for fcc adsorption. Top panels are for exchange, bottom panels are for correlation.

Chapter 9

Summary and Conclusions

This dissertation is a study of the interdependence between chemical and electrostatic interactions in the electrochemical double layer, and their significance for accurate prediction of reaction kinetics in electrocatalysis. The double layer is in general a region of high complexity, where experimental and theoretical uncertainties tend to hinder rational design of new catalysts. Models for catalytic activity must encompass as many relevant factors as possible but still remain tractable. As part of these models, it is desirable to understand and be able to accurately predict reaction energetics in the region of the electrified double layer.

First, a kinetic model of the oxygen reduction reaction (ORR) on platinum is developed to illustrate that a self-consistent description of kinetics and reactant coverages on the surface can help to propose new mechanisms when energy prediction and experimental uncertainties still prevail. The model incorporates findings of previous first-principles and experimental studies to extract the most relevant reactions on the surface. Additional DFT calculations are performed to get a description of surface energetics vs. coverage. Kinetic equations are written in the framework of transition state theory, and solved self-consistently. Remaining uncertainties on the energetics are included in a sensitivity analysis, and different scenarios are assessed with respect to experimental observables. ORR kinetic limitation is often rationalized in terms of surface poisoning by parallel reactions, particularly water oxidation, and/or as a result of the demanding requirements of Sabatier's principle. The result of the sensitivity analysis is that additional mechanisms may have to be considered, in particular self-poisoning by transient O_2 dissociation in certain regimes. In this case, a guideline for catalyst design could be to hinder O_2 dissociation. Additional work on the experimental side would focus on closer characterization of the surface state possibly modified by O_2 reactant.

One notorious difficulty of catalytic studies is the so-called pressure gap problem: many surface characterization techniques are conducted in vacuo, while working catalysts operate in

dense environments, for instance liquids. To what extent are some critical properties affected in the process? In a similar way, application of a potential bias on electrocatalytic surfaces a priori modifies the structure of the double layer, with no direct way to probe local variations. In order to refine our understanding of bias effects in the double layer, a correction code is applied to plane-wave DFT techniques so that isolated charged systems can be accurately described. In particular, an electrochemical half-cell under potential control is realistically simulated by means of a metal slab with variable explicit charge screened by ions in solution.

The scheme is first used to elucidate the nature of the stretching frequency shift of CO on Pt(111) as a function of electrode potential. Specifically, the question is to decide if vibrational shifts are of chemical nature, as rationalized by donation and back-donation mechanisms, or rather electrostatic, i.e. involving only molecular dipoles, like in a Stark effect. It is concluded that the Stark effect interpretation is correct, and more generally, that electrochemistry on metal surfaces may often be correctly and conveniently described in terms of perturbation theory. However, the concept of molecule metallization is emphasized, by which it is understood that the notion of an individual CO molecule vanishes upon chemisorption, and the relevant dipole for Stark effect interpretation is the one of the molecule-on-the-surface system as a whole.

The importance of surface dipole is further illustrated in the study of hydrogen under-potential deposition on platinum as a function of pH. The amount of free charges on the surface of the reversible hydrogen electrode (RHE) is a function of pH. It is shown that modification of the surface dipole by hydrogen electrosorption couples with the surface charge to make the adsorbant chemical potential pH-dependent. This observation is related to the concept of electrosorption valency, which becomes computable by application of the electrostatic correction code. Furthermore, the octahedric-to-cubic nanoparticle shape transition resulting from hydrogen adsorption upon cathodic sweep is then predicted to be more pronounced in alkaline media. This observation is of importance for catalytic purposes, as it is well established that surface activity is a function of crystalline orientation. This effect is exemplified for the case of hydrogen adsorption because comparison with accurate experimental isotherms is available; however, the use of strongly electronegative adsorbants, such as oxygen or chlorine, could have even larger effects.

The relation between surface charge and electric field in the double layer is expressed by the interface capacitance, which is itself a function of water permittivity. Measuring the double layer capacitance is not straightforward, owing to hiding effects from faradaic surface currents in many potential windows. However, increasing knowledge has been gained in particular from the application of impedance spectroscopy techniques. Here, the purpose is to assess the

ability of first-principles methods to reproduce permittivity and dielectric saturation measurements. The electrostatic correction scheme is applied to compute the molecular dipole of water in the condensed phase of ice Ih. Then, Monte-Carlo techniques are performed to simulate the statistics of proton arrangement. The permittivity of ice predicted by DFT is larger than from experiment. Elucidation of the discrepancy is related to the question of the behavior of ice at very low temperature, where transition to a ferroelectric state has still to be completely established. In spite of these uncertainties, dielectric saturation effects are believed to be qualitatively captured by our model. Their influence on reaction kinetics in the double layer from the Frumkin effect is assessed. The impact is rather moderate with at most a factor of 3 in exchange current predictions.

Finally, DFT occasional errors in chemisorption energies remain an important drawback for heterogeneous catalysis studies. In this work, the vdW-DF functional for inclusion of long-range, dispersion interactions is tested on the prediction of CO adsorption on transition metals. It is observed that improvement on binding energies and adsorption site ordering comes at the expense of the correct description of metal energetics, suggesting the need for alternative schemes in this case.

In conclusion, the purpose of this work is to help the design of electrocatalysts by providing a framework to assess chemical and electrostatic contributions to surface kinetics. Traditional concepts of electrochemistry are discussed and connected to quantities computable from appropriate first-principles schemes to extract rigorous and, if possible, simple rationales. At the same time, models with sufficient flexibility are developed to adapt to the characteristic complexity and uncertainties of the surface and double layer structure.

Appendix A

Constants and Units

A.1 De Broglie's equation

$$\lambda = \frac{h}{p}$$

with **Planck's constant** $h = 6.62607 \times 10^{-34}$ Js.

- For a photon:

$$E = \frac{hc}{\lambda}$$

with **speed of light in vacuum** $c = 299\ 792\ 458$ ms^{-1}. Equivalent ways to report photon position in the middle of the visible electromagnetic spectrum:

Energy = 2.0664 eV
Frequency = 0.50×10^{15} Hz
Wave-length = 600 nm
Inverse of wave-length = $16,667$ cm^{-1}

- For a massive particle:

$$E = \frac{\hbar^2 k^2}{2m}$$

For comparison, 1 Å wavelength implies $E(\text{X-ray}) = 10$ keV, $E(\text{e}^-) = 200$ eV.

A.2 Bohr units

With q_e being the absolute charge of the electron[1], we write[2] $e^2 = \frac{q_e^2}{4\pi\varepsilon_0}$, where:

$q_e = 1.60218 \times 10^{-19}$ C
$\varepsilon_0 = 8.85419 \times 10^{-12}$ $C^2N^{-1}m^{-2}$ (permittivity of free space)

Units for energy and length are the Hartree and Bohr radius:

$$E_a = \frac{m_e e^4}{\hbar^2} = 27.2 \text{ eV}$$

$$a_0 = \frac{\hbar^2}{m_e e^2} = 0.529 \text{ Å}$$

The strength of the electromagnetic force is characterized by the fine-structure constant:

$$\alpha = \frac{e^2}{\hbar c} \simeq \frac{1}{137}$$

Particle masses:

$m_e = 9.1094 \times 10^{-31}$ kg $\rightarrow m_e c^2 = 0.511$ MeV
$m_p = 1.67262 \times 10^{-27}$ kg $\rightarrow m_p c^2 = 938.27$ MeV
$m_n = 1.67493 \times 10^{-27}$ kg $\rightarrow m_n c^2 = 939.57$ MeV

A.3 Statistics

Boltzmann constant $k = 1.38065 \times 10^{-23}$ JK^{-1}:

- At 298 K, $kT = 0.02568$ eV
- $\frac{kT}{h} = 6.21 \times 10^{12}$ Hz

Avogadro's number $N_A = 6.02214 \times 10^{23}$
Faraday's constant $F = 96485.3$ C

[1] All equations in the dissertation do use the usual convention that the electron is negatively charged.

[2] This is to simplify these equations in SI units. However, everywhere else in the text, it is simply e which denotes the absolute electronic charge.

A.4 Conversions

1 eV = 96.485 kJ/mol

1 kcal/mol = 4.184 kJ/mol

1 D = 3.33564×10^{-30} Cm

On Pt(111), a surface charge of 10 μC/cm^2 corresponds to $\frac{4.34}{100}e$ per atom.

For Pt(111), a surface energy of 1 J/m^2 corresponds to 0.434 eV/atom.

Appendix B

Chemistry on transition metals

B.1 Periodic table of the elements

Understanding and prediction of the arrangement and electronic structure of atoms in the periodic table is a good example of how a simple model can then be refined by perturbative approaches.

B.1.1 Hydrogenoid atoms

Electronic eigenstates are labeled (n, l, m_l). Energy is only a function of n (defining the shell: K, L, M, etc.):

$$E_n = -13.6\frac{Z^2}{n^2}\ \text{eV}$$

and the radial function has a factor in $\exp\left(-\frac{Zr}{na_0}\right)$. When l increases inside a shell, more nodes appear in the angular part of the orbital, which is compensated by fewer nodes in the radial part.

B.1.2 Multi-electron atoms

First, a mean-field approach is considered. Each electron feels an attraction from the nucleus, screened by the average charge of the other electrons, which is assumed to be spherical. Therefore, they occupy hydrogen-like orbitals with the same labeling.

However, the degeneracy in l is now broken. For instance, in a given shell, s orbitals are lower in energy than p orbitals (they have a radial part which is less subject to screening).

Moreover, as the atomic number increases, the partial efficiency of intra-shell screening results in a general trend of increasing electronegativity when moving towards the top right corner of the periodic table (not true for late transition metals).

B.1.3 Hund's rules

Additional corrections lift more degeneracies. Hund's rules are used to find the most stable electronic structure of an atom:

> **Spin** - When filling a subshell (n,l), electrons occupy the maximum number of spherical harmonics ($2l+1$ values of m_l) with their spins in the same direction. S (total spin angular momentum) is maximized to enjoy the exchange energy as much as possible[1].
>
> **Dynamic structure** - For a given S, the total orbital angular momentum L is maximized. Electrons rotating in the same direction are less often in "close contact", thus lowering the interaction energy.
>
> **Spin-orbit coupling** - If the subshell is less than half-filled, the total angular momentum $J = S+L$ should be minimum. If the subshell is more than half-filled, it should be maximum.

These rules lead to determination of the spectroscopic term ${}^{2S+1}L_J$ of the stable configuration. They involve summation of angular momenta. As a short reminder, when adding angular momenta, $\hat{J} = \hat{J}_1 + \hat{J}_2$, in a tensorial product vector space, if starting from states of quantum numbers[2] j_1 and j_2, states with quantum numbers anywhere between $|j_1 - j_2|$ and $j_1 + j_2$ are obtained. Exact formulas of eigenstates of $\hat{J}^2$ in terms of eigenstates of $\hat{J}_1^2$ and $\hat{J}_2^2$ are obtained by means of Clebsch-Gordan coefficients. In the case of electrons, when playing with S and L, some combinations are not possible due to Pauli exclusion principle.
Example: The spectroscopic term of carbon is ${}^3P_0$.

B.2 Adsorption on transition metals

B.2.1 Effect of electronic structure

The late transition metals region is rich in idiosyncratic trends. An electronegativity trend was mentioned previously for s and p blocks. For instance, carbon is more electronegative, form shorter and stronger bonds (higher cohesive energy) than silicon.

[1] This first Hund's rule is important. If O_2 was preferentially in a singlet state rather than a triplet state, the carbon monoxide oxidation reaction would occur without the need for a catalyst. Also, life would not exist.

[2] meaning, for example, that for any state ϕ of the first space: $\hat{J}_1^2\phi = j_1(j_1+1)\hbar^2\phi$

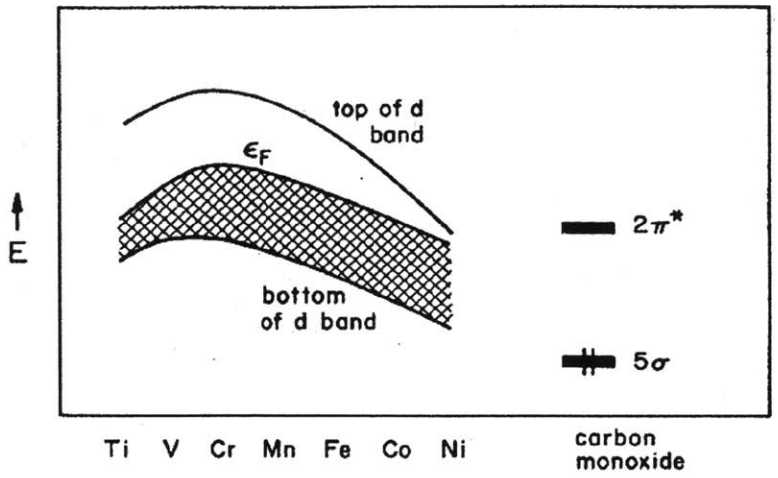

Figure B-1: Trends in electronic structure of $3d$ metals (reproduced from [211])

By contrast, in the late transition block, strong electronegativity and strong cohesive energy (but large lattice parameter) are for the $5d$ noble metal, namely gold.

For the electronic structure of transition metals, it is good to have in mind the simple picture emphasized by Hoffman (Fig. B-1). Effect of an increasing Z is to attract and contract orbitals, make the d-band deeper and narrower. In parallel, more filling occurs, with the net effect of a lower Fermi level but a wider occupied d-band. Moving down the periodic table, orbitals are more extended, and overlaps increase, with the effect of stretching the bands. Some chemical trends can be predicted. Early transition metals are better at breaking up the CO bond, because a higher Fermi level implies increased occupation of the antibonding LUMO of CO. Late transition metals bind CO molecularly. Of great interest is the simple predictor of Hammer and Nørskov for binding energies: a shorter distance of the d-band center to the Fermi level tends to make the metal more reactive [44]. This is because, in this case, hybridization with orbitals of the molecule produce an antibonding state that will lie more easily above the Fermi level, thus resulting in a stronger energy lowering. To say that gold is noble encompasses a set of properties [212]: strong electronegativity (resistance to corrosion), strong cohesivity (mechanical stability), and a low affinity for adsorbants. This last property is qualitatively explained by Hammer-Nørskov predictor: a wide d-band and an important filling.

To the right of gold, and for different reasons, note the very low electronegativities of zinc and aluminum, implying low half-cell potentials and poor thermodynamic resistance to corro-

sion. However, formation of protective oxide layers provide kinetic corrosion resistance.

B.2.2 Coordination and size effects

Nanoparticle chemistry is a function of size. For instance, the lattice parameter of a Pt particle of 30 nm is 3.9 Å and for a particle of 10 nm, it is 3.4 Å. Metallicity of the particle may be affected at very small sizes. Gold becomes active when it is in the form of nanoparticles [213, 214].

B.2.3 Coadsorption

In the case of coadsorption, lateral interactions may originate from direct overlap of wave functions, shift of d-electrons, dipole interactions, metal bond order modification, etc.

An example is coadsorption of CO and potassium on transition metal surfaces. Adsorption of electropositive potassium enhances the bond between the molecule and the metal and promotes CO dissociation at sufficiently high temperatures.

Appendix C

Spectroscopy and Surface Science Techniques

Surface science techniques mentioned in the main text are here briefly described. Most information is from [215]. For applications in catalysis, surface sensitive techniques, involving low-energy electrons, ions, etc., are important. The inherent disadvantage of small mean free paths is that measurements must be carried out in vacuo.

AFM - Atomic force microscopy is based on the small forces between a sharp tip and atoms on the surface. The tip is mounted on a flexible arm, called cantilever, and is positioned at a subnanometer distance from the surface. The deflection of the scanning tip can be measured with a laser and photodetectors. This technique can be used even if the surface is not conducting (e.g. an oxide). A variant is Kelvin probe force microscopy, and allows determination of the surface work function.

AES - Auger electron spectroscopy. In photoelectron spectroscopy (see XPS), peaks are observed in addition to the photoelectron peaks. Indeed, the atom from which the photoelectron is ejected is a highly excited ion, with a hole in one of its inner shells. Relaxation of the ion ejects an Auger electron with fixed kinetic energy, which may however be reported on the binding energy scale of the photoelectron spectrum. Auger peaks can be detected by measuring the spectrum at two different X-ray energies. Only Auger peaks will shift on the binding energy scale. This is the main reason why X-ray sources often contain a dual anode of Mg and Al.

In a specific Auger spectroscopy experiment, a beam of energetic (2-5 keV) electrons create the initial core holes. Auger electrons are labeled with the terminology commonly used in X-ray spectroscopy. For instance, a KLM peak is for an initial core hole in the K shell, filled by an electron from the L shell, and ejecting an Auger electron from the M shell.

EELS - Electron energy loss spectroscopy. Low energy electrons fall on the surface and excite lattice and molecular vibrations. The energy spectrum of scattered electrons shows how much energy has been lost to vibrations. Using electrons requires ultra-high vacuum and is preferably done on flat surfaces of single crystals. When IR and Raman spectroscopy are limited to vibrations in which a dipole moment or the molecular polarizability change, EELS detects all vibrations.

EXAFS - NEXAFS (XANES) - Extended X-ray absorption fine structure. Like XPS, this technique is based on the absorption of X-rays and the creation of photoelectrons, but then looks at how electrons are scattered by neighboring atoms, as shown by interferences in the spectrum. The technique yields detailed information on the distance, number and type of neighbors. The interference pattern just above the edge (when electrons start being ejected) comes from electrons with low kinetic energy, interacting with valence electrons. This near-edge range in the spectrum is referred to as NEXAFS or XANES.

IR - Infrared spectroscopy. Measurements on supported catalysts in diffuse reflection and transmission modes are, in practice, limited to frequencies above those where the support absorbs (below about 1250 cm^{-1}). IR can also provide information on bond orientation.

LEED - Low-energy electron diffraction spectroscopy. It is the surface analogue of X-ray diffraction. Low energy electrons do not penetrate far into the material. Therefore, elastically reflected electrons carry only information on the outermost layers of the surface. Electrons of energy close to the minimum of mean-free path have a wavelength comparable to the distance between atoms in a lattice (see XPS). Back-scattered electrons form a pattern of spots on a fluorescent screen - photographed by a CCD camera, from which the symmetry and structure of the surface may be determined.

LEIS - Low energy ion scattering. A beam of noble gas ions with energy of a few keV scatters elastically from a solid surface. Total energy and momentum are conserved so that the mass of the collision target can be found. 1-keV He ions have a neutralization probability of about 99% on passing through one layer of substrate atoms. Hence, the majority of ions reaching the detector have scattered off the outermost layer. This is therefore a highly surface sensitive technique. However, there is currently no simple theory to adequately describe the scattering cross section and the neutralization probability.

NMR - Nuclear magnetic resonance. An effect whereby magnetic nuclei in a magnetic field

absorb and re-emit electromagnetic energy. This energy is at a specific resonance frequency which depends on the strength of the magnetic field and other factors. This allows the observation of specific quantum mechanical magnetic properties of an atomic nucleus. All stable isotopes that contain an odd number of protons and/or neutrons have an intrinsic magnetic moment, while all nuclides with even numbers of both have spin 0. The most commonly used nuclei are ^{1}H and ^{13}C.

Raman spectroscopy - While in infrared spectroscopy, a molecule absorbs photons with the frequency of its vibrations, Raman spectroscopy is based on the inelastic scattering of photons, giving rise to Stokes and anti-Stokes bands in the spectrum. A vibration is Raman active if it changes the polarizability of the molecule. For instance, stretching vibrations of H_2 (4160.2 cm^{-1}), N_2 (2330.7 cm^{-1}) and O_2 (1554.7 cm^{-1}) are observed in Raman spectroscopy but not in infrared spectroscopy. There have been recent developments in UV Raman spectroscopy.

SFG - Sum frequency generation. A specialty in vibrational spectroscopy that probes adsorbates at interfaces both in real-time and in situ. A typical setup contains a light source - a Nd:YAG laser - emitting photons at a wavelength of 1064 nm. The beam is split: one part is frequency doubled using a KDP crystal (KH_2PO_4), generating second-harmonics at 532 nm in the green; the second part falls on an optical parametric amplification crystal (e.g. $LiNbO_3$, a non-linear, uni-directional material), which is tunable in the infrared region by changing its direction. The sum of two scattered photons from each frequency produces a photon in the blue region. Sum frequency generation cannot occur in centrosymmetric media, making it a surface sensitive technique. Absorption of infrared light and scattering of visible light are involved, implying that selection rules include those of both infrared and Raman spectroscopies.

SIMS - Secondary ion mass spectroscopy. By far the most sensitive surface technique, but it is hard to quantify. When a surface is exposed to a beam of ions (Ar^+, 0.5-5 keV), energy deposited in the surface may stimulate ejection of atoms and ions. Ions are detected directly with a quadrupole mass spectrometer. This is usually a destructive technique.

STM - Scanning tunneling microscopy. A sharp tip is brought close to the surface and a low voltage bias is applied between the sample and the tip. The tip is usually made of tungsten, unless less reactive Pt is required for ambient conditions. What is depicted in an STM experiment is the density of states around the Fermi level. The technique can be applied in situ (even in liquids), but only works on well-defined, planar, and conducting surfaces such as metals and semiconductors, but not on oxide-supported catalysts (unless the oxide part is a thin film).

STM has been successfully applied to distinguish between different adsorbate structures which are very close in energy. The STM profile is compared with the density of states at the Fermi level computed by DFT. This is how the detailed structure of water hexamers on Pd was identified [156].

TEM - Transmission electron microscopy. An electron beam of high energy impinges on the sample. As the beam attenuation depends on the density and thickness, transmitted electrons form a two-dimensional projection of the sample mass, subsequently magnified by electron optics to produce a so-called bright-field image. The dark-field image is obtained from diffracted electron. Typical operating conditions of a TEM instrument are 100 to 200 keV electrons, 10^{-6} mbar vacuum, 0.3 nm resolution, and a magnification of 3×10^5 to 10^6.

UPS - Ultraviolet photoelectron spectroscopy. Most frequent UV sources are helium discharge lamps, which generate He I light at 21.2 eV and He II light at 40.8 eV. At these low exciting energies, photoemission is limited to valence electrons. Hence, UPS is particularly suited to probe bonding in metals, in molecules and in adsorbed species. The spectrum measured from a metal extends from electrons at the Fermi level (*d* metals have a high density of states at the Fermi level) down to electrons that have just enough energy to escape. The work function is directly computable from the spectrum width.

XPS - X-ray photoelectron spectroscopy. Yields information about elemental composition and the oxidation state of elements and electronegativity of ligands. It is based on the photoelectric effect, and the kinetic energy of ejected electrons is measured. Common X-ray sources are MgKα ($h\nu$ = 1253.6 eV) and AlKα ($h\nu$ = 1486.3 eV), inducing kinetic energies of photoelectrons in the 0-1 keV range. Electrons with these energies do not travel more than a few atomic distances, making XPS a surface sensitive technique. An optimum resolution of 5 Å is achieved for electron kinetic energies in the 50-200 eV range. Photoelectron peaks are labeled according to the quantum numbers of the level from which electrons are ejected. Because of the spin, each level with $l \geq 1$ has two sublevels, $j = l \pm 1/2$ (with multiplicity $2j+1$), separated by the spin-orbit coupling splitting energy. For instance, Rh 3d level ($l = 2$) gives two photoemission peaks, $3d_{5/2}$ and $3d_{3/2}$, 307 and 312 eV respectively. By measuring the peak ratio from support and particles, one can determine the catalyst dispersion - if other techniques such as electron microscopy or hydrogen chemisorption are not available.

XRD - X-ray diffraction spectroscopy. Used to identify crystalline phases by elastic scattering of X-ray photons. Crystallite sizes can be inferred from the line broadening in the interference

pattern. One great advantage of this technique is the penetrating power of X-rays, so that XRD can be used to study catalysts under realistic conditions in specially designed in situ reactors. Use of synchrotron radiations as a source for XRD offers opportunity for short collection times and high radiation intensity. Note that the surface, where catalytic reactions occur, is itself invisible in standard XRD.

Appendix D

Computation

D.1 Plane-wave DFT

D.1.1 Reciprocal space

From chapter 2, it is reminded that the system to solve to determine the ground-state electronic structure of the system is:

$$\left[-\frac{\nabla^2}{2}+v_{\text{eff}}(\mathbf{r})\right]\Psi_i=\varepsilon_i\Psi_i \tag{D.1}$$

This problem is put into matrix form by expanding the unknown wave-functions on a basis set. Working in periodic-boundary conditions leads naturally to the use of plane-waves, a choice motivated by convenience and by the performance of fast Fourier transform techniques - such as the Fastest Fourier Transform in the West (FFTW) - which scale in $N\log N$. Specifically, Bloch's theorem states that eigenfunctions of an electron placed in a periodic potential have the form:

$$\Psi_{n\mathbf{k}}(\mathbf{r})=e^{i\mathbf{k}\cdot\mathbf{r}}u_{n\mathbf{k}}(\mathbf{r})$$

where $u_{n\mathbf{k}}(\mathbf{r})$ is a function with the periodicity of the potential. Eigenvalues are obtained for $\mathbf{k}$ restricted to the first Brillouin zone of the crystal. Inserting this form into Eq. (D.1) and expanding $u_{n\mathbf{k}}(\mathbf{r})$ on the plane-wave basis set with coefficients $c_{n,\mathbf{k}+\mathbf{G}}$, the secular equation to solve is obtained (in hartrees):

$$\sum_{\mathbf{G}'}\left[\frac{1}{2}|\mathbf{k}+\mathbf{G}|^2\delta_{\mathbf{G}\mathbf{G}'}+V_{\text{ion}}(\mathbf{G}-\mathbf{G}')+V_{xc}(\mathbf{G}-\mathbf{G}')+V_H(\mathbf{G}-\mathbf{G}')\right]\times c_{n,\mathbf{k}+\mathbf{G}'}=\varepsilon_{n\mathbf{k}}c_{n,\mathbf{k}+\mathbf{G}}$$

Sampling of the first Brillouin zone is achieved by creation of a sufficiently dense k-point mesh [216].

D.1.2 Pseudopotentials

The expansion of wave-functions on the plane-wave basis set has a cutoff. The kinetic energy - taken to be the one of an electron - corresponding to the maximum wave-vector ($E = \frac{\hbar^2 G^2}{2m_e}$) controls the spatial resolution. To give an idea, for the wave-length of an electron to be on the order of 1 Å, the energy required is 200 eV. The number of g-vectors in a given direction depends on the size of the unit cell, since the smallest g-vector has a wave-length of that size. The total number of g-vectors combined with the number of k-points and the number of electrons (controlling the number of wave-functions calculated at each k-point) determines the required memory (e.g., a $100 \times 100 \times 100$ g-vector grid induces a factor around 1 MB).

The chemical properties of an atom come mostly from its valence electrons. Atomic pseudopotentials have been developed as a means to replace the potential created by the nucleus and core electrons. The benefit is to avoid computation of core electron wave-functions, which, furthermore, have a strong spatial variation close to their center. Valence wavefunctions computed with the pseudopotentials are identical to the real, all-electron ones, beyond a certain distance from the nucleus, called cutoff radius[1], which is enough for chemical purposes, since hybridization occurs far enough from the nucleus. Matching of the derivative at the cutoff radius is also ensured for preserving scattering properties. Inside the cutoff radius, the wave-function is smoother, allowing the use of smaller plane-wave energy cutoffs. Finally, norm-conserving pseudopotentials guarantee that the wave-function total charge density within the cutoff radius is also preserved, an important condition for charge conservation and correct application of energy functionals. However, for wavefunctions with no radial node, the norm-conserving condition precludes sufficient smoothing close to the center. This is, for instance, the case of oxygen $2p$ orbitals. Ultrasoft pseudopotentials were developed by Vanderbilt to overcome this problem [217]. The scheme leads to pseudopotentials that force smoothness of their eigenfunctions, sacrificing norm conservation. This is then repaired by the use of augmentation charges. Specifically, the ultrasoft pseudopotential is made of a local part $V_{\text{loc}}^{\text{ion}}$ of spherical symmetry and a non-local part that involves projectors $|\beta_i\rangle\langle\beta_j|$ on functions of definite angular momenta (typically, a couple of them at different energies for each relevant l, to ensure good transferability) and vanishing beyond the cutoff radius. Eigenfunctions in the ultrasoft pseudopotential

[1]For atomic wavefunctions, this is achieved when building the pseudopotential. A reference electronic configuration is chosen. In a more complex chemical environment, it is a consequence of transferability, which must also be part of the pseudopotential construction.

formalism are not orthonormal, implying definition of an overlap operator:

$$S = 1 + \sum_{ij} Q_{ij} \left|\beta_i\right\rangle\left\langle\beta_j\right|$$

where charges Q_{ij} are computed when creating the pseudopotential. Resolution of Kohn-Sham equations in this formalism introduces a dependence of the non-local part on the charge density. The equation to solve becomes:

$$(T + V_{\text{loc}} + V_{NL} - \varepsilon_{n\mathbf{k}} S)\,\Psi_{n\mathbf{k}} = 0$$

where $V_{\text{loc}} = V_{\text{loc}}^{\text{ion}} + V_{\text{Hxc}}$ and:

$$V_{NL} = \sum_{ij} D_{ij} \left|\beta_i\right\rangle\left\langle\beta_j\right|$$

in which $D_{ij} = D_{ij}^{\text{ion}} + D_{ij}^{\text{Hxc}}$. D_{ij}^{ion} come with the pseudopotential and D_{ij}^{Hxc} depend on the charge density through the Hartree-exchange-correlation potential, implying that part of the self-consistent process is to update the pseudopotential.

D.1.3 Diagonalization

Resolution of the secular equation is achieved by means of iterative techniques. Eigenvalues are obtained as the Lagrange multipliers related to constraints on orthonormality of the eigenfunctions. An example is the conjugate-gradient technique, improving on the steepest descent algorithm. Optimization along a conjugate direction ensures optimization within the entire space defined by previous search directions. Overall cost of DFT algorithms is in $O(N^3)$ in general but often achieves $O(N^2 \log N)$-$O(N)$.

D.2 Hardware

Most of DFT calculations in this work have been completed on our local cluster (Zahir), constituted by one 2U master node, two gigabit switches and 50 twin 1U compute nodes with specifications in Fig. D-1.

Software includes Intel compilers icc, ifort, MPI wrappers mpicc, mpif90, Intel MKL 10.1 libraries, and espresso-3.2.3, espresso-4.0.5.

	Quantity	**CPU (cores/threads)**	**Speed (GHz)**	**RAM (Gb)**	**HardDisk (Gb)**
Master node	1	E5520 (8/16)	2.27	12	1 Tb RAID (/dev/sdb) 2 Tb (/dev/sda)
Compute-0-0.. compute-0-37	38	E5520 (8/16)	2.27	12	2x 250 Gb
Compute-0-38.. compute-0-49	12	E5520 (8/16)	2.27	48	2x 500 Gb

Figure D-1: Specifications of our cluster Zahir.

Bibliography

[1] D.J.C. MacKay, "Sustainable energy - without the hot air", UIT Cambridge, 2009. 19

[2] P. Baer and M. Mastrandrea, "High stakes: designing emissions pathways to reduce the risk of dangerous climate change", Institute for Public Policy Research, London, 2006. Available at www.ippr.org. 19

[3] M.W. Kanan and D.G. Nocera, Science **321**, 1072 (2008). 22

[4] D.J. Bradwell, "Liquid metal batteries: ambipolar electrolysis and alkaline earth electroalloying cells", MIT PhD thesis, 2011. 23

[5] J. Kohanoff and N.I Gidopoulos, "Handbook of molecular physics and quantum chemistry", Wiley, 2003, vol. 2, part 5, chap. 26. 30

[6] P. Hohenberg and W. Kohn, Phys. Rev. **136**, B864 (1964). 32

[7] W. Kohn and L.J. Sham, Phys. Rev. **140**, A1133 (1965). 33

[8] D.M. Ceperley and B.J. Alder, Phys. Rev. Lett. **45**, 566 (1980). 34

[9] J.P. Perdew and A. Zunger, Phys. Rev. B **23**, 5048 (1981). 34

[10] J.P. Perdew and Y. Wang, Phys. Rev. B **45**, 13244 (1991). 35

[11] J.P. Perdew, K. Burke and M. Ernzerhof, Phys. Rev. Lett. **78**, 1396 (1981). 35

[12] M. Dion, H. Rydberg, E. Schröder, D.C. Langreth and B.I. Lundqvist, Phys. Rev. Lett. **92**, 246401 (2004). 35

[13] R. Kubo, Rep. Prog. Phys. **29**, 255 (1966). 36

[14] G. Giuliani and G. Vignale, "Quantum theory of the electron liquid", Cambridge University Press, 2005, chap. 3.

[15] R.M. Martin, "Electronic structure: basic theory and practical methods", Cambridge University Press, 2005, app. D. 36

[16] G. Román-Pérez and J.M. Soler, Phys. Rev. Lett. **103**, 096102 (2009). 38

[17] T. Thonhauser, V.R. Cooper, S. Li, A. Puzder, P. Hyldgaard and D.C. Langreth, Phys. Rev. B **76**, 125112 (2007). 38

[18] D. C. Langreth et al., J. Phys.: Condens. Matter **21**, 084203 (2009). 38

[19] M. Fuchs and X. Gonze, Phys. Rev. B **65**, 235109 (2002). 38

[20] O.A. Vydrov and T. Van Voorhis, Phys. Rev. Lett. **103**, 063004 (2009). 38

[21] H.-V. Nguyen and S. de Gironcoli, Phys. Rev. B **79**, 205114 (2009). 38

[22] I. Dabo, A. Ferretti, N. Poilvert, Y. Li, N. Marzari and M. Cococcioni, Phys. Rev. B **82**, 115121 (2010). 38, 139

[23] H.A. Gasteiger and N.M. Marković, Science **324**, 48 (2009). 39

[24] I.E. Maxwell, Stud. Surf. Sci. Catal. **101**, 1 (1996). 42

[25] W. Prandtl, J. Chem. Ed. **27**, 176 (1950). 41

[26] H.G. Petrow and R.J. Allen, US Patent No. 4,044,193 (1977). 42

[27] I.D. Raistrick, "Diaphragms, separators and ion exchange membranes" edited by J.W. van Zee, R.E. White, K. Kinoshita et al., Pennington: The Electrochemical Society Softbound Proceedings Series, 1986, PV 86-13. 42

[28] M.S. Wilson and S. Gottesfeld, J. Electrochem. Soc. **139**, L28 (1992). 42

[29] M.S. Wilson, US Patents Nos. 5,211,984 and 5,234,777 (1993). 42

[30] T.E. Springer, M.S. Wilson and S. Gottesfeld, J. Electrochem. Soc. **140**, 3513 (1993). 42

[31] H.A. Gasteiger, S.S. Kocha, B. Sompalli and F.T. Wagner, Appl. Cat. B: Env. **56**, 9 (2005). 42

[32] J.H. Simpson and H.Y. Carr, Phys. Rev. **111**, 1201 (1958). 42

[33] E.F. Holby, W. Sheng, Y. Shao-Horn and D. Morgan, En. Environ. Sci. **2**, 865 (2009). 43

[34] Y. Shao-Horn, W.C. Sheng, S. Chen, P.J. Ferreira, E.F. Holby and D. Morgan, Top Catal. **46**, 285 (2007). 43

[35] L. Tang, B. Han, K. Persson, C. Friesen, T. He, K. Sieradzki and G. Ceder, J. Am. Chem. Soc. **132** (2), 596 (2010). 43

[36] A. Kuzume, E. Herrero and J.M. Feliu, J. Electroanal. Chem. **599**, 333 (2007). 44

[37] M.D. Maciá, J.M. Campiña, E. Herrero and J.M. Feliu, J. Electroanal. Chem. **564**, 141 (2004). 44

[38] N.M. Marković and P.N. Ross, Surf. Sc. Rep. **45**, 117 (2002). 44, 89

[39] S. Gottesfeld, "Fuel cell catalysis - A surface science approach", Wiley, 2009, Chap. 1. 44, 48, 49

[40] J. Greeley, J. Rossmeisl, A. Hellman and J.K Nørskov, Z. Phys. Chem. **221**, 1209 (2007). 44

[41] B.C. Han, C.R. Miranda and G. Ceder, Phys. Rev. B **77**, 075410 (2008). 44

[42] S.W. Lee, S. Chen, W. Sheng, N. Yabuuchi, Y.-T. Kim, T. Mitani, E. Vescoco and Y. Shao-Horn, J. Am. Chem. Soc. **131**, 15669 (2009). 44

[43] S.W. Lee, S. Chen, J. Suntivich, K. Sasaki, R.R. Adzic and Y. Shao-Horn, J. Phys. Chem. Lett. **1**, 1316 (2010). 44

[44] B. Hammer and J.K. Nørskov, Surf. Sc. **343**, 211 (1995). 44, 89, 159

[45] K.J.J. Mayrhofer, B.B. Blizanac, M. Arenz, V.R. Stamenkovic, P.N. Ross and N.M. Markovic, J. Phys. Chem. B **109**, 14433 (2005). 44

[46] S. Mukerjee and S. Srinivasan, J. Electroanal. Chem. **357**, 201 (1993). 45

[47] S. Mukerjee, S. Srinivasan, M.P. Soriaga and J. McBreen, J. Electrochem. Soc. **142**, 1409 (1995). 45

[48] A.V. Ruban, H.L. Skriver and J.K Nørskov, Phys. Rev. B **59**, 15990 (1999). 45

[49] J. Zhang, Y. Mo, M.B. Vukmirovic, R. Klie, K. Sasaki and R.R. Adzic, J. Phys. Chem. B **108**, 10955 (2004). 45

[50] V.R. Stamenkovic, B. Fowler, B.S. Mun, G. Wang, P.N. Ross, C.A. Lucas and N.M. Marković, Science **315**, 493 (2007). 45, 48, 89

[51] V.R. Stamenkovic, B. Simon Mun, M. Arenz, K.J.J. Mayrhofer, C.A. Lucas, G. Wang, P.N. Ross and N.M. Marković, Nature Materials **6**, 241 (2007). 45

[52] M. Lefèvre, E. Proietti, F. Jaouen and J.-P. Dodelet, Science **324**, 71 (2009). 46

[53] Q. Liang, Y. Jianguo and L. Ju, J. Chem. Phys. **125**, 054701 (2006). 47, 48

[54] T. Jacob and W.A. Goddard III, ChemPhysChem **7**, 992 (2006). 47

[55] K.C. Neyerlin, W. Gu, J. Jorne and H.A. Gasteiger, J. Electrochem. Soc. **153**, A1955 (2006). 48

[56] R. Makharia, M.F. Mathias and D.R. Baker, J. Electrochem. Soc. **152**, A970 (2005). 48

[57] A.B. Anderson et al., Electrochim. Act. **47**, 2999 (2002). 48

[58] A.B. Anderson, J. Roques, S. Mukerjee, V.S. Murthi, N.M. Marković and V. Stamenkovic, J. Phys. Chem. B **109**, 1198 (2005). 48

[59] J.K Nørskov, J. Rossmeisl, A. Logadottir, L. Lindqvist, J.R. Kitchin, T. Bligaard and H. Jónsson, J. Phys. Chem. B **108**, 17886 (2004). 48, 49

[60] J. Greeley, I.E.L. Stephens, A.S. Bondarenko, T.P. Johansson, H.A. Hansen, T.F. Jaramillo, J. Rossmeisl, I. Chorkendorff and J.K. Nørskov, Nature Chem. **1**, 552 (2009). 48

[61] J.K Nørskov, F. Abild-Pedersen, F. Studt and T. Bligaard, PNAS **108**, 937 (2011). 48

[62] M. Teliska, V.S. Murthi, S. Mukerjee and D.E. Ramaker, J. Electrochem. Soc. **152**, A2159 (2005). 48

[63] J.X. Wang, N.M. Marković and R.R. Adzic, J. Phys. Chem. B **108**, 4127 (2004). 48, 70

[64] M. Shao, P. Lu and R.R. Adzic, J. Am. Chem. Soc. **128**, 7408 (2006). 49, 71

[65] I. Chorkendorff and J.W. Niemantsverdriet, "Concepts of modern catalysis and kinetics", Wiley, 2007. 50

[66] CRC Handbook of Chemistry and Physics, CRC press, 84th ed., 2003-2004. 56, 59, 93

[67] R.A. Marcus, Electrochim. Acta **13**, 955 (1968). 57

[68] P. Vassilev, R.A. van Santen and M.T.M. Koper, J. Chem. Phys. **122**, 054701 (2005). 57, 105

[69] R.I. Cukier and D.G. Nocera, Annu. Rev. Phys. Chem. **49**, 337 (1998). 57

[70] O. Pecina and W. Schmickler, Chem. Phys. **228**, 265 (1998). 57

[71] W. Schmikler, Chem. Phys. Lett. **237**, 152 (1995). 57

[72] J.B. Straus, A. Calhoun and G.A. Voth, J. Chem. Phys. **120**, 529 (1995). 57, 105

[73] E. Santos and W. Schmickler, "Fuel cell catalysis - A surface science approach", Wiley, 2009, Chap. 2. 57

[74] L.J. Richter and W. Ho, Phys. Rev. B **36**, 9797 (1987). 59

[75] J.L. Gland, B.A. Sexton and G.B. Fisher, Surf. Sc. **95**, 587 (1980). 59, 69

[76] K. Bedürftig, S. Völkening, Y. Wang, J. Wintterlin, K. Jacobi and G. Ertl, J. Chem. Phys. **111**, 11147 (1999). 59

[77] N.A. Deskins, J. Lauterbach and K.T. Thomson, J. Chem. Phys. **122**, 184709 (2005). 60

[78] D.C. Ford, Y. Xu, M. Mavrikakis, Surf. Sc. **587**, 159 (2005). 60

[79] J.M. Hawkins, J.F. Weaver and A. Asthagiri, Phys. Rev. B **79**, 125434 (2009). 60

[80] E. Janin, H. von Schenck, M. Göthelid, U.O. Karlsson and M. Svensson, Phys. Rev. B **61**, 13144 (2000). 60

[81] A. Panchenko, M.T.M. Koper, T.E. Shubina, S.J. Mitchell and E. Roduner, J. Electrochem. Soc. **151**, A2016 (2004). 60

[82] Z. Shi, J. Zhang, Z.-S. Liu, H. Wang and D.P. Wilkinson, Electrochim. Acta **51**, 1905 (2006). 60

[83] H. Angerstein-Kozlowska, B.E. Conway and W.B.A. Sharp, Electroanal. Chem. Inter. Electrochem. **43**, 9 (1973). 61

[84] C. Clay, S. Haq and A. Hodgson, Phys. Rev. Lett. **92**, 046102 (2004). 61

[85] G.S. Karlberg, F.E. Olsson, M. Persson and G. Wahnström, J. Chem. Phys. **119**, 4865 (2003). 61

[86] A. Michaelides and P. Hu, J. Chem. Phys. **114**, 513 (2001). 61

[87] G. Jerkiewicz, G. Vatankhah, J. Lessard, M.P. Soriaga and Y.-S. Park, Electrochim. Act. **49**, 1451 (2004). 61

[88] M. Wakisaka, H. Suzuki, S. Mitsui, H. Uchida and M. Watanabe, Langmuir **25**, 1897 (2009). 61, 62

[89] V. Viswanathan, H.A. Hansen, J. Rossmeisl, T. Jaramillo, H. Pitsch and J.K. Nørskov, J. Am. Chem. Soc. (2009) (in preparation). 61

[90] H.A. Hansen, J. Rossmeisl and J.K Nørskov, Phys. Chem. Chem. Phys. **10**, 3722 (2008). 61

[91] J. Rossmeisl, J.K. Nørskov, C.D. Taylor, M.J. Janik and M. Neurock, J. Phys. Chem. B **110**, 21833 (2006). 61

[92] K. Reuter, D. Frenkel and M. Scheffler, Phys. Rev. Lett. **93**, 116105 (2004). 64

[93] C.C. Fu, J. dalla Torre, F. Willaime, J.-L. Bocquet and A. Barbu, Nature Mat. **4**, 68 (2005). 64

[94] K.J.J. Mayrhofer, D. Strmcnik, B.B. Blizanac, V. Stamenkovic, M. Arenz and N.M. Markovic, Electrochim. Acta **53**, 3181 (2008). 44, 67

[95] V. Stamenković, T.J. Schmidt, P.N. Ross and N.M. Marković, J. Phys. Chem. B **106**, 11970 (2002). 67, 70

[96] N.R. Avery, Chem. Phys. Lett. **96**, 371 (1983). 69

[97] J.L. Gland, Surf. Sc. **93**, 487 (1980). 69

[98] H. Steininger, S. Lehwald and H. Ibach, Surf. Sc. **123**, 1 (1982). 69

[99] J. Rossmeisl, A. Logadottir and J.K. Nørskov, Chem. Phys. **319**, 178 (2005). 71

[100] P.D. Nolan, B.R. Lutz, P.L. Tanaka, J.E. Davis and C.B. Mullins, J. Chem. Phys. **111**, 3696 (1999). 72

[101] J. Rossmeisl, G.S. Karlberg, T. Jaramillo and J.K Nørskov, Faraday Disc. **140**, 337 (2008). 72

[102] I. Dabo, B. Kozinsky, N.E. Singh-Miller and N. Marzari, Phys. Rev. B **77**, 115139 (2008). 74, 80, 93

[103] M. Otani and O. Sugino, Phys. Rev. B **73**, 115407 (2006). 74, 77, 89

[104] A.J. Bard and L.R. Faulkner, "Electrochemical methods : Fundamentals and applications", Wiley, 2nd ed., 2001. 76

[105] R. Parsons, Chem. Rev. **90**, 813 (1990). 76

[106] G.S. Karlberg, J. Rossmeisl and J.K. Nørskov, Phys. Chem. Chem. Phys. **9**, 5158 (2007). 76

[107] A.Y. Lozovoi and A. Alavi, Phys. Rev. B **68**, 245416 (2003). 77

[108] C.D. Taylor, S.A. Wasileski, J.-S. Filhol and M. Neurock, Phys. Rev. B **73**, 165402 (2006). 77

[109] K.-Y. Yeh, S.A. Wasileski and M.J. Janik, Phys. Chem. Chem. Phys. **11**, 10108 (2009). 77

[110] I. Dabo, N. Bonnet , Y.L. Li and N. Marzari, "Fuel cell science : theory, fundamentals, and biocatalysis" edited by A. Wieckowski and J. Nørskov, Wiley, 2010, Chap. 13. 77, 89

[111] R. Jinnouchi and A.B. Anderson, J. Phys. Chem. Lett. C **112**, 8747 (2008). 77

[112] J. Rossmeisl, E. Skúlason, M.E. Björketun, V. Tripkovic and J.K. Nørskov, Chem. Phys. Lett. **466**, 68 (2008). 77, 89

[113] M. Otani, I. Hamada, O. Sugino, Y. Morikawa, Y. Okamoto and T. Ikeshoji, J. Phys. Soc. Japan **77**, 024802 (2008). 77

[114] E. Skúlason, G.S. Karlberg, J. Rossmeisl, T. Bligaard, J. Greeley, H. Jónsson and J.K. Nørskov, Phys. Chem. Chem. Phys. **9**, 3241 (2007). 77

[115] J.-L. Fattebert and F. Gygi, Int. J. Quant. Chem. **93**, 139 (2003). 78

[116] D.A. Scherlis, J.-L Fattebert, F. Gygi, M. Cococcioni and N. Marzari, J. Chem. Phys. **124**, 74103 (2006). 78

[117] S. Trasatti, Pure Appl. Chem. **58**, 955 (1986). 78

[118] S. Trasatti, Russ. J. Electrochem. **31**, 713 (1995). 78

[119] I. Dabo, E. Cancès, Y. Li and N. Marzari, in submission, arXiv:0901.0096v2. 78, 80, 84

[120] A.Y. Lozovoi, A. Alavi, J. Kohanoff and R.M. Lynden-Bell, J. Chem. Phys. **115**, 1661 (2001). 78

[121] G. Blyholder, J. Phys. Chem. **68**, 2772 (1964). 79

[122] J.A. Rodriguez and D.W. Goodman, Science **257**, 897 (1992). 79

[123] B. Hammer, Y. Morikawa and J.K. Nørskov, Phys. Rev. Lett. **76**, 2141 (1996). 79

[124] J.S. Luo and R.G. Tobin, Chem. Phys. Lett. **204**, 445 (1993). 79, 80, 84

[125] S.P. Mehandru and A.B. Anderson, J. Phys. Chem. **93**, 2044 (1989). 80

[126] P.S. Bagus, C.J. Nelin, W. Müller, M.R. Philpott and H. Seki, Phys. Rev. Lett. **58**, 2044 (1989). 80

[127] P.S. Bagus and G. Pacchioni, Surf. Sc. **236**, 233 (1990). 80

[128] S.A. Wasileski, M.T.M. Koper and M.J. Weaver, J. Chem. Phys. **115**, 8193 (2001). 80

[129] F. Illas, F. Mele, D. Curulla, A. Clotet and J.M. Ricart, Electrochim. Act. **44**, 1213 (1998). 80

[130] M. Head-Gordon and J.C. Tully, Chem. Phys. **175**, 37 (1993). 80

[131] C. Korzeniewski, S. Pons, P.P. Schmidt and M.W. Severson, J. Chem. Phys. **85**, 7 (1986). 80

[132] M.T.M. Koper, R.A. van Santen, S.A. Wasileski and M.J. Weaver, J. Chem. Phys. **113**, 4392 (2000). 80

[133] D. Curulla, A. Clotet, J.M. Ricart and Francesc Illas, Electrochim. Acta **45**, 639 (1999). 80

[134] T.C. Leung, C.L. Kao, W.S. Su, Y.J. Feng and C.T. Chan, Phys. Rev. B **68**, 195408 (2003). 82

[135] L. Qi, X. Qian and J. Li, Phys. Rev. Lett. **101**, 146101 (2008). 82

[136] A.Y. Lozovoi and A. Alavi, J. Electroanal. Chem. **607**, 140 (2007). 80, 84

[137] S. Baroni et al., Quantum-ESPRESSO, http://www.quantum-espresso.org. 80, 93

[138] M. Sterrer, M. Yulikov, E. Fischbach, M. Heyde, H.-P. Rust, G. Pacchioni, T. Risse and H.-J. Freund, Angew. Chem. Int. Ed. **45**, 2630 (2006). 88

[139] G.S. Karlberg, T.F. Jaramillo, E. Skúlason, J. Rossmeisl, T. Bligaard and J.K. Nørskov, Phys. Rev. Lett. **99**, 126101 (2007). 92

[140] T. Pajkossy and D.M. Kolb, Electrochim. Act. **46**, 3063 (2001). 93, 125, 126

[141] A. Cuesta, Surf. Sc. **572**, 11 (2004). 93

[142] M. Otani, I. Hamada, O. Sugino, Y. Morikawa, Y. Okamoto and T. Ikeshoji, Phys. Chem. Chem. Phys. **10**, 3593 (2008). 93

[143] R. Guidelli and W. Schmickler, "Modern aspects of electrochemistry, number 38", ed. by B.E. Conway et al., Kluwer Academic/Plenum Publishers, 2005. 96

[144] N. Garcia-Araez, V. Climent, E. Herrero, J.M. Feliu and J. Lipkowski, Electrochim. Acta **51**, 3787 (2006). 96

[145] N.M. Marković, B.N. Grgur and P.N. Ross, J. Phys. Chem. **101**, 5405 (1997). 97, 98

[146] N.M. Marković, H.A. Gasteiger and P.N. Ross, J. Phys. Chem. **100**, 6715 (1996). 97, 98

[147] N.M. Marković, T.J. Schmidt, B.N. Grgur, H.A. Gasteiger, R.J. Behm and P.N. Ross, J. Phys. Chem. **103**, 8568 (1999). 97, 98

[148] P. Delahay, "Double layer and electrode kinetics", Wiley, 1965, Chap. 2. 97

[149] N.E. Singh-Miller and N. Marzari, Phys. Rev. B **80**, 235407 (2009). 98

[150] G. Wulff, Z. Kristallogr. Mineral. **34**, 449 (1901). 98

[151] R.V. Chepulskii and S. Curtarolo, ACS Nano **5**, 247 (2011). 98

[152] J. Ferreira and Y. Shao-Horn, Electrochem. Solid-St. Lett. **10**, 3 (2007). 100

[153] N. Tian, Z.-Y. Zhou, S.-G. Sun, Y. Ding and Z.L. Wang, Science **316**, 732 (2007). 100

[154] J.A. Morrone and R. Car, Phys. Rev. Lett. **101**, 017801 (2008). 101, 105

[155] P.J. Feibelman, Physics Today **63**, 34 (2010). 102

[156] A. Michaelides, Appl. Phys. A **85**, 415 (2006). 102, 164

[157] A. Hodgson, S. Haq, Surf. Sc. Rep. **64**, 381 (2009). 102, 103

[158] P.A. Thiel, T.E. Madey, Surf. Sc. Rep. **7**, 211 (1987). 102

[159] M.A. Henderson, Surf. Sc. Rep. **46**, 5 (2002). 102

[160] H. Ogasawara et al., Phys. Rev. Lett. **89**, 276102 (2002). 102

[161] G. Held, D. Menzel, Surf. Sc. **316**, 92 (1994). 103

[162] P.J. Feibelman, Phys. Rev. B **67**, 035420 (2003). 103

[163] P.J. Feibelman et al., Science **295**, 99 (2002). 103

[164] A. Michaelides, A. Alavi, D. A. King, J. Am. Chem. Soc. **125**, 2746 (2003). 103

[165] G.A. Kimmel, N.G. Petrik, Z. Dohnálek and B.D. Kay, Phys. Rev. Lett. **95**, 166102 (2005). 103

[166] F. McBride, G.R. Darling, K. Pussi and A. Hodgson, Phys. Rev. Lett. **106**, 226101 (2011). 103

[167] J. Carrasco, B. Santra, J. Klimeš and A. Michaelides, Phys. Rev. Lett. **106**, 026101 (2011). 104

[168] S. Grimme, J. Antony, S. Ehrlich and H. Krieg, J. Chem. Phys. **132**, 154104 (2010). 104

[169] H. Noguchi, T. Okada and K. Uosaki, Faraday Discuss. **140**, 125 (2008). 104

[170] G. Nagy, K. Heinzinger and E. Spohr, Faraday Discuss. **94**, 307 (1992). 104

[171] G. Aloisi, M.L. Foresti and R. Guidelli, J. Chem. Phys. **91**, 5592 (1989). 104

[172] P.H.-L. Sit and N. Marzari, J. Chem. Phys. **122**, 204510 (2005). 105

[173] M. Allesch, E. Schwegler, F. Gygi and G. Galli, J. Chem. Phys. **102**, (2004). 105

[174] L. Pauling, J. Am. Chem. Soc. **57**, 2680 (1935). 105

[175] E.H. Lieb, Phys. Rev. Lett. **18**, 692 (1967). 105

[176] J.F. Nagle, J. Chem. Phys. **61**, 883 (1974). 105

[177] G.T. Barkema and J. de Boer, J. Chem. Phys. **99**, 883 (1993). 106

[178] S.W. Rick and A.D.J. Haymet, J. Chem. Phys. **118**, 9291 (2003). 106

[179] C. Knight, S.J. Singer, J.-L. Kuo, T.K. Hirsch, L. Ojamäe and M.L. Klein, Phys. Rev. E **73**, 056113 (2006). 106, 119

[180] J.-L. Kuo, Phys. Chem. Chem. Phys. **7**, 3733 (2005). 106

[181] M. Sharma, R. Resta and R. Car, Phys. Rev. Lett. **98**, 247401 (2007). 106

[182] L. Onsager, J. Am. Chem. Soc. **58**, 1486 (1936). 107

[183] J.N. Wilson, Chem. Rev. **25**, 377 (1939). 107

[184] G.H. Wannier, Phys. Rev. **52**, 191 (1937). 108

[185] N. Marzari and D. Vanderbilt, Phys. Rev. B **56**, 12847 (1997). 108

[186] R. Resta, Rev. Mod. Phys. **66**, 899 (1994). 108

[187] K. Röttger, A. Endriss, J. Ihringer, S. Doyle and W.F. Kuhs, Acta Cryst. **B50**, 644 (1994). 109

[188] P. Debye, Physik. Z. **13**, 97 (1912). 115

[189] G.P. Johari and E. Whalley, J. Chem. Phys. **75**, 1333 (1981). 115

[190] J.L. Aragones, L.G. MacDowell and C. Vega, J. Phys. Chem. A **115**, 5745 (2011). 122

[191] U. Kaatze, J. Chem. Eng. Data **34**, 371 (1989). 125

[192] A. Roudgar and Axel Gross, Chem. Phys. Lett. **409**, 157 (2005). 127

[193] C.G. Sánchez, Surf. Sc. **527**, 1 (2003). 127

[194] http://www.andrew.cmu.edu/course/39-801. 129

[195] B.E. Conway, J.O'M. Bockris and I.A. Ammar, Trans. Faraday Soc. **47**, 756 (1951). 130

[196] J. Larminie and A. Dicks, "Fuel cell systems explained", Wiley, 2nd ed., 2003. 133

[197] G. García and M.T.M. Koper, ChemPhysChem (2011) (to be included in issue). 134, 137

[198] N.P. Lebedeva, M.T.M. Koper, J.M. Feliu and R.A. van Santen, J. Phys. Chem. B **106**, 12938 (2002). 134

[199] F. Abild-Pedersen and M.P. Andersson, Surf. Sc. **601**, 1747 (2007). 135, 143

[200] M.Ø. Pedersen, S. Helveg, A. Ruban, I. Stensgaard, E. Lægsgaard, J.K Nørskov and F. Besenbacher, Surf. Sc. **426**, 395 (1999). 135

[201] Y. Gohda and A. Gross, J. Electroanal. Chem. **607**, 47 (2007). 135

[202] Y. Gohda and A. Gross, Surf. Sc. **601**, 3702 (2007). 135

[203] D. Strmcnik, K. Kodama, D. van der Vliet, J. Greeley, V.R. Stamenkovic and N.M. Marković, Nature Chem. **1**, 466 (2009). 137

[204] A. Stroppa and G. Kresse, N. J. Phys. **10**, 063020 (2008). 137

[205] G. Kresse, A. Gil and P. Sautet, Phys. Rev. B **68**, 073401 (2003). 138

[206] I. Dabo, A. Wieckowski and N. Marzari, J. Am. Chem. Soc. **129**, 11045 (2007). 139

[207] B. Hammer, L.B. Hansen and J.K. Nørskov, Phys. Rev. B **59**, 7413 (1999). 140

[208] P. Lazić, M. Alaei, N. Atodiresei, V. Caciuc, R. Brako and S. Blügel, Phys. Rev. B **81**, 045401 (2010). 140

[209] L. Schimka, J. Harl, A. Stroppa, A. Grüneis, M. Marsman, F. Mittendorfer and G. Kresse, Nature Mat. **9**, 741 (2010). 146

[210] J. Harl and G. Kresse, Phys. Rev. Lett. **103**, 056401 (2009). 146

[211] R. Hoffmann, Rev. Mod. Phys. **60**, 601 (1988). 159

[212] B. Hammer and J.K. Nørskov, Nature **376**, 238 (1995). 159

[213] M. Valden, X. Lai and D.W. Goodman, Science **281**, 1647 (1998). 160

[214] N. Lopez and J.K. Nørskov, J. Am. Chem. Soc. **124**, 11262 (2002). 160

[215] J.W. Niemantsverdriet, "Spectroscopy in catalysis", Wiley, 2007. 161

[216] M.C. Payne, M.P. Teter, D.C. Allan, T.A. Arias and J.D. Joannopoulos, Rev. Mod. Phys. **64**, 1045 (1992). 168

[217] D. Vanderbilt, Phys. Rev. B **41**, 7892 (1990). 168